# Optical Characterisation of Dry Etched II-VI Semiconductors

Andrew Patrick Smart B.Sc., M.Sc.

A thesis submitted for the degree of Doctor of Philosophy
in the Faculty of Engineering in the University of Glasgow

September 1994

© A.P. Smart, 1994

ProQuest Number: 13818454

All rights reserved

INFORMATION TO ALL USERS
The quality of this reproduction is dependent upon the quality of the copy submitted.

In the unlikely event that the author did not send a complete manuscript
and there are missing pages, these will be noted. Also, if material had to be removed,
a note will indicate the deletion.

ProQuest 13818454

Published by ProQuest LLC (2018). Copyright of the Dissertation is held by the Author.

All rights reserved.
This work is protected against unauthorized copying under Title 17, United States Code
Microform Edition © ProQuest LLC.

ProQuest LLC.
789 East Eisenhower Parkway
P.O. Box 1346
Ann Arbor, MI 48106 – 1346

Thesis
10184
Copy 1

to my parents

What time I wasted youthful hours,
One of the shining wingèd powers,
Show'd me vast cliffs, with crowns of towers.

As towards that gracious light I bow'd,
They seem'd high palaces and proud,
Hid now and then with sliding cloud.

He said, "The labour is not small;
Yet winds the pathway free to all:-
Take care thou dost not fear to fall!"

Lord Tennyson

Where dips the rocky highland
Of Sleuth Wood in the lake,
There lies a leafy island
Where flapping herons wake
The drowsy water-rats;
There we've hid our faery vats,
Full of berries
And of reddest stolen cherries.
*Come away, O human child!*
*To the waters and the wild*
*With a faery, hand in hand,*
*For the world's more full of weeping than you can understand.*

Where the wave of moonlight glosses
The dim grey sands with light,
Far off by furthest Rosses
We foot it all the night,
Weaving olden dances,
Mingling hands and mingling glances
Till the moon has taken flight;
To and fro we leap
And chase the frothy bubbles,
While the world is full of troubles
And is anxious in its sleep.
*Come away, O human child!*
*To the waters and the wild*
*With a faery, hand in hand,*
*For the world's more full of weeping than you can understand.*

Where the wandering water gushes
From the hills above Glen-Car,
In pools among the rushes
That scarce could bathe a star,
We seek for slumbering trout
And whispering in their ears
Give them unquiet dreams;
Leaning softly out
From ferns that drop their tears
Over the young streams.
*Come away, O human child!*
*To the waters and the wild*
*With a faery, hand in hand,*
*For the world's more full of weeping than you can understand.*

Away with us he's going,
The solemn-eyed:
He'll hear no more the lowing
Of the calves on the warm hillside
Or the kettle on the hob
Sing peace into his breast,
Or see the brown mice bob
Round and round the oatmeal-chest.
*Come away, O human child!*
*To the waters and the wild*
*With a faery, hand in hand,*
*For the world's more full of weeping than you can understand.*

W.B. Yeats

**Acknowledgements**

I would like to take this opportunity to thank some of the many people who have helped towards the completion of this project.

First I would like to thank my supervisor Dr. Clivia Sotomayor Torres for providing the spectroscopy facilities for me to carry out this research. I am indebted to her for the time spent and inconvenience suffered whilst reading and advising me on this thesis. Her support and concern throughout the duration of the project will not be forgotten, thanks Clivia! I must also mention Dr. Morag Watt who took time to show me the ropes and explain the basics.

I would also like to thank Professor P. Laybourn and his predecessor, the late Professor J. Lamb for providing the other facilities used in the course of this project. Thank you also to Professor C. Wilkinson for his help and suggestions in his role as joint supervisor.

The smooth running of the laboratory could not have happened without the expert technical support of Messrs. D. Irons, J. Smith and A. Ross. I must also thank Miss H. Wallace for her advice and help on fabrication matters.

A special sincere thank you to my parents for instilling in me the will to learn, for their endless support and for never doubting my abilities. An engineer is a crazy investment but I hope this goes part of the way to repaying you. The students and research assistants of the Rankine Building deserve a huge thank you for providing the good times and unmemorable nights. Thanks especially to Dave and Sarah Staton for their solid support. My employers at Electrotech have allowed me time and freedom without which the completion of this thesis would not have been possible. Christine and David

Scott deserve a mention for all their support as do Liz and Dave Malpass, Murthy and Mark Ford.

Financial support was provided by a Science and Engineering Research Council QUOTA award. While this is gratefully acknowledged I feel I must point out I could not have survived without the generosity of my family, the department and various part-time employers. Thank you also to The Fellowship of Engineering for financing the study trip to Regensburg.

Finally the biggest thank you of all goes to my wife Kathryn , who has loyally stood by and supplied $x$ cups of coffee during our first year of marriage where $x$ is a very large and positive integer. I cannot possibly describe her support and can only say thank you to a lovely lady and a best friend. I promise the following years will be infinitely more enjoyable!

Andrew P. Smart

Chepstow, September 1994

# List of Tables


2.1 XPS results for control and etched ZnTe. 18
2.2 XPS results for control and etched ZnSe. 19

3.1 Lines and their powers available from the Spectra-Physics Argon-ion laser. 35
3.2 Raman active modes of Te. 69

4.1 Peaks occurring in low temperature PL of ZnSe. 81
4.2 RIE parameters for ZnSe. 82
4.3 Peaks occurring in low temperature PL of ZnTe. 93
4.4 RIE parameters for etching ZnTe wires. 106
4.5 Peaks occurring in low temperature PL of reactive ion etched ZnTe. 124

# List of Figures


| | | |
|---|---|---|
| 2.1 | TEM of ZnTe/GaAs interface. | 10 |
| 2.2 | Surface morphology of ZnTe as seen by Normarski. | 11 |
| 2.3 | Low temperature reflectivity of ZnTe from Regensburg. | 12 |
| 2.4 | Low temperature PL of ZnTe from Regensburg. | 13 |
| 2.5 | Schematic of 3M laser diode. | 14 |
| 2.6 | Schematic of D-SEED. | 24 |
| 3.1 | Lithographic process. | 32 |
| 3.2 | Schematic of a bilayer of resist after exposure and development. | 33 |
| 3.3 | Grating efficiency. | 37 |
| 3.4 | Light path through U1000 spectrometer. | 38 |
| 3.5 | Radiant sensitivity of PMT. | 40 |
| 3.6 | Spectral response of light detection system. | 41 |
| 3.7 | Detective quantum efficiency of CCD. | 44 |
| 3.8 | Schematic of apparatus arranged in near back scattering configuration. | 46 |
| 3.9 | Schematic of reactive ion etch system. | 50 |
| 3.10 | Graph of ZnTe etch rate against methane content of $CH_4/H_2$. | 51 |
| 3.11 | Energy levels of exciton. | 54 |
| 3.12 | Schematic of exciton bound to a donor. | 55 |
| 3.13 | Elementary Raman scattering process. | 61 |
| 3.14 | Deformation potential Raman polarisability near resonance. | 65 |
| 3.15 | Fröhlich Raman polarisability near resonance. | 66 |
| 3.16 | Folded acoustic phonon. | 71 |
| 3.17 | Schematic of quantum wire. | 76 |
| 4.1 | NBE low temperature PL from ZnSe control. | 81 |
| 4.2 | NBE low temperature PL from ZnSe control and etched (1:2/1:3/1:4) samples. | 82 |
| 4.3 | Low temperature PL from ZnSe control and etched (1:2/1:3/1:4) samples. | 83 |
| 4.4 | NBE low temperature PL from ZnSe control and etched samples (1:2/1:3/1:4) after annealing. | 84 |
| 4.5 | Low temperature PL from ZnSe control and etched (1:2/1:3/1:4) samples after annealing. | 84 |
| 4.6 | NBE low temperature PL from ZnSe control and etched (1:8/1:10) samples. | 85 |
| 4.7 | Low temperature PL from ZnSe control and etched (1:8/1:10) samples. | 86 |
| 4.8 | NBE low temperature PL from ZnSe control and etched (1:8/1:10) samples after annealing. | 87 |
| 4.9 | Spectra from ZnSe obtained using different excitation frequencies. | 89 |
| 4.10 | Raman scattering from control and etched (1:2/1:3/1:4) samples of ZnSe. | 90 |
| 4.11 | Raman scattering from control and etched sample of ZnSe after time delay and anneal. | 91 |
| 4.12 | Raman scattering from control and etched sample of ZnSe after time delay and anneal in $Ar+H_2$ and then pure Ar. | 92 |
| 4.13 | NBE low temperature PL from ZnTe control. | 93 |
| 4.14 | NBE low temperature PL from ZnTe control and etched (1:6/1:8/1:10) samples. | 94 |
| 4.15 | Low temperature PL from ZnTe control and etched (1:6/1:8/1:10) samples. | 96 |
| 4.16 | NBE low temperature PL from ZnTe control and etched (1:6/1:8/1:10) samples after annealing. | 97 |
| 4.17 | Deep level low temperature PL from ZnTe control and etched (1:6/1:8/1:10) samples after annealing. | 97 |
| 4.18 | Low temperature Raman scattering from ZnTe control. | 99 |
| 4.19 | Variation of peak intensity of ZnTe LO phonon with temperature, 5145 Å excitation. | 100 |
| 4.20 | Variation of peak intensity of ZnTe LO phonon with temperature, 5286 Å excitation. | 101 |
| 4.21 | Low temperature Raman scattering from ZnTe control and etched (1:6/1:8/1:10) samples. | 102 |
| 4.22 | Low temperature Raman scattering from ZnTe control and etched thick sample. | 103 |
| 4.23 | Micrograph of 80 nm ZnTe wires. | 106 |
| 4.24 | Room temperature Raman scattering from ZnTe control, unpatterned area and wires. | 108 |
| 4.25 | Micrograph of Ti mask after lift-off. | 109 |
| 4.26 | Micrograph of ZnTe wires that have fallen over due to anisotropy factor becoming too great. | 110 |

| | | |
|---|---|---|
| 4.27 | Micrograph of 20 nm ZnTe wires. | 111 |
| 4.28 | Close-up micrograph of 20 nm ZnTe wires. | 112 |
| 4.29 | Effect of excitation frequency on Raman scattering from ZnTe. | 113 |
| 4.30 | Effect of excitation power on Raman scattering from ZnTe. | 114 |
| 4.31 | Effect of sample temperature on Raman scattering from ZnTe. | 116 |
| 4.32 | Effect of polarisation on Raman scattering from ZnTe. | 118 |
| 4.33 | Effect of sample orientation on Raman scattering from ZnTe. | 120 |
| 4.34 | Effect of the orientation of wires on Raman scattering from ZnTe. | 121 |
| 4.35 | Comparison of low temperature Raman scattering from wires and unpatterned area. | 123 |
| 4.36 | NBE low temperature PL from ZnTe wires and unpatterned areas. | 124 |
| 4.37 | Micrograph of ZnTe dot. | 126 |
| 4.38 | Room temperature Raman scattering from ZnTe dots. | 127 |
| 4.39 | Comparison of low temperature Raman scattering from dots and unpatterned area, 5145 Å excitation. | 128 |
| 4.40 | Comparison of low temperature Raman scattering from dots and unpatterned area, 5286 Å excitation. | 129 |
| | | |
| A1 | Low temperature Raman scattering from *ZS371*. | 143 |
| A2 | Low temperature Raman scattering from *ZS377*. | 144 |
| A3 | Low temperature Raman scattering from *ZS379*. | 144 |
| A4 | Room temperature Raman scattering from *MB313*. | 145 |
| A5 | Room temperature Raman scattering from *P26*. | 145 |
| A6 | Low temperature PL from *Q97*. | 146 |
| A7 | Room temperature Raman scattering from *Q97*. | 146 |
| A8 | Micrograph of wires etched in *DJI22A*. | 147 |
| A9 | Low temperature PL of *DJI22A*. | 148 |
| A10 | Low temperature PL from wires etched in *DJI22A*. | 148 |
| A11 | Low temperature Raman scattering from *DJI22A*. | 149 |
| A12 | Low temperature Raman scattering from wires etched in *DJI22A*. | 149 |
| A13 | Low temperature PL from wires etched in *DJI28A*. | 150 |
| A14 | Low temperature Raman scattering from *DJI28A*. | 150 |
| A15 | Low temperature PL from *DJI30A*. | 151 |
| A16 | Low temperature Raman scattering from *DJI30A*. | 151 |
| A17 | Room temperature Raman scattering temperature PL from *DJI30A*. | 152 |
| A18 | Low temperature PL from *DJI31A*. | 152 |
| A19 | Low temperature Raman scattering from *DJI31A*. | 153 |

## Publications Arising from this Work

Foad, M.A., Smart, A.P., Watt, M., Sotomayor Torres, C.M. and Wilkinson, C.D.W.
"Reactive Ion Etching of II-VI Semiconductors Using a Mixture of Methane and Hydrogen"
Electronics Letters **27**(1) 73 (1991).

Foad, M.A., Watt, M., Smart, A.P., Sotomayor Torres, C.M., Wilkinson, C.D.W., Kuhn, W., Wagner, H.P., Leiderer, H., Bauer, S. and Gebhardt, W.
"High Resolution Dry Etching of Zinc Telluride: Characterisation of Etched Surfaces by X-Ray Photoelectron Spectroscopy, Photoluminescence and Raman Scattering"
Semicond. Sci. Technol **6** A115 (1991).

Watt, M., Smart, A.P., Foad, M.A., Wilkinson, C.D.W., Arnot, H.E.G. and Sotomayor Torres, C.M.
"Raman Scattering of III-V and II-VI Semiconductor Microstructures"
in "Light Scattering in Semiconductor Structures and Superlattices"
NATO ASI Series B,
Volume **273**, 247,
Plenum Publishing, New York (1991).

Foad, M.A., Smart, A.P., Watt, M., Sotomayor Torres, C.M., Kuhn, W., Wagner, H.P., Leiderer, H., Bauer, S., Wilkinson, C.D.W., Gebhardt, W. and Razeghi, M.
"Fabrication and Assessment of Wires and Dots in ZnTe and ZnSe"
in "Nanostructures and Mesoscopic Systems"
Proc. Int. Symp., Santa Fe, May 19-24, 1991, 463,
Academic Press, San Diego (1992).

Foad, M.A., Smart, A.P., Watt, M., Sotomayor Torres, C.M., Kuhn, W., Wagner, H.P., Leiderer, H., Bauer, S., Wilkinson, C.D.W., Gebhardt, W. and Razeghi, M.
"Optical Assessment of Reactive Ion Etched ZnTe and ZnSe for Nanostructures"
Surf. Sci. **267** 223 (1992).

Sotomayor Torres, C.M., Smart, A.P., Foad, M.A. and Wilkinson, C.D.W.
"Fabrication and Spectroscopy of Dry Etched Wide-Gap II-VI Semiconductor Nanostructures"
Advances in Solid State Physics **32** 265 (1992).

Smart, A.P., Sotomayor Torres, C.M., Tsutsui, K., Foad, M.A. and Wilkinson, C.D.W.
"Optical Spectroscopy of Dry Etched Zinc Telluride"
ASI Series E,
Volume **236**, 363,
Kluwer Publishing (1993).

Sotomayor Torres, C.M., Smart, A.P., Watt, M., Foad, M.A., Tsutsui, K. and Wilkinson, C.D.W.
"Nanometer Fabrication Techniques for Wide-Gap II-VI Semiconductors and Their Optical Characterisation"
J. Electronic Materials **23**(3) 289 (1994).

## Synopsis of Thesis

The topic of this thesis is the characterisation of dry etched II-VI semiconductors. After a brief introduction to the thesis there follows a review of the literature on the subjects encompassed by the thesis. The subjects covered include the development of the growth process and fabrication techniques. Also included is a summary of the theoretical aspects which have driven experimental research into nanotechnology.

There is a fairly rigorous description of the experimental apparatus used during the project which is split into spectroscopy equipment and fabrication equipment for reasons of clarity. The samples used in the course of the project are also described. This is followed by an intensive explanation of the theory behind the experimental techniques used in the assessment of the materials, specifically Raman scattering and photoluminescence spectroscopy. There is also a brief account of some crystallographic information concerning tellurium which is of relevance to this work.

The results are presented for each material considered, namely zinc selenide and zinc telluride. For each material the results are presented first for photoluminescence and then for Raman scattering. Each of these techniques was used to examine the samples as-grown and after a uniform etch was performed on the unpatterned samples using the technique of dry etching. The etch gas chemistry used was methane and hydrogen, the use of which to etch II-VI semiconductors was pioneered at Glasgow University. The experimental procedure is reported which was developed to fabricate wires and dots with dimensions down to 20 nm in zinc telluride. Use was made of electron-beam lithography to pattern a bilayer of positive electron-beam resist spun on the sample. The nanostructures were then characterised using the above optical spectroscopic techniques. The effect on the Raman scattering process of varying numerous parameters was investigated, these being excitation frequency and power, sample temperature and excitation polarisation. The difference between the region patterned with nanostructures

and the region away from the pattern was explored, as was the orientation of the wires with respect to the incoming laser radiation in the near back scattering configuration used.

The results of the experiments are discussed, paying particular consideration to the theoretical aspects discussed earlier concerning the confinement of phonons and crystalline damage. The subject of hydrogen incorporation and subsequent passivation of luminescence centres is broached. Relevant conclusions are then drawn from the results and discussion. Suggestions for extending the work covered in this thesis and any other work considered to be of interest concerning this project are then put forward.

# Contents

Acknowledgements
List of Tables
List of Figures
Publications Arising from this Work
Synopsis of Thesis

1 Introduction 1
- 1.1 General Introduction 1
- 1.2 Survey of the Following Chapters 4

2 Literature Review 8
- 2.1 Overview 8
- 2.2 Advances in II-VI Growth 9
- 2.3 Advances in Fabrication Techniques 15
- 2.4 Summary of Theoretical Interest in Nanotechnology 21

3 Experimental Methodology 25
- 3.1 Introduction 25
- 3.2 List of Samples 26
- 3.3 Resists and Masks 29
  - 3.3.1 Sample Preparation 29
  - 3.3.2 Resists and Masks 30
- 3.4 Equipment 34
  - 3.4.1 Spectroscopy Equipment 34
    - 3.4.1.1 Laser 34
    - 3.4.1.2 Spectrometer 36
    - 3.4.1.3 Photomultiplier Tube 39
    - 3.4.1.4 Spectral Response of the System 41
    - 3.4.1.5 Charge-Coupled Device 42
    - 3.4.1.6 Data Acquisition 44
    - 3.4.1.7 Cryostat 45
  - 3.4.2 Fabrication Equipment 47
    - 3.4.2.1 Electron-Beam Writer 47
    - 3.4.2.2 Reactive Ion Etcher 49
- 3.5 Experimental Techniques 52
  - 3.5.1 Photoluminescence 52
  - 3.5.2 Raman Scattering 56
    - 3.5.2.1 Raman Scattering from Phonons 56
    - 3.5.2.2 Resonant Raman Scattering 64
    - 3.5.2.3 Polarisation 66
    - 3.5.2.4 Raman Scattering from Tellurium 68
    - 3.5.2.5 Effect of Crystalline Damage on the Raman Spectrum 69
  - 3.5.3 Effect of Reduced Dimensions on Phonons 71
    - 3.5.3.1 Zone Folding 71
    - 3.5.3.2 Confined Phonons 72

4 Results 78
- 4.1 Introduction 78
- 4.2 Zinc Selenide 79
  - 4.2.1 Low Temperature Photoluminescence of Zinc Selenide 79
  - 4.2.2 Low Temperature Photoluminescence of Reactive Ion Etched Zinc Selenide 82
  - 4.2.3 Room Temperature Raman Spectroscopy of Zinc Selenide 87
- 4.3 Zinc Telluride 92
  - 4.3.1 Low Temperature Photoluminescence of Zinc Telluride 92
  - 4.3.2 Low Temperature Photoluminescence of Reactive Ion Etched Zinc Telluride 94

4.3.3 Raman Spectroscopy of Zinc Telluride 98
4.3.4 Raman Spectroscopy of Reactive Ion Etched Zinc Telluride 101
4.4 Wires Fabricated in Zinc Telluride 103
4.4.1 Fabrication of Wires 103
4.4.2 Unpolarised Raman Spectroscopy of Wires 107
4.4.3 Effect of Excitation Frequency 111
4.4.4 Considerations When Comparing Spectra 113
4.4.4.1 Effect of Excitation Power 114
4.4.4.2 Effect of Sample Temperature 115
4.4.5 Effect of Polarisation 117
4.4.6 Scattering from a Patterned Area Versus an Off-Pattern Area 119
4.4.7 Effect of Wire Orientation 119
4.4.8 Comparison of the LO and 2LO Phonon Peak Intensities 121
4.4.9 Photoluminescence of Wires 123
4.5 Cylinders Fabricated in Zinc Telluride 125
4.5.1 Fabrication of Cylinders 125
4.5.2 Raman Spectroscopy Cylinders 127

5 Discussion of Results 130
5.1 Importance of Starting Material 130
5.2 Effects of Dry-Etching 132

6 Conclusions and Future Work 136
6.1 Summary of Work Presented in this Thesis 136
6.2 Future Work 141

Appendix 143

References 154

# Chapter 1

# Introduction

## 1.1 General Introduction

Research into wide band-gap II-VI semiconductors began over twenty years ago, this early work has been reviewed by Aven and Prener [1.1]. The interest in these materials was setback because of the lack of good quality starting material relative to the competing technologies such as Si and GaAs. The far superior methods of preparation for Si and GaAs meant a great deal of interest was focused into these better quality materials. The large research interest spawned much new science and suggested many applications, the avalanche of interest was self-perpetuating and interest in II-VI semiconductors was left simmering. Recent advances in the growth techniques of *molecular beam epitaxy*, (MBE) and *metallo-organic chemical vapour deposition*, (MOCVD), have led to the realisation of good quality samples of wide band-gap II-VI semiconductor materials.

The competition between III-V semiconductors and Si has raged for over a decade. The III-V flag has been flown mainly by GaAs based upon its intrinsic electrical mobility which, being much higher than that of Si, enabled devices to be manufactured according to new scientific ideas, ideas which catered for the ever accelerating market of electronics upon which today's society is becoming more and more dependent. Si, though it has a lower intrinsic mobility, has always benefited from the developments demanded by industrial level and world-wide spread manufacturing and fabrication techniques. The

former is especially beneficial in reducing the all-important product cost while the latter has meant that whenever GaAs has got from A to B faster, courtesy of its higher mobility, Si has been able to arrive yet faster by being able to reduce the distance between A and B courtesy of a refinement in the fabrication steps.

The optical market however, did not stop evolving and recently demanded devices which operated at higher energies. This has opened the door for wide band-gap II-VI semiconductors since they emit at higher energies, well into the visible part of the spectrum and even into the blue in the case of zinc selenide. There is however competition in this area from III-Vs in the form of GaN and AlGaN from which pulsed emission at 380 nm has been reported [1.2]. For III-Vs the possibility also exists to *frequency double* emission to reduce the wavelength using frequency doubling crystals. This technique requires two elements, which means valuable space is taken up and the system requires some degree of alignment. Therefore this idea is likely to become redundant as soon as single element sources become available.

Photographic processes occur much faster when higher energy light is used and so there is a demand from this sector for high energy light sources. This is also true for reprographics where photocopying could be made much more efficient with the advent of a short wavelength solid state laser.

Devices which operate in the visible region of the spectrum can be used for display purposes. The combination of yellow and black optimises the performance of the human eye. This point has been picked up by some bus companies which use printed yellow dots to form the letters of the destination thereby allowing people waiting at bus stops the opportunity of reading the destination of the bus from a further distance than if the destination were printed in other colours. This is a crude attempt to imitate a display of LEDs. If the dots or pixels were LEDs there would be no need to provide a flooding

white light illumination at night as is the case with these displays. The development costs of the printed dots are minor when compared to the costs of developing an LED display however, and so it has to be conceded this is not an area in which visible LEDs will eclipse other technologies. Nevertheless, the whole issue of large panel displays requires further research. For example, to meet the demand to update constantly a display such as is the case at a concourse of a busy train station or airport, the printed dot technology proves to be inflexible since all the messages must be prepared in advance. Here is a niche for the LED based technology where the LEDs can be switched on and off as required by simple electronics. There is such a display already in operation at Helsinki airport.

The constant drive towards miniaturisation of electronics is now being held up by the absence of relatively small power supplies and batteries and also the displays. Televisions could be made smaller if the cathode ray tube were made obsolete, though in this case, the demand is for a small box of electronics which is fronted by as large a screen as possible. The relatively new market of portable computers is providing a lot of momentum for the development of display technology. There are many possible technologies available at the moment none of which is dominant. At the budget end of the market LCD technology is still a popular means of achieving a low resolution monochrome display at a relatively low cost. Gas plasma technology allows the production of colour displays and there is a major effort in the area of thin film transistors at the moment, though the cost of this technology precludes it from all but the executive end of the market. When visible LEDs become available in all three primary colours they could be used in a similar manner to the phosphors in today's televisions where any colour can be produced at a pixel by a mixture of the primary colours.

The use of optical storage discs is becoming more and more common. The limit of resolution for light to read the information stored in this manner is $\lambda/4$, hence reducing $\lambda$ allows the packing density to be increased. This has the knock-on effect of allowing more

information to be stored on a set disc or the disc size can be reduced if a finite amount of data needs to be stored.

Recently there have been reports that IBM have succeeded in developing an optical disc which records the information bits on six different physical levels (four different levels if it is required to write to the disc as well as read from it) which can be read by a standard red diode laser using a focusing lens [1.3]. They expect one of these discs to be able to hold 6.5 Gbytes or more. They also predict the possibility of discs with many more layers, together with shorter wavelength lasers, to be able to store more than 30 Gbytes of data.

Wide band-gap II-VI semiconductors may be used as optical switches. Such switches will be required in the next generation of optical computers. ZnSe is known to exhibit optical bistability in electric fields and this may be utilised in an optical switch at visible wavelengths, see *Section 2.4*. This then allows the switching on and off of light beams to transfer digital information.

Common to most of the devices discussed above is the requirement to fabricate the device from the raw starting material. There has been little work done on the fabrication of II-VI semiconductors at the dimensions of interest to modern electronics i.e. sub-micron and hence little work has been done to investigate sub-micron structures in these materials. It is hoped this thesis will provide some insight into the field of sub-micron II-VI physics and assist the engineering of future devices.

## 1.2 Survey of the Following Chapters

This first chapter has been a general introduction to give some idea of why the need exists to carry out research to enable the understanding of wide band-gap II-VI

semiconductors.

Chapter 2 brings the reader up to date in the topics encompassed in this thesis. The growth techniques used to prepare samples are given together with the landmarks in the advances made which have culminated in the growth of state-of-the-art material available today. The chapter then goes on to discuss the current state of the fabrication technology and the developments and break throughs made to arrive at this point. There then follows an outline of the theoretical aspects behind the research into nanotechnology applied to semiconductors. As much relevant information as possible is given in this section though it impossible to include all of the information which may be required. In anticipation of this situation occurring there are relevant references given in association with the details, the reader is then able to pursue any questions arising which are not covered in enough detail in the text.

In Chapter 3 the equipment used in the duration of this project is detailed. The chapter is divided into several parts for reasons of clarity. The chapter begins with a list detailing all of the samples used in this project including the information supplied by the growers. The methods used to clean and mount the samples for the experiments follow and there is then a description of the resists and masks used during the lithographic work. The chapter continues with descriptions of the spectroscopy equipment and then goes on to describe the fabrication equipment used. Relevant theoretical aspects are explained in the text as it progresses. The majority of the chapter is taken up with an explanation of the theory required to understand the experiments and results included in the thesis.

The results obtained are given in Chapter 4. Those obtained from ZnSe are given first and these are further divided into those obtained from photoluminescence and Raman scattering experiments for as-grown, etched and annealed samples. Due to the few samples available only flat etches were assessed, there were no nanostructures patterned

on the ZnSe. The chapter then goes on to deal with the other material system considered in this work, ZnTe. The layout is the same as for ZnSe, first the photoluminescence is reported and then the Raman scattering for the as-grown, flat etched and annealed samples. Further samples of ZnTe were then patterned and the development of the patterning technology is reported. After etching the samples were examined using Raman scattering and the results of these experiments are given. Parameters such as sample temperature, the excitation frequency and power, polarisation, orientation of the sample and the effect of the wires were varied to give a fuller understanding of the system. The absence of good quality superlattices and the limit reached in the smallness of the nanostructures meant that phonon confinement effects could not be investigated. The chapter ends with the results obtained from the fabrication and subsequent spectroscopic investigation of cylinders fabricated in ZnTe.

The penultimate chapter, Chapter 5, is used to discuss the individual results and to combine them wherever possible to explain why the results have occurred, and the implications arising from the findings. It begins with a discussion of the starting material, highlighting the good points of the materials supplied as well as their disadvantages. This section suggests sample parameters which are critical for this type of experiment. The effects of dry-etching on the photoluminescence and Raman scattering spectra are then discussed.

The experiments were initially aimed at revealing any signs of crystalline damage induced by the etching process. The flat etched samples were encouraging in that there was no sign of crystalline damage. There was evidence of a link between the photoluminescence and the amount of hydrogen used in the etching gas which was investigated by annealing the samples and the photoluminescence did recover, suggesting the desorption of hydrogen.

There were however, some unexpected features which arose in the Raman spectrum after the fabrication of wires and dots in ZnTe. These features were assigned, using the literature, as crystalline tellurium. After many experiments designed to establish the location of the Te, it was found to occur on the vertical surfaces of the etched features. In order to explain this, a hypothesis is put forward of preferential etching of the Zn, or the deposition of a Te containing compound which protected the sidewall from lateral etching. These findings are linked to the *x-ray photoelectron spectroscopy*, (XPS), findings of Sotomayor Torres et al. [1.4].

In Chapter 6, the conclusions from this work are given. Finally proposals are given for future work for which there has either simply not been enough time to attempt during the course of this project, or which the evolution of ideas has only recently suggested.

An appendix has been attached to show the spectra obtained from the samples which are listed in the main text but whose spectra are not referred to. These spectra were deemed not be of a good enough quality, either showing relatively broad or low intensity peaks in their photoluminescence or Raman scattering spectra. This in turn meant that any expected broadening or intensity reducing effects would have been difficult to observe. However, they have been included to give an overall impression of the quality of the materials presently available. Also included in the appendix are SEM photographs showing nano-dimensional structures etched into ZnCdSe/ZnSe superlattices as proof of the versatility and quality of the etch process developed.

# Chapter 2

# Literature Review

## 2.1 Overview

In this chapter there are relevant details of other important work carried out in relevant fields both previously and currently. It becomes clear the field of II-VI semiconductors underwent intense investigation approximately three decades ago but this effort was not sustained and only in the past five to ten years has the interest been rekindled.

Major advances have been made in the growth techniques and only now, due to better quality samples becoming available, are results concerning device related issues being published. There is a definite correlation between those establishments producing good quality materials and those publishing device results. The devices so far reported have been adapted and developed from technologies established in III-V science. Due to this, the development of devices has shown, and should continue to show, rapid progress. There is now developing a need to integrate III-V and II-VI semiconductors to produce devices which utilise the benefits of both material systems. In order to integrate the II-VI semiconductors it is necessary to fabricate features on a similar scale to that commonly achieved with the III-V materials. The field of nanotechnology is relatively new for any material system and it is hoped this project will make a definite contribution to the research into this field.

## 2.2 Advances in II-VI Growth

The development of the growth technology for wide band-gap II-VI semiconductors has benefited greatly from the experience gained in the development of III-V semiconductors. The purest material today is produced by MBE, which is an extremely expensive way of producing semiconductors and hence has few commercially viable markets. Commercial awareness has driven the development of MOCVD due to its relative ease of use and more economical running costs.

These techniques have both made huge advances and now are capable of growing very good quality undoped material as assessed by optical methods. The previous sentence alludes to the major obstacle in the path towards production devices. For many years now the crystal growers have been perplexed by how to dope the wide band-gap II-VIs, this problem arises because many of the II-VIs are self-compensating [2.1, 2.2]. The other critical problem has been the absence of an obvious lattice-matched heterostructure system. ZnSe has benefitted from its lattice spacing of 5.668 Å [2.3] being close to that of GaAs at 5.653 Å [2.4] resulting in a lattice mismatch of only 0.26% at room temperature. This is much smaller than the lattice mismatch between ZnTe and GaAs which is 7.90% due to the lattice spacing of ZnTe being 6.104 Å [2.5] at room temperature. GaSb has a lattice constant of 6.096 Å [2.5] resulting in a mismatch of 0.13% with ZnTe at room temperature but unfortunately GaSb substrates are relatively expensive and so are not widely used.

Universität Regensburg prepared ZnTe samples grown on GaAs substrates for (100) cross sectional *transmission electron microscopy* (TEM) analysis using a *Phillips CM30 TEM* operating at 300 keV. The sample was mechanically thinned before argon ion milling was performed to perforate the sample. The bright field image obtained of a 750 nm layer of ZnTe on a GaAs substrate is given in *Figure 2.1*. This figure clearly

shows a region of approximately 200 nm in which misfit dislocations prevail. The density of these dislocations decreases as the distance from the interface increases and defect free areas can be observed further from the interface.

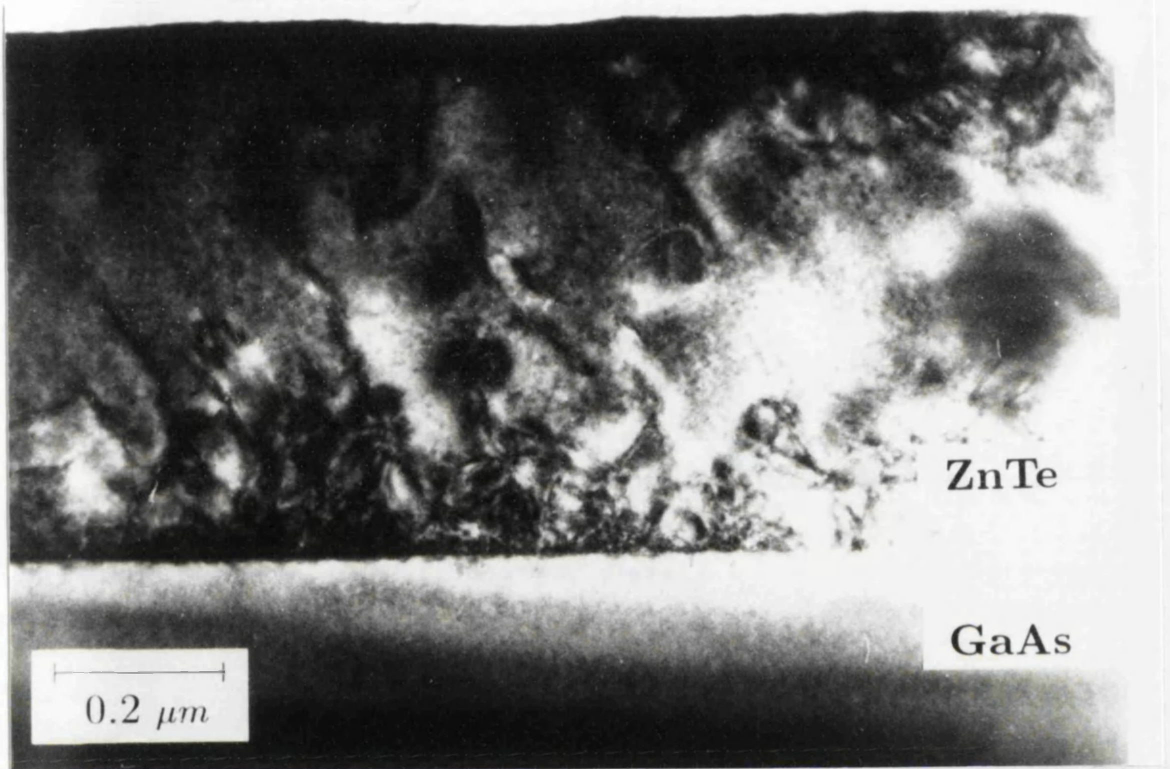


*Figure 2.1* Bright-field image of cross sectional TEM showing ZnTe/GaAs interface of ZnTe layer grown by MOCVD.

A sample of ZnTe which was 1.97 μm thick, again grown on a GaAs substrate, was characterised after growth by the growth group at Universität Regensburg. They used a Normarski interference contrast microscope to investigate the quality of the surface morphology. A photograph of the image was taken and is shown in *Figure 2.2*, as can be seen from this figure the surface was quite rough compared to high quality III-V materials.

The growth group at Universität Regensburg carried out reflectivity experiments which revealed a strain related splitting of the excitonic structure into heavy and light hole transitions at 2.379 eV and 2.374 eV respectively. The reflectivity spectrum obtained is

shown in *Figure 2.3*. Low temperature photoluminescence experiments at 2 K were also carried out. The resulting spectra, an example of which is given in *Figure 2.4*, enabled the identification of emission from the biaxial strain split free exciton at 2.379 eV and 2.374 eV, an exciton bound to an arsenic acceptor at 2.368 eV and another exciton bound to an unidentified acceptor at 2.357 eV. There was also a band of luminescence assigned to a donor-acceptor pair centred at approximately 2.305 eV.

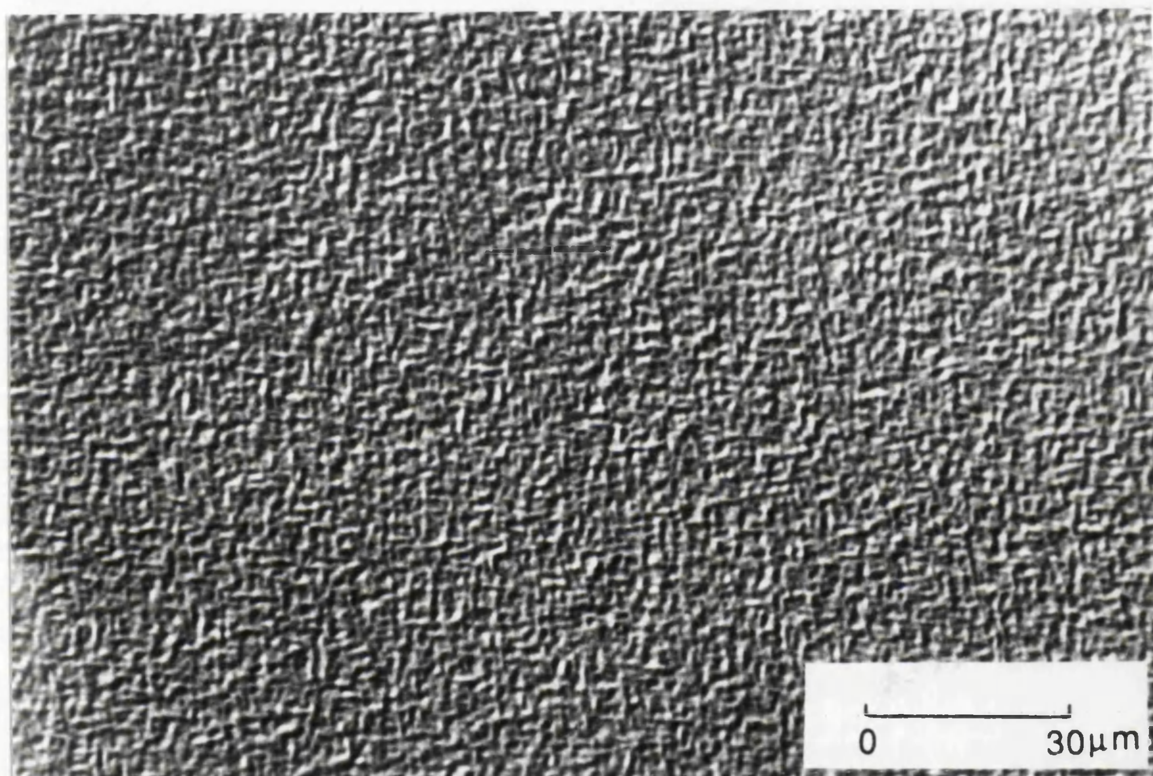


*Figure 2.2* Photograph showing the surface morphology of a ZnTe layer, taken using a Normarski interference contrast microscope.

One of the most studied materials is ZnSe, this was mainly because of its extremely wide band-gap of 2.4 eV at 4 K [2.3], forecasting the possibility of huge potential confinement effects and its near lattice match with GaAs substrates allowing relatively low strained samples to be grown. The late eighties saw the emergence of papers reporting the successful doping of ZnSe, first *n*-type [2.6] and then at low levels of *p*-type using Li and N dopants [2.7, 2.8, 2.9, 2.10, 2.11, 2.12]. The production of nitrogen free radicals by an rf

source led to $p$-type levels of $1\times10^{18}$ $cm^{-3}$, an order of magnitude greater than that attained using Li. This then allowed the fabrication of simple blue light emitting diodes (LEDs) from a *pn*-junction [2.7, 2.10, 2.13]. Unfortunately the problem of doping a self-compensating material still plagues growers of many other II-VI semiconductors including ZnTe.

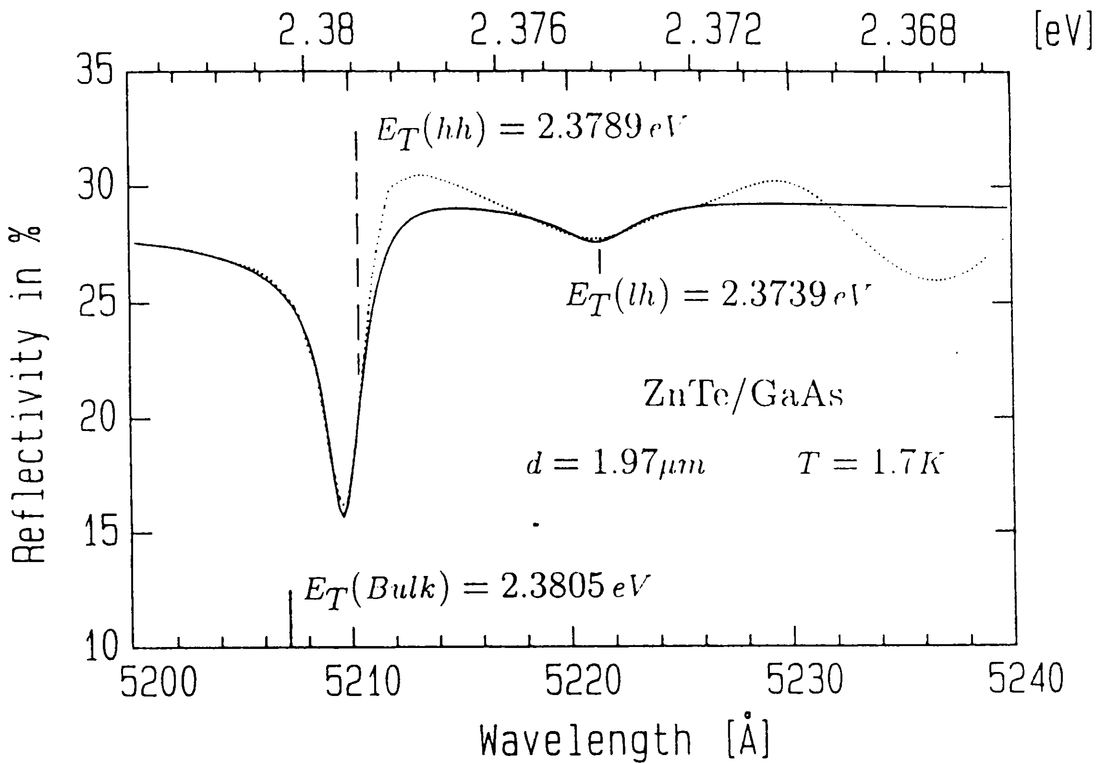


*Figure 2.3* Low temperature (1.7 K) reflectivity spectrum of an as-grown ZnTe sample. Heavy and light hole transitions occur at 2.379 eV and 2.374 eV respectively. The solid line is the theoretical data and the dotted line is experimental data.

It was as early as the 1960s that laser action was demonstrated in several of the wide band-gap II-VI semiconductors. These early experiments used e-beam pumping [2.14]. Several more examples of lasing action were reported using e-beam pumping and also photo-pumping [2.15] but mainly due to the problems mentioned in the preceding paragraph, there were no reports of a diode laser, the device demanded by industry.

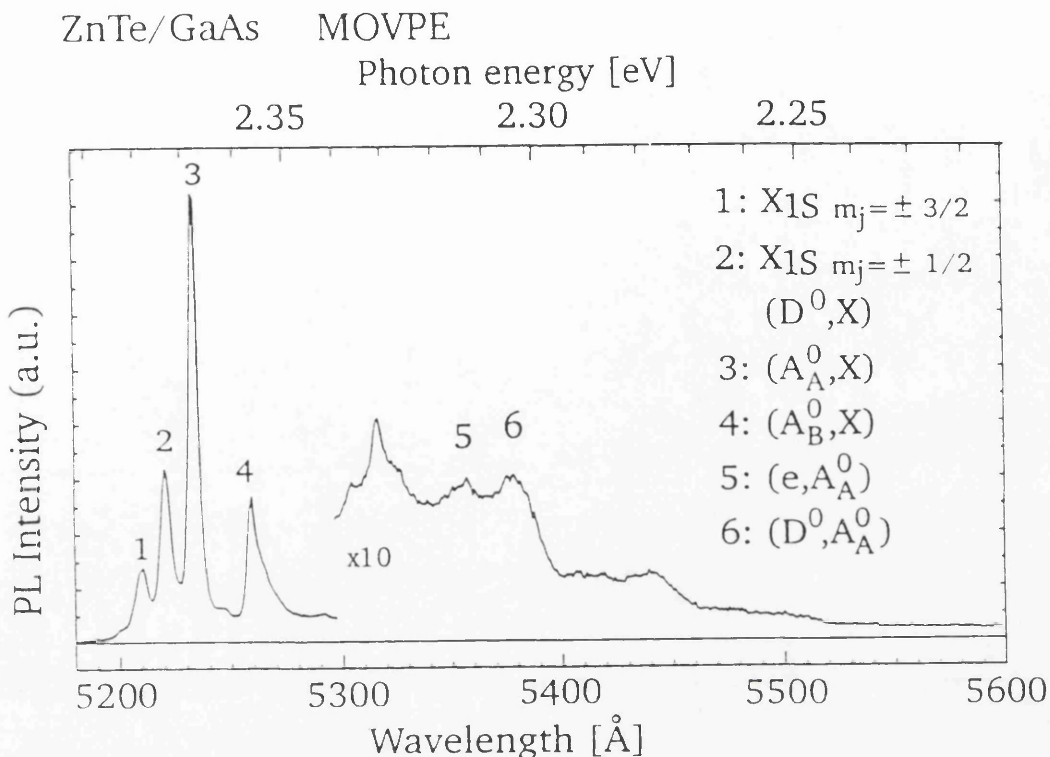


*Figure 2.4* Low temperature (2 K) photoluminescence spectrum of ZnTe. 4579 Å excitation. Peaks 1 and 2 are luminescence from the biaxial strain split free excitons, peaks 3 and 4 are due to an exciton bound to an arsenic acceptor and another unidentified acceptor respectively. Peak 6 is donor-acceptor pair recombination.

Several groups came extremely close to producing a diode laser. The group at Brown University led by Nurmikko published their evidence of room temperature blue lasing using optical pumping of (Zn,Cd)Se/ZnSe multiple quantum well structures [2.16]. The same group also reported laser action from an optically pumped single quantum well of the same heterostructure [2.15]. Several other groups have reported photo pumping laser action from II-VI semiconductors [2.17, 2.18].

It was in 1991 that 3M [2.19] published their claim to be the first to fabricate a laser diode using II-VI semiconductors. They used pulsed current injection to obtain coherent

light at a wavelength of 490 nm from a single quantum well structure at 77 K, the device also lased briefly at 200 K. The structure was grown by MBE and consisted of a 1 μm GaAs:Si buffer layer grown on a (100) Si doped $n^+$-GaAs substrate. On top of this were grown $n$-type layers, doped with chlorine from a $ZnCl_2$ source. From the buffer there was a $10^{18}$ $cm^{-3}$ ZnSe contact layer, a $10^{18}$ $cm^{-3}$ $ZnS_{0.07}Se_{0.93}$ cladding layer which was almost lattice matched to the substrate and a $10^{17}$ $cm^{-3}$ ZnSe guiding layer. This was then mirrored in $2x10^{17}$ $cm^{-3}$ $p$-type material (with the exception of the top contact layer which was doped to $10^{18}$ $cm^{-3}$) obtained by doping with N from an rf plasma source using nitrogen gas. Sandwiched between the n- and p-type ZnSe was the 100 Å thick $Cd_{0.2}Zn_{0.8}Se$ quantum well which was responsible for emitting the light. Mirrors were formed on the samples by cleaving facets to make cavities about 1 mm long. The structure is shown schematically in *Figure 2.5*. The author sums up the work with *"this breakthrough advances the status of ZnSe and related materials well beyond merely "promising""*.

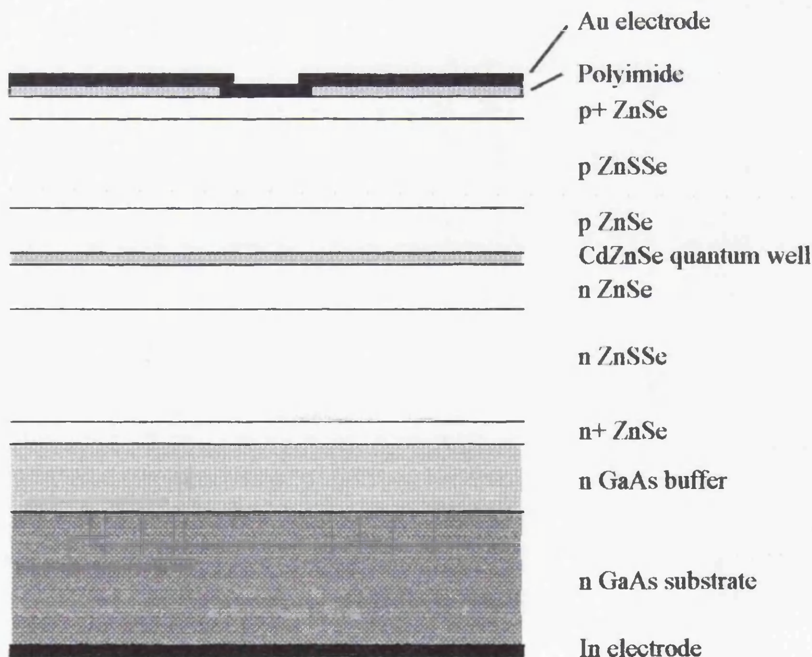


*Figure 2.5* Schematic diagram of the II-VI laser diode fabricated by 3M.

There is an effort to combine II-VI and III-V growth to produce novel devices

which has necessitated the development of adapted hardware. An example of such work is that being carried out at Universität Würzburg where they use a multichamber MBE kit. The idea behind the multichambers is to keep the sample under vacuum at all times so as not to reduce its purity but to allow the dedication of one chamber to growing certain compounds, this serves to preserve the purity of the sources and of the chamber and hence of the final epilayers.

## 2.3 Advances in Fabrication Techniques

Originally semiconductor devices were fabricated by removing material in a bath of liquid chemicals hence this technique became known as *wet etching*. The areas which were desired to be left intact were protected by some form of mask and the exposed areas were subjected to a chemical reaction and the by-products of the reaction were removed into the chemical liquid, all of which was later rinsed with some neutral liquid, commonly de-ionised water. Wet etching is relatively cheap, it requires very little capital outlay and proves adequate for many fabrication purposes.

Practical problems arise with this technique when the temperature of the system fluctuates, the agitation, which is commonly present, is not reproducible, the time is not reproducible or if the concentration of the chemicals is depleted by the process as it is carried out. Also the chemicals themselves can be hazardous to the user i.e. hydrofluoric acid. Fundamentally wet etching is an isotropic etching technique, which means it will etch at an equal rate in all directions, although it does have some preference for some crystallographic planes. This is probably not a problem when etching relatively large features, of say 10 μm, to a shallow depth, say 0.5 μm, because the slight curvature of the sidewalls and base of the structure is negligible compared to the other dimensions. This problem reaches far greater importance however, as the dimensions of the structures are

reduced and *critical dimension*, (CD) losses and profiles become critical.

The technique of dry etching was invented [2.20] as a solution to the problem of isotropic etching. Carefully chosen gases are placed between two electrodes across which is applied an rf voltage. The sample is placed on one of the electrodes. The voltage causes the gases to ionise and the oscillating nature of the field removes the negatively charged electrons from the gas, thus forming a plasma. The electrons are removed courtesy of their smaller mass making them more mobile than the positive ions. The heavier, less mobile positive ions are then drawn by a DC bias towards the sample electrode where they make contact with the sample. If the gases are chosen correctly there then occurs a chemical reaction at the surface between the incident ions and the sample. The ions also have kinetic energy given to them by the accelerating field and so are able to bombard the sample and physically remove material. This is a second component to the technique and care must be taken to ensure this bombardment does not damage the sample. The great benefit of dry etching is that the incident positive ions travel parallel to one another and this allows a large degree of anisotropy. Thus dry etching allows very small, sub-micron, structures to be fabricated with vertical sidewalls and horizontal bases.

The relatively simple technique outlined above which is termed *reactive ion etching*, (RIE), develops problems at very small dimensions of the order of 0.5 μm and it has become necessary to operate at lower pressures, typically a few millitorr. This had the effect of reducing the amount of ions available to the reaction and now there are various methods which intensify the plasma to increase the number of ions available, typically of the order of $10^{12}$ $cm^{-3}$ so it becomes possible to reduce the pressure. The first technique developed for this purpose was *electron cyclotron resonance*, (ECR), which used magnetic and electric fields to confine the plasma. Recently *transformer coupled plasmas*, (TCP), and *inductively coupled plasmas*, (ICP), have emerged. With these techniques a second rf generator is used to power a coil separated from the gases by a ceramic shield.

The second rf field couples inductively through the ceramic to the first rf field and assists the formation of the plasma. These techniques have been reviewed by Singer [2.21].

There have been few reports of dry-etching II-VI semiconductors. One was by a group at Brown University, led by Nurmikko who published a paper [2.22] reporting the dry etching of ~100 nm wires in ZnSe and ZnCdSe/ZnMnSe heterostructures with a simple $BCl_3$ chemistry at a pressure of 3 mTorr and a power density of 600 mW/cm$^2$ with the sample at 20°C. The samples were grown by MBE and gratings were patterned using holographic techniques to expose the photoresist. A continuous wave ultra-violet argon-ion laser emitting at 350 nm or a dye laser emitting at ~440 nm were used to form the interference patterns in a Mach-Zehnder interferometer-like arrangement. Two such patterns, one rotated by 90° with respect to the other led to the patterning of dots. They reported a low loss of photoexcited carriers due to etch-induced damage from the results of their time-resolved photoluminescence experiments. Other groups have used $BCl_3$/Ar [2.23] and $CH_4/H_2$ [2.24]. None of these etches produce a vertical sidewall necessary for most fabrication processes.

Sotomayor Torres et al. [1.4] characterised samples of ZnSe and ZnTe using the technique of *x-ray photoelectron spectroscopy* (XPS), before and after uniform flat reactive ion etching in $CH_4/H_2$. An *Escalab Mk II* machine provided the Al Kα x-ray line at near normal acceptance angle. Emission from the Te (3d,4d), and Zn (2p,3d) core levels was monitored for ZnTe samples etched with methane to hydrogen ratios of 1:6 and 1:8 as well as a control sample which was not etched. The use of electrons with two different kinetic energies enables two spatially resolved depths to be monitored, these depths being approximately 1 nm and 3 nm below the surface, Gant and Mönch [2.25]. The ZnSe samples examined were etched with 1:8 and 1:10 ratios of methane to hydrogen and again there was an unetched control sample. The emission from the Se (3d) and Zn (2p,3d) core levels was monitored. No change was observed in the binding energies of the

Zn, Se and Te which were identified using the literature, Patterson and Williams [2.26] and Wagner et al. [2.27]. The areas of the Te 4d, Se 3d and Zn 3d peaks were calculated after curve fitting the emission spectra. The atomic fractions were then used to calculate the Te oxide to Te ratio, the Se oxide to Se ratio, the Zn oxide to Zn ratio and finally the Te to Zn ratio. The ratios were corrected to take into account the difference in the photoionisation cross-sections and the difference in the escape depths of the emitted electrons. The results are summarised below; those for ZnTe are presented in *Table 2.1* and those for ZnSe are presented in *Table 2.2*.

These results will be referred to later in Chapter 5 but the following points should be noted. The amount of Te present in the region of investigation has increased, this has been accompanied by a decrease in the amount of Zn present and so the ratio of Te to Zn has increased. A similar effect is seen in the ZnSe where again there is an enrichment of the Group VI element.

| **Etch** | **Te** | **Te Oxide** | **Zn** | **Zn Oxide** | $\frac{\textbf{Te Oxide}}{\textbf{Te}}$ | $\frac{\textbf{Zn Oxide}}{\textbf{Zn}}$ | $\frac{\textbf{Te}}{\textbf{Zn}}$ |
|---|---|---|---|---|---|---|---|
| Control | 61 | 38 | 100 | 0 | 0.623 | 0 | 0.137 |
| 1:6 | 100 | 0 | 100 | 0 | 0 | 0 | 0.226 |
| 1:8 | 77 | 22 | 89 | 11 | 0.286 | 0.123 | 0.195 |

*Table 2.1* Peak areas of the Te 4d and Zn 3d core levels and atomic fraction ratios for the unetched control sample of ZnTe and samples etched in 1:6 and 1:8 ratios of $CH_4:H_2$.

There now follows a brief review of the advances made in the lithographic field which have enabled the reduction of device dimensions. The masks referred to above are mostly written using an organic compound, referred to as photoresist, the chemical nature

of which is altered when it exposed to light, similar to a photographic negative. A template or reticle is manufactured and placed above the unexposed photoresist. The reticle is then flooded with light which exposes the areas of photoresist not protected by the reticle. The reticle can be scaled up from the required device size to ease manufacturing requirements. To reduce the image reducing optics are placed between the reticle and substrate. The photoresist can then be developed either leaving behind the exposed resist or the unexposed resist depending on whether the resist was *positive* or *negative*. The wafer can then be moved and the same pattern exposed again, this is referred to as stepping and is possible because the majority of chip manufactures require multiples of a relatively small chip design.

| **Etch** | **Se** | **Se Oxide** | **Zn** | **Zn Oxide** | $\frac{\text{Se Oxide}}{\text{Se}}$ | $\frac{\text{Zn Oxide}}{\text{Zn}}$ | $\frac{\text{Se}}{\text{Zn}}$ |
|---|---|---|---|---|---|---|---|
| Control | 72 | 28 | 100 | 0 | 0.388 | 0 | 0.257 |
| 1:8 | 100 | 0 | 100 | 0 | 0 | 0 | 0.358 |
| 1:10 | 92 | 8 | 96 | 4 | 0.086 | 0.041 | 0.343 |

*Table 2.2* Peak areas of the Se 3d and Zn 3d core levels and atomic fraction ratios for the unetched control sample of ZnSe and samples etched in 1:8 and 1:10 ratios of $CH_4$:$H_2$.

Advances in the manufacturing of the reticle and reducing optics have led to smaller features being patterned. The resolution of the technique is dependent upon the wavelength of light used and there has been a concerted effort to reduce the wavelength of the sources used in order to increase their resolution. The *G*-line of a mercury arc lamp gives light at 436 nm which was adequate to pattern features with dimensions >1 μm. As the required dimensions fell below 1 μm the *H*-line at 405 nm was used. As the current production technology pushes 0.35 μm features the *I*-line at 365 nm has become the

benchmark [2.28].

Holography has been used as a means of avoiding the mask problem. Constructive and destructive interference of light is used to produce patterns. The constructive interference is used to expose the photoresist whereas the areas which suffer destructive interference are not able to fully expose the photoresist and this then leads to a differentiation between the areas upon development of the resist. This technique is therefore similar to that of photolithography, as is discussed above, with the exception of the method of forming the pattern. Due to the coherent nature of lasers, relatively large areas of square centimetres can be patterned very accurately with this technique [2.29].

X-rays have also been suggested as a way forward but there are numerous drawbacks which have precluded this technique becoming an industry standard. There is no material available to x-ray lithography which is analogous in that it has the transmissive properties of glass in optics, hence it is not possible to manufacture reducing optics. Membranes have been used but these are very expensive. The sources available are poor in comparison with optical sources. The synchrotron, laser and plasma sources which are available prove to be complex and expensive. There is also a requirement for more sensitive resists which places more emphasis on developing better sources. The resists available are relatively insensitive and are not suitable for subsequent processing such as stripping. Finally the use of x-rays leads to quite significant radiation damage [2.28].

A technique similar to photolithography but utilising the smaller wavelength and the accompanying higher resolution of an electron beam has been developed. This technique scans a focused beam of electrons to expose electron-beam resist which is then developed similarly to photoresist [2.28]. Since this is a scanning method it is more time consuming than the simpler flooding method used in photolithography. Advances in electronics, electromechanical drives and micropositioners have meant accuracy of

positioning has been increased allowing larger areas to be patterned.

The main competition for electron-beam lithography comes from ion-beams. The shorter mean-free-path of the ions reduces both proximity effects and the degradation of the resolution [2.28]. Unfortunately the sources are much weaker than those of e-beam and this leads to a much lower throughput which burdens this technique with a severe disadvantage.

It has recently been suggested that structures may be written directly onto surfaces by bringing together atoms one at a time and so by using an atomic beam, a wire could be one atom wide. This idea has been postulated, but not yet achieved, with the advent of the *scanning tunnelling microscope*, (STM). So far only acronyms have been written using argon atoms, notably by IBM [2.30] and real atomic-circuits are still to come.

## 2.4 Summary of Theoretical Interest in Nanotechnology

It is now commonly accepted that reducing the motion of electrons to two dimensions in a *two dimensional electron gas*, (2DEG), increases the mobility of the electrons as a result of reducing their scattering by impurities. This is due to a spatial separation brought about by electrostatic repulsion. This has led to the postulation and fabrication of such novel devices as the *high electron mobility transistor* (HEMT).

It was Sakaki [2.31] who first realised the benefits of moving towards even further reduced dimensionality. He appreciated the fact that in one dimensional structures i.e. wires, the conservation of energy required that if an electron was elastically scattered, it could only be scattered from its initial state $\mathbf{k}_i$ to a final state $-\mathbf{k}_i$. The accompanying large change in momentum, $2k_i$, prohibited the long range part of the scattering potential from

taking part in the interaction. There must therefore be a significant reduction in the amount of scattering taking place in one dimensional structures. This is all very interesting from a scientific viewpoint but the huge implication of this theory is the electron mobility is increased due to the reduction in scattering, this factor is of major interest to the device manufacturers.

Concerning light emission, it has been widely shown that laser diodes operate with much lower threshold currents and higher efficiencies when the carriers are confined in potential wells. The confinement also serves to increase the excitonic binding energy and it has been noted [2.32] that by enhancing the binding energy of excitons in ZnSe using this method, the energy of LO phonons at room temperature would not be enough to dissociate the exciton. The exciton would then be able to exist at room temperature. This could not occur in GaAs because the bulk exciton binding energy is ≈5 meV, (c.f. 17 meV for ZnSe) and the LO phonon energy is ≈36 meV (c.f. 31 meV for ZnSe). The excitons are therefore able to partake in exciton-exciton scattering and exciton-electron scattering, both of which led to highly desirable optical gain in laser diodes. The existence of excitons at room temperature and a more detailed discussion of the lasing mechanisms involved is given by Kawakami et al. [2.33].

The confinement of phonons in periodic superlattices allows the dispersion curve of the phonons to be investigated using laser light which has an associated wavevector close to zero. Without the confinement, the light would not be able to couple with phonons with wavevectors greater than zero. Previously the only way of measuring the dispersion would have been by using neutron scattering. Neutron scattering is a more difficult experiment than Raman scattering and also requires large samples as target. This can be impossible if the crystals are difficult or expensive to grow, as is often the case with the development of new material systems. A more detailed discussion on confinement effects is given in *Section 3.5.3.*

The carriers in systems of reduced dimensionality will lose energy when they are scattered by the longitudinal optic phonons and so the change in the scattering cross-section and the spatial properties of the phonons when they are confined is of vital importance. It is necessary to understand and be able to model the effects of confinement on the longitudinal optic phonons in order to include these effects when calculating the energy loss of carriers subjected to such dimensional constraints.

One of the first devices to be manufactured utilising II-VI semiconductors is the quantum confined Stark effect modulator [2.34] which has been developed from III-V technology, see Miller et al. [2.35]. For this device a series of 60 Å ZnCdSe quantum wells separated by 80 Å barriers were grown, sandwiched between a *pn*-junction formed by the appropriate doping of ZnSe. The device was grown on a GaAs substrate which had a window wet etched through it in order to provide a means of transmitting light through the device. The two dimensional confinement provided by the quantum well structure leads to an enhancement of the exciton binding energy which then leads to strong exciton absorption at room temperature. When an electric field is applied perpendicular to the layers, it forces a change in the shape of the quantum well. The wavefunctions of the electrons and holes are therefore changed and this leads to a decrease in the binding energy and absorption strength of the exciton.

Wang et al. [2.36, 2.37] went on to exploit the bistable nature of ZnSe in a similar device which was used as an optical switch for light at 488 nm. A *diode based self-electro-optic effect device* (D-SEED) was fabricated by placing a Si photodiode in series with the quantum confined Stark effect modulator, a schematic diagram of the arrangement is given in *Figure 2.6*. The photodiode provided a constant-current source which served to bias the D-SEED thereby rendering it in a high transmission state. This voltage across the SEED was independent of the photocurrent generated by the *p-i-n* diode because of the constant-current source. When the photocurrent became comparable with the bias

current the majority of the voltage was then dropped across the photodiode thereby rendering the SEED in a low transmission state. This situation persisted even when the input optical power was reduced below the level where the high-to-low transmission transition occurred, hence the bistable terminology. Eventually the positive feedback operates in reverse and the SEED reverts back to the higher transmission state. The bistability of the device allows its operation in either transmission mode between these powers i.e. it can be used as an optical switch.

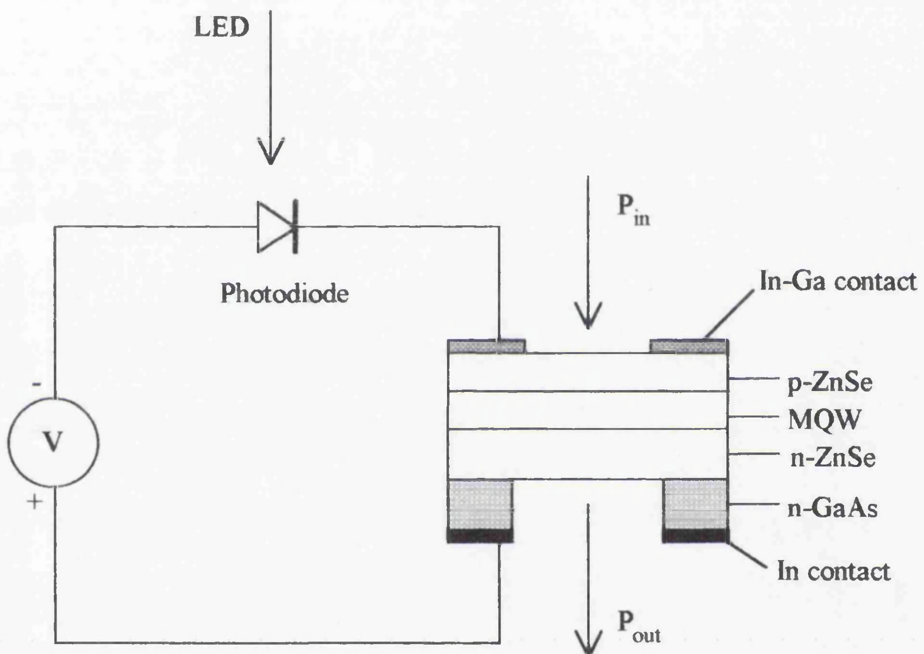


*Figure 2.6* Schematic diagram of the D-SEED fabricated by Wang et al. and the electronic cicuit to drive it.

# Chapter 3

# Experimental Methodology

### 3.1 Introduction

The aim of this chapter is to convey to the reader all of the information necessary for an appreciation and understanding of the experiments performed. The chapter begins with a section detailing the samples used during this project. Also included are all of the relevant details provided by the growers. There is a short sub-section outlining the relevant procedure adopted to prepare the samples for the experiments. The chapter continues with a comprehensive catalogue of all the equipment used in the experiments including details of all relevant specifications. For clarity the equipment section is sub-divided into spectroscopic equipment and fabrication equipment. The second section of the chapter deals with the theory behind the experiments using SI units. Again for clarity this section is sub-divided into smaller sections dealing separately with photoluminescence and Raman scattering. The latter sub-section begins almost from first principles and develops the theory to explain the phenomena of resonance and polarisation effects. Theoretical predictions concerning the effect of crystalline damage on the Raman spectrum are then explained and this is followed by an explanation of the origins of the arguments concerning the confinement of phonons in systems with reduced dimensionality.

### 3.2 List of Samples

ZnTe/GaAs
Sample Reference: ZT 34
Thickness: 2.1 μm
Origin: Universität Regensburg
Growth Method: MOCVD
Growth Temperature: 350°C

ZnTe/GaAs
Sample Reference: ZT 95
Thickness: 1.7 μm
Origin: Universität Regensburg
Growth Method: MOCVD
Growth Temperature: 350°C

ZnTe/GaAs
Sample Reference: ZT 46
Thickness: 0.8 μm
Origin: Universität Regensburg
Growth Method: MOCVD
Growth Temperature: 350°C

ZnTe/GaAs
Sample Reference: ZT 193
Thickness: 2.2 μm
Origin: Universität Regensburg
Growth Method: MOCVD
Growth Temperature: 350°C

ZnTe/GaAs
Sample Reference: ZT 55
Thickness: 1.8 μm
Origin: Universität Regensburg
Growth Method: MOCVD
Growth Temperature: 350°C

ZnSe/ZnTe
Sample Reference: Q97
Thickness: 0.6 μm/0.7 μm
Origin: Universität Regensburg
Growth Method: MOCVD
Growth Temperature: 350°C

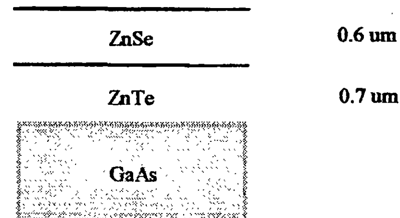


ZnSe/GaAs
Sample Reference: ZS 129
Thickness: 0.53 μm
Origin: Thomson-CSF
Growth Method: MOCVD
Growth Temperature: 400°C

ZnSe/GaAs
Sample Reference: ZS 134
Thickness: 0.58 μm
Origin: Thomson-CSF
Growth Method: MOCVD
Growth Temperature: 400°C

$ZnS_{0.95}Se_{0.05}/ZnSe/ZnS_{0.31}Se_{0.69}$
Sample Reference: P26
Origin: UMIST
Growth Method: MOCVD
Growth Temperature: 450°C
Substrate: GaAs

| Layer | Thickness |
|---|---|
| ZnS(0.95)Se(0.05) | 114 A |
| ZnSe | 104 A |
| ZnS(0.31)Se(0.69) | 500 - 700 A |
| GaAs | |

$ZnS_{0.68}Se_{0.32}/ZnSe/ZnS_{0.68}Se_{0.32}$
Sample Reference: ZS 377
Origin: RWTH Aachen
Growth Method: MOCVD
Growth Temperature: N/A
Substrate: GaAs

| Layer | Thickness |
|---|---|
| ZnS(0.68)Se(0.32) | 1000 A |
| ZnSe | 10 A |
| ZnS(0.68)Se(0.32) | 10000 A |
| GaAs | |

$ZnS_{0.42}Se_{0.58}/QW*/ZnS_{0.42}Se_{0.58}$
Sample Reference: ZS 379
Origin: RWTH Aachen
Growth Method: MOCVD
Growth Temperature: N/A
Substrate: GaAs

| Layer | Thickness |
|---|---|
| ZnS(0.42)Se(0.58) | 1000 A |
| *Growth Interruption | 5 seconds |
| ZnS(0.42)Se(0.58) | 10000 A |
| GaAs | |

$ZnS_{0.42}Se_{0.58}/QW*/ZnS_{0.42}Se_{0.58}$
Sample Reference: ZS 371
Origin: RWTH Aachen
Growth Method: MOCVD
Growth Temperature: N/A
Substrate: GaAs

| Layer | Thickness |
|---|---|
| ZnS(0.42)Se(0.58) | 1000 A |
| *Growth Interruption | 80 seconds |
| ZnS(0.42)Se(0.58) | 10000 A |
| GaAs | |

ZnCdSe/ZnSe (x20)

Sample Reference: DJI 22A / DJI 28A / DJI 30A / DJI 31A
Origin: Strathclyde University
Growth Method: MOCVD
Growth Temperature: 300°C
Substrate: GaAs

**DJI 22A**

| Layer | Thickness |
|---|---|
| ZnSe | 40 A |
| ZnSe (SLS x20) | 100 A |
| ZnCdSe (SLS x20) | 100 A |
| ZnSe | 7000 A |
| GaAs | |

**DJI 30A**

| Layer | Thickness |
|---|---|
| ZnSe | 80 A |
| ZnSe (SLS x20) | 200 A |
| ZnCdSe (SLS x20) | 170 A |
| ZnSe | 14000 A |
| GaAs | |

**DJI 28A**

| Layer | Thickness |
|---|---|
| ZnSe | 40 A |
| ZnSe (SLS x20) | 100 A |
| ZnCdSe (SLS x20) | 50 A |
| ZnSe | 7000 A |
| GaAs | |

**DJI 31A**

| Layer | Thickness |
|---|---|
| ZnSe | 40 A |
| ZnSe (SLS x20) | 100 A |
| ZnCdSe (SLS x20) | 100 A |
| ZnSe | 7000 A |
| GaAs | |

$ZnCd_{0.2}Se_{0.8}/ZnSe$ (x15)

Sample Reference: MB313
Origin: Heriot-Watt University
Growth Method: MBE
Growth Temperature: N/A
Substrate: GaAs

| Layer | Thickness |
|---|---|
| ZnSe | 2500 A |
| ZnSe (SLS x15) | 80 A |
| ZnCd(0.2)Se(0.8) (SLS x15) | 30 A |
| ZnSe | 10000 A |
| GaAs | |

The samples of ZnTe grown at the Universität Regensburg, Germany, were grown in their horizontal MOCVD kit. The (100) GaAs substrates were prepared prior to growth by cleaning in IPA and then was etched in a mixture of 4:1:1 ($H_2SO_4$:$H_2O_2$:$H_2O$) to remove any surface contaminants. The substrate was then rinsed in deionised water and finally blown dry with nitrogen. The substrate was immediately introduced to the reactor and the growth process initiated.

The precursors were DEZn and DiPTe which were kept at 17°C. These were transported to the reactor cell by the hydrogen carrier gas with a total flow rate of 7 l/min. The partial pressure ratio of the reactants was optimised to two which dictated flow rates of 17 mmol/min for the DEZn and 34 mmol/min for the DiPTe. The growth temperature was 350°C. The thickness of the epilayer was calculated from the growth rates and confirmed using an interference technique [3.1]. The ZnTe epilayer samples were 1.8 μm thick. A Normarski interference contrast microscope was used to assess the morphology of the epilayers. A photograph from the microscope is given in *Figure 2.2* by way of example. The growers also performed low temperature photoluminescence and photoreflectance experiments to characterise the samples. The results of these investigations are given in *Section 2.2*.

## 3.3 Resists and Masks

### 3.3.1 Sample Preparation

The samples to be covered by e-beam resist were first cleaned using a technique which is standard in the Ultra-small Structures laboratory. The sample was placed in a plastic beaker, rather than a glass one, to reduce the possibility of breaking the sample in the ultrasonic bath. The first cleaner used was trichloroethylene, which is a general

degreaser, the beaker was then placed in the ultrasonic bath for five minutes. Secondly the sample was cleaned in another plastic beaker filled with acetone and again the beaker was placed in the ultrasonic bath for five minutes. The sample was then placed in a beaker of Isopropyl alcohol and subjected to a further five minutes in the ultra-sonic bath. Finally the sample was removed and blown dry using a nitrogen gun.

If the sample was being prepared simply for spectroscopic purposes then it was rinsed in acetone and delicately dried by placing a lens tissue on one unimportant corner of the sample and drawing the liquid off the surface using the surface tension of the liquid, or by blow-drying the sample using nitrogen. If the sample had been etched with nanostructures however, the sample was not cleaned prior to the spectroscopic work being carried out in case the etched structures were damaged.

The sample was then attached to a mounting plate using as small a drop of glue as possible, typically 2 $mm^2$ on the top edge of the sample, away from the area to be examined. This was to reduce the strain imposed by securing the sample to the mounting plate which might have influenced the spectroscopic results. The mounting plate was then screwed to the sample holder ready for insertion into the cryostat. At this point the sample was checked to ensure that it was secured safely, only then was the insert lowered into the cryostat. The temperature of the cryostat, and hence the sample, was then lowered to 5 K for the experiment.

### 3.3.2 Resists and Masks

Resists can be divided into two groups, positive and negative resists. With a positive resist the electron-beam changes the chemical make-up of the resist so that upon developing the exposed resist is removed. In the case of negative resists, the exposed resist remains. For this work a positive resist was used.

After the sample was carefully cleaned using the procedure above, the sample was placed on the spinner. This was simply a disc which could be rotated at a chosen speed. There was also a hole in the disc which was there so that suction could be applied to prevent the sample being thrown from the disc.

One drop of positive resist was placed onto the sample using a pipette. The sample was then spun at 5000 revolutions per minute for one minute to give a uniform layer of resist over the centre part of the sample where the pattern was to be written. The sample was then baked for at least two hours, and more commonly overnight, so that the solvent was evaporated from the resist. If a second layer of resist was required then it was applied using the same procedure after the first layer had been baked.

The resist used for this work was *PMMA*. This is a positive resist which was suitable for the fabrication of wires and gratings because the electron beam only covers the area of the wire rather than all of the surface except the wires. This meant the pattern was quicker to write.

For very fine resolution work two layers of resist with different molecular weights are used [3.2]. The resist with the lighter molecular weight is applied directly to the surface of the sample. The heavier resist is then applied on top of the lighter after the latter has been baked. In the case of this work, BDH with a molecular weight of 200 000 amu was spun onto the sample and ELV was spun on top because its molecular weight is 500 000 amu. Upon exposure the lighter resist suffers greater lateral exposure than the heavier resist. This is due to the lighter molecular weight and also to proximity effects.

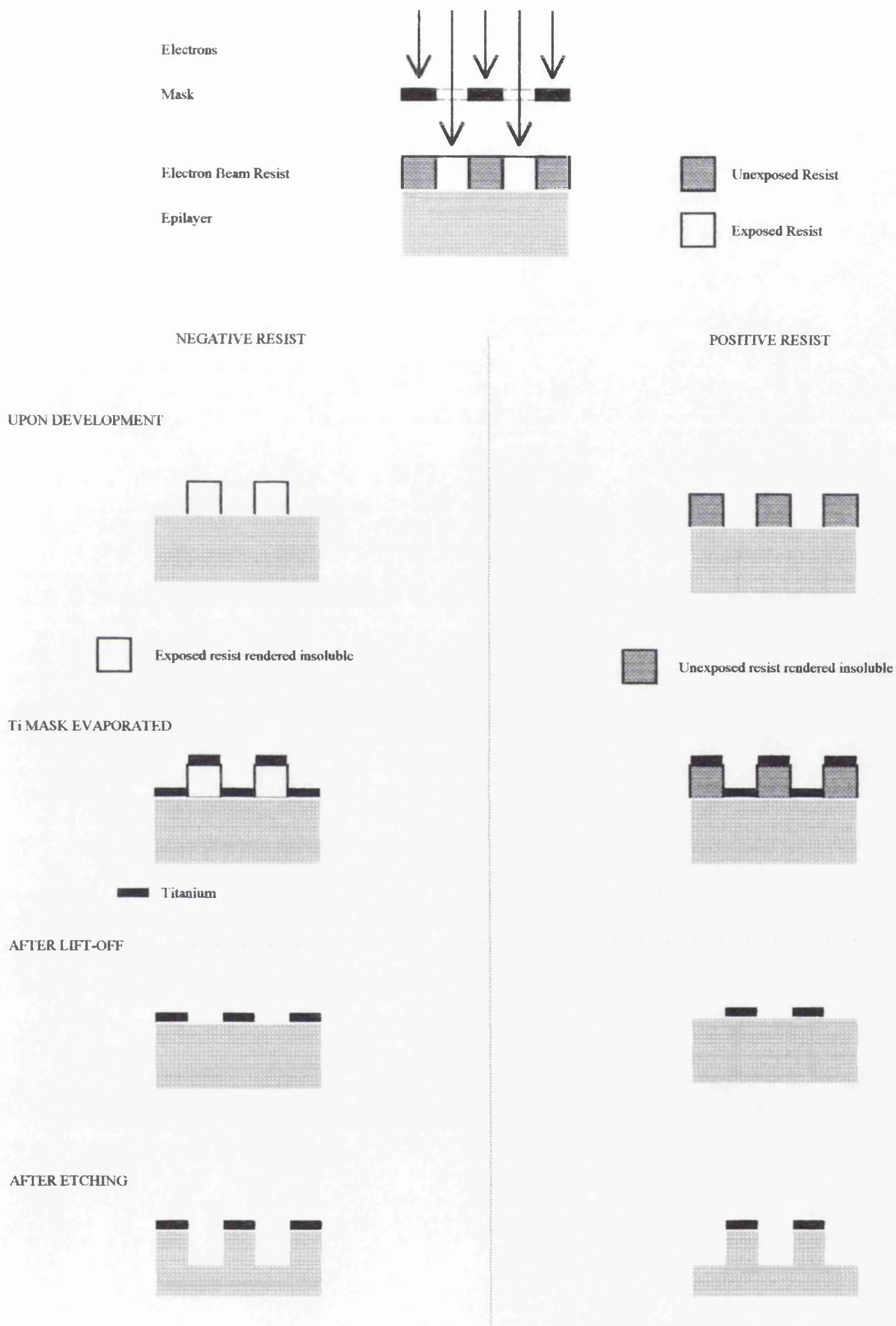


*Figure 3.1* Schematic diagram showing the stages involved in the lithographic process.

The molecular weight dictates the ease with which the molecules of the photoresist can be broken down into short polymer chains upon exposure, thereby allowing the developing process to happen. Proximity effects occur when the electrons are scattered back from the substrate and re-enter the resist. The electron, if it still has enough energy, can still expose the resist. The scattering is a random process and it has the effect of increasing the dimensions of the feature being written. The resist with the heavier molecular weight is distanced from the scattered electrons by the underlying layer and so suffers less from this effect than does the lighter resist.

The resist was then developed in a suitable developer. For positive resist the developer dissolves the exposed resist leaving behind the unexposed resist, for negative resist the opposite occurs, see *Figure 3.1*. For good resolution a 3:1 ratio of IPA to MiBK was used. The exposed sample was placed in a beaker of developer for 30 seconds, the temperature of the developer was 23°C, which was a critical factor. The sample was then removed and rinsed in IPA for 10 seconds before being blown dry with nitrogen.

A diagram showing the resulting resist profile after development is given in *Figure 3.2*. The fact that the resist with the lighter molecular weight has suffered greater lateral removal than the heavier resist is almost irrelevant because the heavier resist serves as a mask, and the opening may be regarded as being the smaller dimension if the following processing is relatively anisotropic.

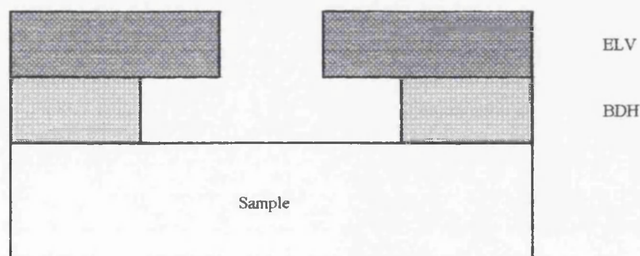


*Figure 3.2* Schematic diagram illustrating a bilayer of resist after exposure and development.

Often the resist can be used directly as a mask for the etching process. The use of $CH_4/H_2$ as a dry-etching gas proves to be relatively aggressive and quickly etches the resist and so a more robust material was sought to provide masking protection for the sample. It was decided that titanium would serve this purpose best and so a thin layer of approximately 25 nm of Ti was evaporated onto the sample. The resist provided a mask so that Ti was only deposited where the electron-beam had written. The thickness of the Ti layer was important because if it were too thick the layer on top of the sample would connect with the layer on top of the resist. If this were to happen the lift-off process would not work because the chemicals could not get through the continuous layer of Ti.

To facilitate lift-off the sample was placed in a beaker of acetone at approximately 40°C. The acetone did not attack the Ti but it did dissolve the resist and so the Ti on top of the resist simply floats off. It was found lift-off worked better if the acetone was agitated by squirting it with a syringe and hypodermic needle. The final result was the Ti adhered directly to the sample surface, masking the areas which were not to be etched by the dry-etching process. A schematic diagram of the lithographic process is given in *Figure 3.2*.

## 3.4 Equipment

### 3.4.1 Spectroscopy Equipment

#### 3.4.1.1 Laser

An argon-ion laser was used in the spectroscopy experiments, specifically a *Spectra-Physics 2045* [3.3]. It can be tuned by adjusting a prism in the cavity so that a selection of discrete spectral lines of different wavelength are available. The wavelengths

available vary from 2 754 Å in the deep ultra-violet to 10 923 Å in the far infra-red.

The lines used in this work were in the visible and ultra-violet part of the spectrum, they are listed below in *Table 3.1*, together with the power available from each line:

| **Energy (eV)** | **Wavelength (Å)** | **Power (W)** |
|---|---|---|
| 3.408 | 3638 | 1.6 |
| 2.728 | 4545 | 0.5 |
| 2.708 | 4579 | 1.6 |
| 2.541 | 4880 | 9.0 |
| 2.471 | 5017 | 1.8 |
| 2.410 | 5145 | 8.9 |
| 2.345 | 5287 | 1.1 |

*Table 3.1* Energies, corresponding wavelengths, and powers of the lines available from the Spectra-Physics 2045 argon ion laser.

The maximum power available from the laser can be attained by removing the prism from the cavity. If suitably reflecting mirrors are then placed at each end of the cavity then all of the lines lase together giving a peak output power of 23 W.

To ensure that only the required excitation wavelength reached the sample, a *Laserspec III* laser filter monochromator [3.4, 3.5] was placed in the path of the beam. This consisted of five prisms and two slits. The prisms dispersed light according to its wavelength and the slits were used to select the required wavelength by blocking the passage of the other, unwanted wavelengths. In practice the filter monochromator had a flat transmission response of 50% between 200 nm and 1000 nm despite being specified at 70%, with a bandpass FWHM of $<0.15$ nm at 633 nm. The filter monochromator was a valuable safeguard against *plasma lines* which are due to light emission from the plasma

inside the laser tube and can interfere with the spectrum under investigation. As a check against plasma lines the prism arrangement to the rear of the laser, containing the back reflector can be removed, thereby preventing lasing action but not the possible presence of a plasma line. The detection of emission at the same wavelength with the prism arrangement removed, as with it in place, therefore proves that the emission originates from a plasma line.

The polarisation experiments were carried out using a half-wave plate to manipulate the polarisation of the laser beam into the orientation required by the experiment. The half-wave plate, in the experimental setup, was placed as near to the sample as possible. The principal plane of the half-wave plate, which took the form of a disc, was the plane passing through both the symmetry axis of the disc and the crystalline optic axis within the disc. If the angle between the half-wave plate principal plane and the electric field vector of the incident beam is $-\theta$, the emergent light will make an angle $+\theta$ with the principal plane [3.6]. The emergent beam has therefore been rotated through an angle $2\theta$ from the incident polarisation. The light was analysed before entering the spectrometer by a dichroic sheet analyser.

#### 3.4.1.2 Spectrometer

The spectrometer used was a *Jobin-Yvon U1000,* one metre long, double pass spectrometer, meaning that it consisted of two, one metre long single pass spectrometers coupled together in subtractive mode [3.7]. By extending the effective length of the spectrometer the stray light rejection of the spectrometer is improved. In the case of the U1000 this is down to $10^{-14}$ at 20 $cm^{-1}$ from the Rayleigh line with the 1800 grooves/mm gratings which are discussed below. This is extremely important in Raman spectroscopy where the region of interest can lie within a few wavenumbers of the intense laser line.

There are two gratings inside the spectrometer which serve to disperse the light. The gratings used were 110 mm square and were ruled holographically with 1800 lines per millimetre. If there are more lines per millimetre, the period of the grating is reduced and hence the dispersion is increased. This can be seen in *Equation 3-1*. The efficiency of the gratings is shown in *Figure 3.3*.

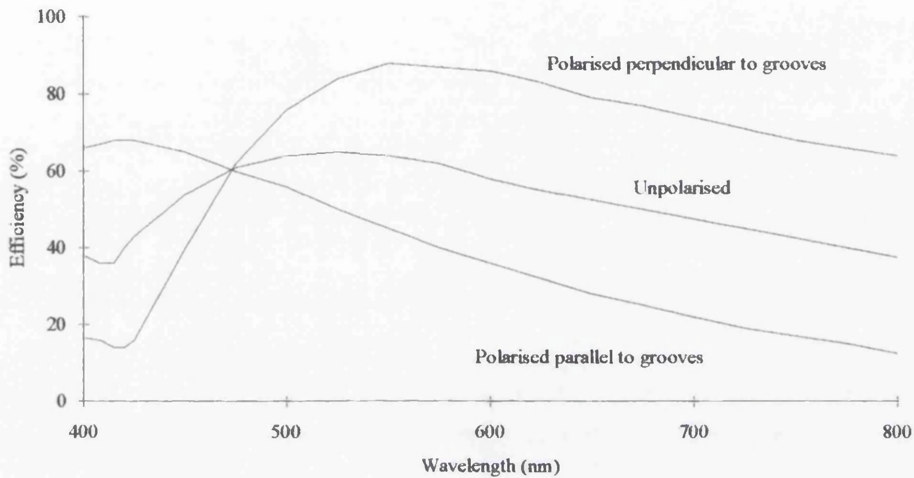


*Figure 3.3* Efficiency of the 1800 grooves/mm gratings as a function of wavelength for various polarisations of light.

The dispersion of the gratings is given by [3.8]:

$$D = \frac{dx}{d\lambda} = f\frac{d\theta}{d\lambda} = \frac{nf}{d\cos\theta} \qquad \textbf{(3-1)}$$

where D ≡ linear dispersion

x ≡ direction of dispersion

λ ≡ wavelength of incident light

f ≡ focal length of exit mirror

θ ≡ angle between the diffracted light and the normal to the grating

n ≡ order of diffraction

d ≡ period of grating

Inside the spectrometer four slits cut out unwanted light in the vertical direction thereby increasing the spectral resolution. Their height is controlled by a micrometer, accurate to 1 μm. There are also shutters accompanying each slit which control the amount of light passing in the horizontal direction, again serving to reject stray light. The shutters are of five discrete widths and only one width per shutter can be chosen. A schematic diagram of the spectrometer showing the elements discussed above and indicating the path the light traverses through the spectrometer is given in *Figure 3.4*.

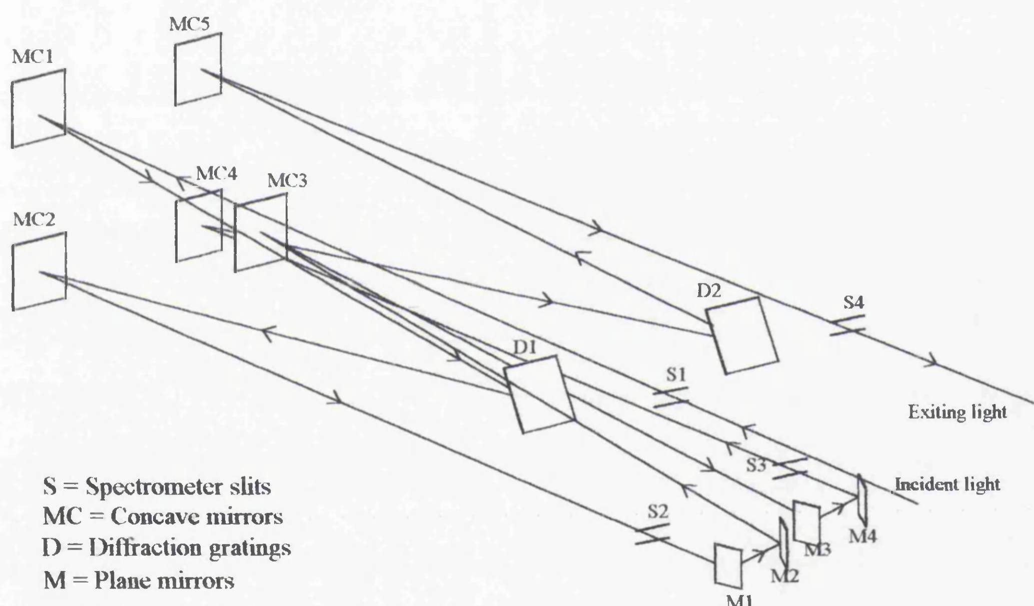


*Figure 3.4* Schematic diagram of the layout of the U1000 spectrometer showing the path the light traverses through it.

The resolution of the spectrometer *R* [3.8] is given by a combination of the static resolution *SR*:

$$SR = \frac{d\lambda}{dx} \cdot S \qquad \textbf{(3-2)}$$

where $SR \equiv$ static resolution (Å)

$\frac{d\lambda}{dx} \equiv$ reciprocal angular dispersion = 2.43 Å/mm

$S \equiv$ slit width (mm)

and the dynamic resolution *DR*:

$$DR = \xi t_c \quad \textbf{(3-3)}$$

where $\xi \equiv$ scan rate

$t_c \equiv$ time constant of detection system

and so:

$$R = SR + DR \quad \textbf{(3-4)}$$

This infers that a compromise must be reached between the resolution and the signal to noise ratio, since the amount of light reaching the detector is determined by the width and height of the slits. The optimum performance is obtained when all of the slits have the same angular width, which in the case of the U1000 is proportional to the measured width.

#### 3.4.1.3 Photomultiplier Tube

The majority of experiments used a *Hamamatsu R943-02 photomultiplier tube* (PMT) as the light detector [3.9]. This consisted of a Cs activated GaAs photocathode that was cooled to a temperature of -23°C to reduce its dark noise to around 10 counts per second typically. The cooling was controlled by the housing which was designed by *Pacific Instruments* and incorporated a Peltier cooler [3.10, 3.11]. This in turn was cooled

by a flow of water and antifreeze kept at 5°C by a *Techne refrigerated bath RG-5*. The PMT was operated at 1.5 kV, supplied by a *Thorn EMI PM 28B* photomultiplier power supply [3.12]. It was possible to operate the PMT in photon counting mode due to the employment of a *Pacific Instruments 3470/AD6* amplifier discriminator and the selection of the PMT dynode chain circuitry. The resulting discriminated pulses were then input on one of the channels of the *Spectralink*, which is described in *Section 3.4.1.6*. Care had to be taken that the internal switches of the Spectralink were set to allow the signal to be input in this form.

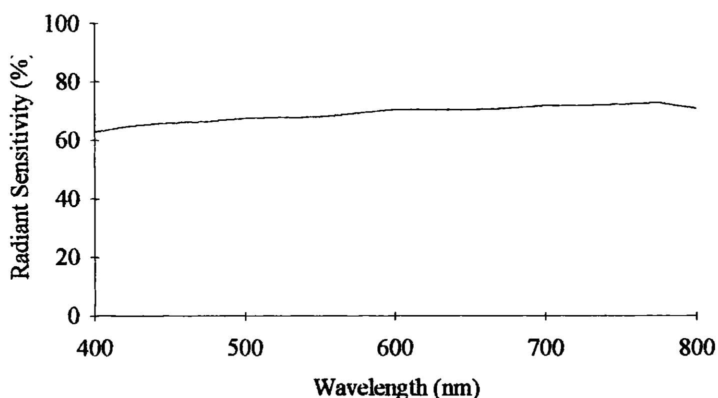


*Figure 3.5* Radiant sensitivity of the Hamamatsu R943-02 photomultiplier tube as a function of wavelength.

The spectral response of the PMT was a function of wavelength and so had to be taken into account when considering the spectral response of the system for spectra that were recorded over a wide range of wavelengths. The response of the PMT as a function of wavelength is given in *Figure 3.5*. It should be noted that the radiant sensitivity is not the same as its quantum efficiency, but it is a measure of its response per unit flux of energy.

#### 3.4.1.4 Spectral Response of the System

In order to compare accurately sub-regions of spectra to one another it is necessary to allow for the spectral response of the system since it may not be constant across the entire energy range being considered. The system referred to is all of the instrumentation, and media in between, after the sample. Hence, in this case the collecting optics, spectrometer mirrors and gratings and the photomultiplier tube must all be included. Let us consider two sub-regions at different extremes of the energy range. If one of the components in the system is more efficient in one of the sub-regions, this would lead to one of the sub-regions being amplified, e.g. higher emission intensities relative to the other. This is flawed and would lead to spurious results. If the spectrum is to be considered as a whole, and it spans a region over which the spectral response is not flat, it should be corrected to allow for the spectral response. Spectra in this thesis either span a short energy range over which the spectral response can be assumed to be flat, or the regions of the spectra are not directly compared but are considered relative to each other.

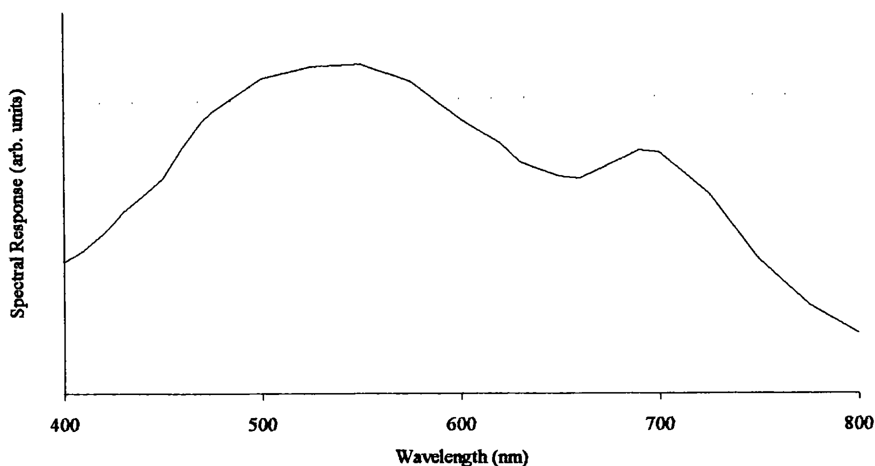


*Figure 3.6* Spectral response of the light detection system as a function of wavelength.

The spectral response was measured [3.13, 3.14] by first heating a piece of graphite to 900°C in a stabilised oven, this then acted as a black-body radiator, the wavelength

dependence of which was known. The emission from the black-body radiator was recorded using the system. This spectrum was then divided by the wavelength dependence of the black-body radiator to obtain the system response shown in *Figure 3.6*.

#### 3.4.1.5 Charge-Coupled Device

A second detector used during this work to increase the speed of data acquisition was an *Astromed CCD 3200 Imaging System*, where CCD stands for charge-coupled device. This was a two-dimensional array of 220 000 pixels that were used to detect light. Due to the high charge transfer efficiency, the resolution of the CCD was limited only by the pixel sampling size. When light was allowed to fall on the CCD by opening the shutter, the light created an electronic charge at each illuminated pixel, the quantity of charge depending on the number of photons incident on the pixel. This resulted in an electronic charge pattern representing the light pattern in the original image.

Light entering the spectrometer was dispersed parallel to one axis of the array, hence detector elements along this axis of the array each measure the light intensity at a different wavelength, thereby allowing many different points in the spectrum to be measured in parallel. This was an important advantage of the CCD over the PMT because it meant the CCD could measure a given range of wavelengths more quickly than the PMT, e.g. minutes instead of hours. This was useful when weak optical signals, as are common in the Raman spectroscopy, had to be investigated and long integration times used to reduce the signal to noise ratio, during which time the system response could have changed due for instance to a fluctuation in the output power of the laser.

Since the CCD measured several wavelengths simultaneously it was necessary to allow a range of wavelengths to reach the detector. The entrance slit of the spectrometer was used solely as a means of controlling the amount of light entering the spectrometer

since all of the dispersion occurred after it, while the final slit was made redundant because a mirror in front of it reflected the light onto the CCD. The two middle slits were opened to 10 mm to allow the required range of wavelengths through. With the 1800 grooves/mm gratings in place the CCD window covered a range of approximately 2 nm (or approximately 120 $cm^{-1}$) at a centre wavelength of 488 nm. If the spectrum required was longer than the range of the window then several frames had to be taken, with the spectrometer moving to the centre of each frame before exposing the CCD, ensuring a slight overlap between frames, the software then stitched these individual frames together.

The CCD could detect photon rates as low as 1 photon/pixel/minute and as high as $10^9$ photons/pixel/minute. This performance was achieved by cooling the CCD to liquid nitrogen temperatures to reduce the dark current and by reading out the CCD slowly to reduce the system noise.

The *detective quantum efficiency* (DQE) of the CCD was improved at lower wavelengths by coating the CCD with *Astrochrome-90*, the peak DQE then reaching almost 50% at 750 nm. The DQE as a function of wavelength is shown in *Figure 3.7*.

An electronic sub-assembly generated the analogue voltages necessary to bias the CCD and to provide the clock waveforms needed to transfer the electronic charge pattern in the correct order to the CCD output. It also processed the output signal to optimise the quality of the output image. The sub-assembly was in turn controlled by a digital controller board installed in the host control computer. The computer was responsible for organising and controlling all aspects of taking data with the system and for managing the data display, storage and analysis.

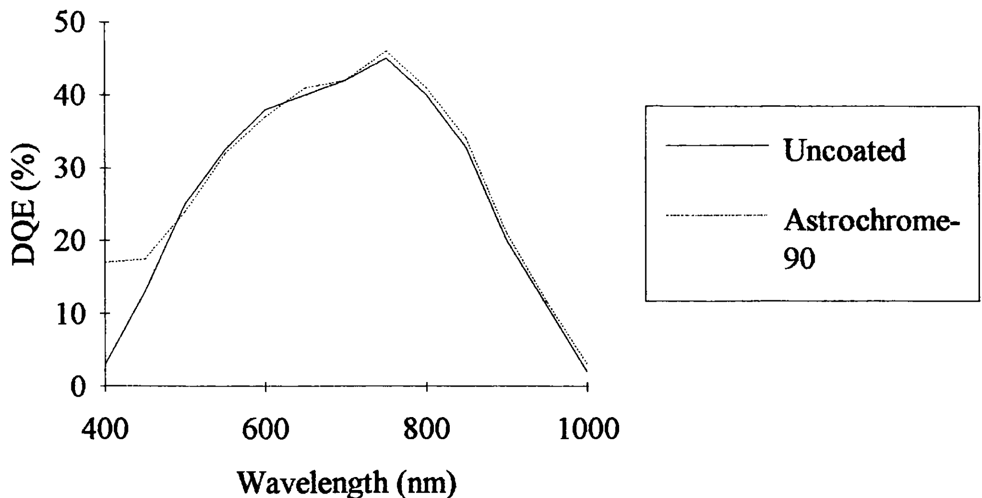


*Figure 3.7* Detective quantum efficiency of the Astromed CCD 3200 Imaging system as a function of wavelength. The figure shows the improvement in the DQE at lower wavelengths caused by the Astrochrome-90 coating.

### 3.4.1.6 Data Acquisition

The software used to control the spectrometer was *Prism* by ISA [3.15]. This was operated from an *Elonex PC386S-200* computer. The instructions from the computer were sent to a *Spectralink* controller [3.16] which then drove a servo which adjusted the orientation of the gratings by altering the angle the grating made with the horizontal. Since the dispersion of the light depends on its wavelength, this had the effect of altering the wavelength of the light incident on the detector that was placed after the final slit. The Spectralink then integrated the voltage signal from the detector over a time period dictated by the operator. This was converted into a photon count and relayed to the software which handled the display of the data. After each point was processed the Spectralink then moved the gratings by an amount dictated by the operator, to a new point which was processed in the same way. In this way the complete spectrum was built up from a series of discrete points, with the software interpolating between the points.

The required parameters of the initial and final wavelength, the integration time for each point and the step size were input using the computer along with relevant scan details for reference purposes.

#### 3.4.1.7 Cryostat

The cryostat used was an *Oxford Instruments CF1204*. The cryostat had a vacuum jacket surrounding the sample chamber, which was there to prevent ambient heat reaching the sample chamber. The windows were made of Quartz to facilitate optical investigations.

Helium gas was passed from a dewar to the cryostat via a transfer tube, the tube was inserted into the dewar with its needle valve open. This precaution meant the helium gas, under an overpressure, created by boil-off when the warmer tube entered the colder dewar, was blown through the tube thereby removing any moisture which could have frozen the needle valve or frosted the windows. The cryostat was first evacuated to remove moisture for the same reasons as mentioned above. This operation was carried out three times as a precaution. The cryostat was then back-filled using He from a gas bottle, to a pressure slightly more than atmospheric pressure. Hence when the transfer tube was inserted into the cryostat, the pressure gradient ensured the gas flow was out of the cryostat, and no moisture from the outside air entered the cryostat.

A vacuum pump was then attached to the transfer tube so that the cryostat was pumped on. The vacuum pump pumped on the outside layer of the transfer tube which meant that He was drawn out of the dewar and along the central layer of the tube into the cryostat. On its return from the cryostat to the pump along the outer sheath the still relatively cold gas helped to prevent the incoming gas warming up. The effect of drawing cold He from the dewar into the cryostat was to cool the contents of the cryostat. The

interior of the cryostat could be cooled to 4.2 K using the helium gas, after this liquid He began to accumulate in the sample chamber. If one continued to pump upon the sample chamber the temperature could be further reduced to around 2K. This was dependent on the pumping speed of the vacuum pump.

The temperature of the sample was controlled by an *Oxford Instruments ITC4,* the ITC standing for *Intelligent Temperature Controller*. This utilised a sensor mounted close to the sample to monitor the temperature of the sample and control electronics applied heat if the temperature dropped below that chosen. The system eventually reached equilibrium between the cooling effect of the incoming helium gas and the warming effect of the heater. The settings used for the controller were as follows; proportional 1.5%, integral 1.5 minutes, derivative 1 minute. As an economic measure, the amount of He allowed into the cryostat was regulated using the needle valve of the transfer tube. With the heater not switched on the temperature was allowed to fall to 90% of the required temperature so that the heater did not have to apply very much energy and so only a small amount of helium was wasted. Using this equipment the temperature of the sample could be controlled to ±0.1 K within the range of 2 K to 300 K.

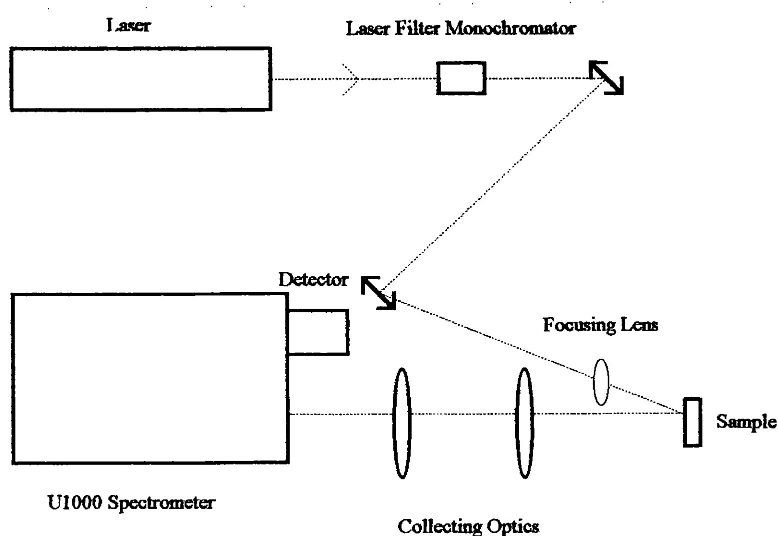


*Figure 3.8* Schematic diagram of the apparatus configured in the near back scattering arrangement.

### 3.4.2 Fabrication Equipment

#### 3.4.2.1 Electron-Beam Writer

The electron beam writer used in this work was a *Leica EBPG5*. It was not capable of producing the resolution of the other beam writers within the department but its great advantage was the area it was possible to cover accurately. This was achieved by dividing the pattern into frames and then *stitching* these frames together. The individual frame size was 0.8 mm square. For this work the dimensions of one frame were adequate to produce a pattern that was visible in the cryostat when using the CCD camera, this is not the same as the Astromed CCD detector but is a simpler *Panasonic model WV CL110 AE* CCD camera. It should be noted this camera was not able to detect the available radiation from the argon-ion laser at wavelengths below 3638 Å and therefore it was not possible to confirm the laser spot was illuminating the required position when wavelengths shorter than 3638 Å were used, hence such lines were not used in this project. The avoidance of any stitching also removed any possibility of inaccuracy in the experimental results due to non-uniformity of the pattern, it also meant the pattern was a lot faster to write which helped to reduce the demand on machine-time.

Fabrication of sub-micron structures places huge demands on standard industrial photolithography which as its name suggests uses light to expose a photoresist, a mask having been made that was similar to the required pattern. The resist is developed and the sample etched to produce the final device. To the credit of those concerned the technology has been developed to an extraordinary degree by increasing the accuracy of the mask fabrication, reducing the wavelength of the light used, thereby increasing the resolution, and by optimising the optics to reduce diffraction effects. This is where the higher resolution capabilities of electron beams become a distinct advantage [2.28, 2.29]. The pattern can be generated using CAD packages and then written directly onto the

sample, the beam position being controlled electronically. Electrons have a much shorter wavelength than the UV light used typically in photolithography, the Leica EBPG5 produced electrons typically at 25 keV and up to a possible maximum of 100 keV. Electrons are also far less susceptible to diffraction than photons. This means that electrons are fundamentally more suitable for writing ultra-small patterns than light. The main drawbacks are the time required to produce a pattern using one scanning beam and the high cost of the equipment, however, both of these factors should be reduced as the technology is developed.

The pattern was generated using several CAD packages, some commercially available and others written in-house. If the pattern was some regular combination of regular shapes the pattern was most easily generated using *Textlib*. The grating was a good example in that it could be thought of as a repetition of a rectangle. Hence *Textlib* was used to first define the dimensions of one rectangle and then to define where and how often the base rectangle should be repeated.

This data was then input into *Cats* which allowed the pattern to be viewed on the workstation terminal and for the resolution to be altered. When choosing the resolution one had to balance the accuracy required and the exposure dose with the time taken to complete writing the pattern. The accuracy was taken to be such that it should take at least two passes of the beam to cover the width of the line being written. The exposure dose had to be found by empirical means. The command *Area* in *Cats* gave the area of the pattern in square microns, dividing this number by the resolution squared gave the number a of square pixels required for the pattern, a pixel being one point of exposure of the beam. One then had to decide on the spot size of the beam. This had to be smaller than the resolution since the beam exposure spread out due mainly to backscattering, yet also large enough to expose all of the resist in the pixel, the beam could be focused to 12 nm ultimately. Another factor to be considered was the resist, more information on this is

given in *Section 3.3*. It should be explained a positive resist was used so that it was the rectangle, representing the plan view of a wire of the grating, that was exposed; rather than the spaces between the wires, which formed a much larger area.

The command *Do* then produced a *.CFLT* file. It was then possible to exit *Cats* and enter the *Writefile* program. This produced a *.IWFL* file which basically contained all of the information required by the beam-writer to produce one pattern. The output file was hence transferred to the beamwriter and stored in a directory called *Patterns*.

The beamwriter also required information on how often to repeat the pattern, where to position the duplicate patterns and what exposure to use. These commands were given by entering the *BWL* package. This package produced a *.COM* file which was transferred via an intermediate workstation to the beamwriter and stored in a directory called *Jobs*.

#### 3.4.2.2 Reactive Ion Etcher

The technique of dry-etching has been developed to great effect within the department to produce devices of nanometer dimensions in Si and GaAs. The technology has now been transferred to II-VI semiconductors and this work is the first to assess the technological steps for II-VI semiconductor nanostructures.

In *reactive ion etching* (RIE) [2.20, 2.28, 2.29], a mixture of gases enter the reaction chamber were they are subjected to a rf field of 13.6 MHz. This has the effect of creating a plasma by removing the lighter, more mobile electrons from the gas, leaving behind the heavier, less mobile positive ions. The sample was placed on an electrode and a DC bias in the range of 300-1000 V applied so that the positive ions were attracted towards the electrode on which the sample was placed. The ions were accelerated by the voltage

across the dark space of the glow discharge and arrived with energies of the order of a few hundred electron volts, this explains why there is a physical bombardment associated with reactive ion etching. The energy of the ions in this technique is orders of magnitude less than the energy of the ions used in a true ion bombardment experiment, e.g. Holtz et al. [3.17] quotes 45 keV for the energy of the ions used in his bombardment experiment, hence the crystalline damage caused by RIE is expected to be much less than that caused by ion bombardment. A schematic diagram of the apparatus is given in *Figure 3.9*. By careful choice of the initial gases these ions are chemically reactive in such a way that they form volatile compounds which can be removed from the sample and chamber as exhaust gases.

The reactive ion etch system used for this project was an *Electrotech SRS Plasmafab 340* with an anode to cathode area ratio of 3:1. The electrodes were made of aluminium, the cathode being coated with titanium oxide.

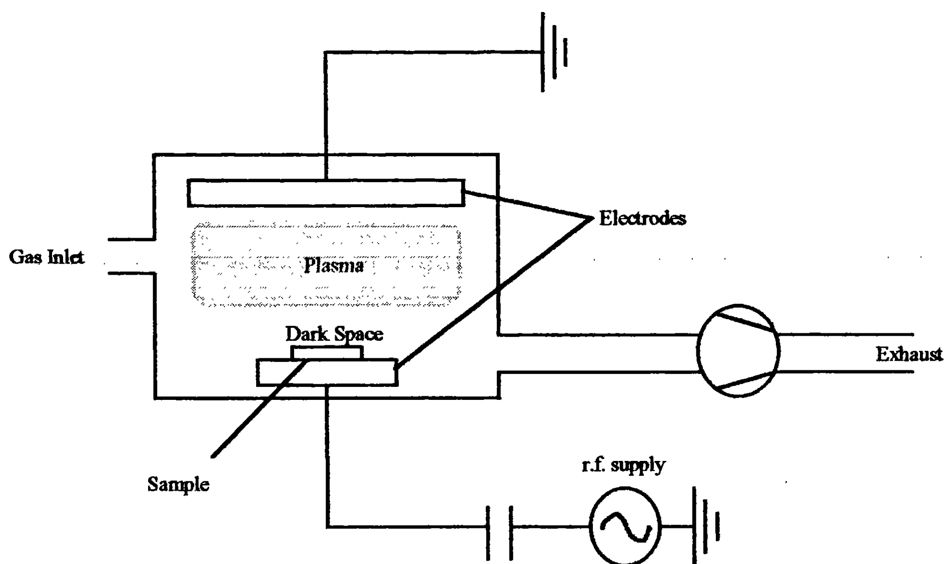


*Figure 3.9* Schematic diagram of the reactive ion etch system.

For II-VI semiconductors the etch gas used was methane hydrogen ($CH_4/H_2$) in contrast to the only other work done on these materials in which $BCl_3$ was used without achieving the necessary results for etching microstructures where one must obtain vertical

sidewalls and horizontal floors. The ability to achieve this is an enormous advantage the technique has over wet etching where surfaces nearly always have some degree of curvature due to the isotropy of the etch. The etch rate was found to vary as a function of the percentage of methane in the etch gas. Several etch tests were carried out by Foad et al. [3.18] to ascertain the etch rate of ZnTe and the results of these experiments are illustrated in *Figure 3.10*. When optimised the $CH_4/H_2$ gas mixture gave an anisotropic uniform etch, which was a necessary condition for fabricating microstructures.

To quantify the anisotropy of an etch process Sze [3.19] defined the *anisotropy factor*, AF, to be:

$$AF = 1 - \left( \frac{\text{Horizontal etch rate}}{\text{Vertical etch rate}} \right) \quad \textbf{(3-5)}$$

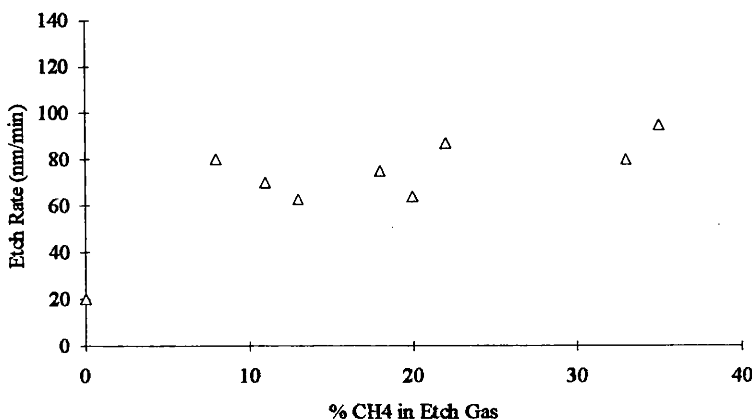


*Figure 3.10* Graph showing the etch rate of ZnTe as a function of the percentage of methane in the methane hydrogen etch gas. The pressure was 20 mTorr, RF power was 150 W and the DC bias was approximately 850 V.

## 3.5 Experimental Techniques

In this section we deal with the theoretical aspects behind this project. It should be noted the techniques dealt with here are non-destructive optical tests. It is hoped the findings here may be used in the future to further develop the techniques to become production worthy, the non-destructive nature would then be a major advantage since the sample would not have to sacrificed and it follows this would allow the individual testing of every sample and not just a few representative ones. It is necessary to carry out optical and electrical tests on nanostructures because it is possible for a nanostructure to appear perfect when examined under the electron microscope yet for it still to be electrically or optically dead.

### 3.5.1 Photoluminescence

This non-destructive technique relies upon the promotion of electrons from the valence band into the conduction band by incident photons of energy $h\nu_i$. For this to happen the incident light must have an energy greater than that of the energy gap, $E_g$, i.e. $h\nu_i > E_g$. Once in the conduction band the electrons lose energy and drop through the continuum of available states, giving up energy by inelastic scattering processes, mainly involving phonons, until they reach the lowest energy state available in the conduction band. From this state the electron then loses more energy as it falls back to the valence band from where it originated. This can occur in two ways, either non-radiatively where the electrons drop through any available states giving up energy by scattering processes, involving mainly phonons, or radiatively where a photon of energy $h\nu_f$ is expelled. We therefore tune the laser to emit photons with energy greater than that of the bandgap.

If the material being examined is sufficiently pure the electrons and holes generated are able to pair off, they are held together by the coulombic attraction between their

opposite charges. This system is then known as a *free exciton*. The term free is used since the exciton is not a set of spatially localised states but instead is free to traverse the crystal lattice. It is now customary to use the conduction band edge to define the continuum state of the exciton and to represent the various states of the exciton to lower energies, see *Figure 3.11*. The ionisation energy of the free exciton, $E_X$, by analogy with the hydrogen atom is given by Pankove [3.20]:

$$E_x = \frac{-m_r^* e^4}{2h^2\varepsilon^2}\frac{1}{n^2} \tag{3-6}$$

where $e \equiv$ elementary charge

$h \equiv$ Planck's constant

$\varepsilon \equiv$ relative permittivity

$n \equiv$ integer $\geq 1$ indicating the various excitonic states

The reduced mass, $m_r^*$, is defined as:

$$\frac{1}{m_r^*} = \frac{1}{m_e^*} + \frac{1}{m_h^*} \tag{3-7}$$

where $m_e^* \equiv$ effective mass of the electron

$m_h^* \equiv$ effective mass of the hole

When the electron and hole recombine they emit a photon of energy $h\nu$ where:

$$h\nu = E_g - E_x \tag{3-8}$$

Since the free exciton is mobile and consists of two elements which are themselves mobile, the translational velocity of the elements must be identical even though their

instantaneous velocities may be different. This places a constraint upon where the exciton can exist in *E-k* space:

$$\left[\frac{dE}{dk}\right]_{hole} = \left[\frac{dE}{dk}\right]_{electron} \tag{3-9}$$

The analogy with the hydrogen-like atom is strictly no longer valid since the effective mass of the hole, though much larger than the effective mass of the electron is not comparable to the mass of a proton. Therefore the exciton is said to have a centre of mass when describing its motion in the crystal.

It should be noted that if strain is present in the crystal lattice this leads to a splitting of the free exciton peak into two, caused by the difference in effective mass of heavy and light holes leading to a relative shift in the valance bands, hence reference is made to heavy and light hole free excitons.

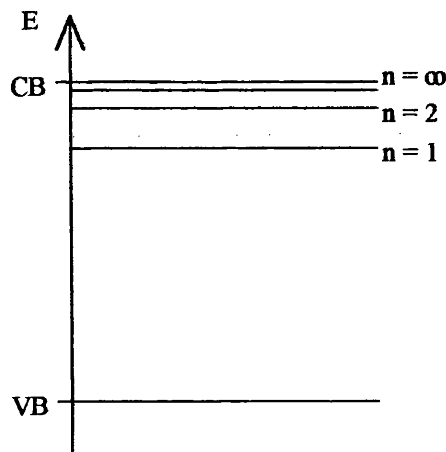


*Figure 3.11* Energy level diagram for the exciton and its excited states. The exciton energy is referenced to the conduction band edge.

Should impurities be present in the lattice they may lead to the formation of *bound excitons*. This happens when a free hole passes close to a neutral donor. The neutral

donor has its extra electron orbiting around the donor as expected. However, the free hole interprets the separation of the electron and the donor atom as a dipole and proceeds to travel around the donor in the electrostatic field of the dipole, see *Figure 3.12*. In *Figure 3.12* $E_b$ represents the energy binding the exciton to the donor. A similar argument holds for a free electron being bound to a neutral acceptor. This phenomenon was first observed in Si by Haynes [3.21].

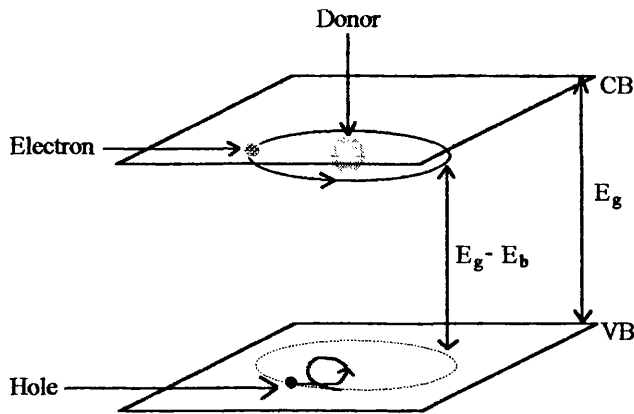


*Figure 3.12* Schematic diagram showing an exciton bound to a donor atom.

Another important phenomenon occurs when a neutral donor and a neutral acceptor are near each other. The electron of the donor atom becomes increasingly more shared by the acceptor as the distance between them decreases i.e. the donor and acceptor form a pair. The energy of such donor and acceptor pairs, $E_{DAP}$, is given by Pankove [3.20] as:

$$E_{DAP} = E_g - E_A - E_D + \frac{e^2}{\varepsilon r} \tag{3-10}$$

where $E_D \equiv$ ionisation energy of the donor impurity

$E_A \equiv$ ionisation energy of the acceptor impurity

$r \equiv$ separation of the donor and acceptor

Since the above equation contains the separation of the donor and the acceptor, r, as a parameter, it is possible for fine structure to be discernible in the emission from donor-acceptor pairs, this is due to the finite variation in the positions of the donors and acceptors in the lattice. If the donor and acceptor both occupy Te sites in ZnTe, they are referred to as a type-I donor-acceptor pair. If the donor was to occupy a Te site and the acceptor to occupy a Zn site they would then be referred to as a type-II donor-acceptor pair.

In some cases a photoluminescence peak is accompanied by peaks to lower energies. These lower energy peaks have lineshapes similar to the main peak and are separated by equal energy amounts each of which is equivalent to the energy of a longitudinal optic phonon in the material, hence the lower energy peaks are called *phonon replicas*. They occur when a phonon is emitted at the same time as the luminescence emission occurs, the energy to create the phonon comes from the emitted photon and so its energy is reduced by an amount equal to the energy of the phonon. It is possible for more than one phonon to be emitted providing the principle of energy conservation is not violated. The phenomenon of phonon replication occurs at the cost of a lower transition probability per phonon emitted and the more phonons emitted, i.e. the lower the emission energy, the weaker the emission becomes.

### 3.5.2 Raman Scattering

#### 3.5.2.1 Raman Scattering from Phonons

The Raman effect was named after C.V. Raman who was the first person to observe the phenomenon in 1928 [3.22] after Smekal [3.23] had predicted it in 1923. It is a non-linear effect in that it results in frequencies that were not present in the incident radiation. This occurs due to the light impinging onto the subject material and a small

fraction of that light, less than $10^{-7}$ of the incident light, being scattered by interactions that can either create or destroy quantised lattice vibrations in the material. These vibrations are called phonons. The scattered light is shifted by an amount equal to the vibrational frequencies of the system, hence there is no violation of energy conservation. This implies the shift is independent of the wavelength of light used.

The scattering occurs because the electric field of the incident photons couples to the internal fields of the molecules. The effect can be explained to a certain extent classically but a full treatment requires a quantum mechanical argument. The classical argument is outlined first.

To briefly describe the classical argument let us first define an *electric field* $\mathbf{E}_I$:

$$\mathbf{E}_I = \boldsymbol{\varepsilon}_I E_I \quad \textbf{(3-11)}$$

where $\boldsymbol{\varepsilon}_I \equiv$ unit vector representing the polarisation of the incoming light.

The dipole moment induced in an atom or molecule placed in the incident electric field may be written [3.24, 3.25]:

$$\mathbf{M} = \mathbf{a} \cdot \boldsymbol{\varepsilon}_I E_I \quad \textbf{(3-12)}$$

where $\mathbf{a} \equiv$ polarisability tensor.

The radiation energy emitted per unit time by the electric dipole moment, **M**, vibrating at a frequency, $\omega_X$, may be written:

$$\frac{dW_s}{d\Omega} = \frac{\omega_x^4}{16\pi^2 \varepsilon_0 c^3} \left| \boldsymbol{\varepsilon}_s \cdot \mathbf{M} \right|^2 \quad \textbf{(3-13)}$$

The classical theory assumes that a is produced by an electronic charge, e, attached to atomic cores by a restoring force $k = \omega_0^2 m$, where m is the electron mass and $\omega_0$ is the vibrating frequency of the harmonic oscillator so defined. Solving the appropriate equation of motion, with $\gamma$ as the damping constant, leads to:

$$a = \frac{e^2}{m\left(\omega_0^2 - \omega_x^2 - i\omega_x\gamma\right)} \tag{3-14}$$

The classical theory next considers a vibrational mode of the molecule of frequency $\omega$. The mode can be characterised by displacements of the N atoms with time dependences $e^{\pm i\omega t}$ and amplitudes $u_i$ ($i = 1,2...N$), where $u_i$ are related to the normal mode coordinate, $\xi$. Assuming the frequency of the exciting laser light to be away from any resonance effects we can treat the phonon as a static deformation of the molecule and define at each instant of time a polarisability which depends on the normal mode coordinate $\xi$. It is then possible to expand the polarisability in terms of $\xi$ to obtain [3.26]:

$$\begin{aligned} a(\omega_1, \xi) = a(\omega_1) &+ \frac{\partial a}{\partial \xi}\xi e^{-i\omega t} + \frac{\partial a}{\partial \xi}\xi^* e^{i\omega t} \\ &+ \frac{1}{2}\frac{\partial^2 a}{\partial \xi^2}\xi^2 e^{-2i\omega t} + \frac{1}{2}\frac{\partial^2 a}{\partial \xi^2}\xi^{*2} e^{2i\omega t} \\ &+ \frac{1}{2}\frac{\partial^2 a}{\partial \xi \partial \xi^*}\left(\xi\xi^* + \xi^*\xi\right) + \ldots \end{aligned} \tag{3-15}$$

This equation can be substituted into *Equation (3-12)* to obtain scattered radiation at $\omega_l$, describing the Rayleigh scattered light, note that its frequency remains unchanged. However, there now also appears scattered radiation at the Anti-Stokes frequency $\omega_l+\omega$ and at the Stokes frequency $\omega_l-\omega$.

The quantum mechanical derivation of optic phonon Raman scattering was more rigorously derived using third order perturbation theory by Born and Bradburn [3.27] in 1947 and subsequently by Smith [3.28] in 1948. For quantitative purposes it is convenient to use the Raman scattering efficiency, $dS/d\Omega$, as a measure of the scattered intensities. The term $dS/d\Omega$ describes the ratio between the scattered and incident powers for a unit solid angle and a unit path length within the crystal, hence it has dimensions of inverse length. The scattering efficiency per unit length can be written as [3.29]:

$$\frac{dS}{d\Omega}=\frac{\omega_s^3\omega_l}{c^4}\frac{\hbar}{2V_cM^*\omega_0}\frac{n_s}{n_l}\left[N(\omega_0)+1\right]\sum_i\left|\varepsilon_s\cdot\vec{R}_i\cdot\varepsilon_l\right|^2 \qquad \textbf{(3-16)}$$

where $V_c \equiv$ volume of primitive cell

$M^* \equiv$ reduced mass of the atoms contributing to the optical mode

$N(\omega_0) \equiv$ Bose-Einstein factor of the phonon

$n \equiv$ refractive index

$\omega \equiv$ frequency of the light

$\varepsilon \equiv$ polarisation vector of the light

The indices $l$ and $s$ refer to the laser and scattered light respectively. $\vec{R}_i$ is the Raman tensor for zone centre phonons. For backscattering at the (001) face, the allowed LO-phonon Raman scattering tensor for a zinc-blende material via the deformation potential interaction is given by [3.26, 3.30]:

$$\vec{R}_{DP}=\begin{pmatrix}0 & a_{DP} & 0\\ a_{DP} & 0 & 0\\ 0 & 0 & 0\end{pmatrix} \qquad \textbf{(3-17)}$$

Under similar conditions the tensor for the Fröhlich interaction is given by [3.26, 3.30]:

$$\vec{R}_F = \begin{pmatrix} a_F & 0 & 0 \\ 0 & a_F & 0 \\ 0 & 0 & a_F \end{pmatrix} \quad \textbf{(3-18)}$$

The Raman polarisability, a, corresponding to a scattering process by which a phonon changes from its initial state *i* to a final state *f*, is given by Ganguly and Birman [3.31] as:

$$a = \frac{n_l n_s}{2\pi} \frac{V_c}{\bar{u}_0} \frac{1}{\hbar\omega_l} W_{fi} \quad \textbf{(3-19)}$$

where the relative displacement, $\bar{u}_0$, is defined as:

$$\bar{u}_0 = \left( \frac{\hbar V_c}{2VM^* \omega_0} \right)^{\frac{1}{2}} \quad \textbf{(3-20)}$$

where $V \equiv$ volume of crystal.

$W_{fi}$ is the amplitude probability of a photon being scattered accompanied by the emission of an optical phonon. Assuming excitons to be the virtual intermediate states the matrix element $W_{fi}$ can be written as [3.29]:

$$W_{fi} = \sum_{pq} \left( \frac{\langle f|H_{ER}|q\rangle\langle q|H_{EL}|p\rangle\langle p|H_{ER}|i\rangle}{(\hbar\omega_l - E_p + i\Gamma_p)(\hbar\omega_s - E_q + i\Gamma_q)} + \frac{\langle f|H_{ER}|p\rangle\langle p|H_{EL}|q\rangle\langle q|H_{ER}|i\rangle}{(\hbar\omega_l + E_q + i\Gamma_q)(\hbar\omega_s + E_p + i\Gamma_p)} \right) \quad \textbf{(3-21)}$$

where $E \equiv$ energy of the exciton

$\Gamma \equiv$ lifetime broadening of the exciton

$p,q \equiv$ reference to excitonic intermediate states

$H_{ER} \equiv$ exciton-radiation interaction Hamiltonian

$H_{EL} \equiv$ exciton-lattice interaction Hamiltonian

This rather complicated expression can be summarised to a certain extent [3.24] by the diagram in *Figure 3.13*.

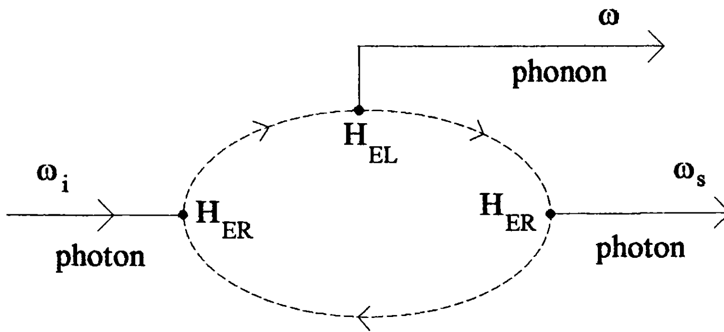


*Figure 3.13* Illustration of a Raman scattering process where incident radiation interacts with an electron. This electron also interacts with the lattice causing the emission of a phonon and there is another interaction resulting in the emission of a photon.

The lifetime broadening $\Gamma_p(n)$ was derived empirically by Cantarero et al. [3.29] to be:

$$\Gamma_p(n) = \Gamma_p(k) - \left( \frac{\Gamma_p(k) - \Gamma_p(1)}{n^2} \right) \tag{3-22}$$

where $n \equiv 1,2,3\ldots$

$\Gamma_p(1) \equiv$ broadening of the n=1 discrete excitonic state

$\Gamma_p(k) \equiv$ broadening of the continuous excitonic states

The Hamiltonians can be written as [3.29]:

$$H_{ER} = \sum_{\substack{Kp \\ e\kappa \\ cv}} \left\{ T_{cv}^{p}(\mathbf{K}) D_{pK}^{\xi}\left(a_{\kappa,e} + a_{-\kappa,e}^{\xi}\right) + \left[T_{cv}^{p}(\mathbf{K})\right]^{*} D_{pK}\left(a_{\kappa,e} + a_{-\kappa,e}^{\xi}\right) \right\} \quad \mathbf{(3\text{-}23)}$$

$$H_{EL} = \sum_{\substack{KK' \\ Q\nu \\ pq}} S_{qp}^{KK'}(\mathbf{Q}) D_{qK'}^{\xi} D_{pK}\left(b_{Q,\nu}^{\xi} + b_{-Q,\nu}\right) \quad \mathbf{(3\text{-}24)}$$

where $\kappa \equiv$ wavevector of light

$\nu \equiv$ phonon branch

$\mathbf{Q} \equiv$ quasi-momentum of the phonon

$\mathbf{K} \equiv$ centre-of-mass momentum of the exciton

$D \equiv$ annihilation operator for excitons

$a \equiv$ annihilation operator for photons

$b \equiv$ annihilation operator for phonons

$\xi \equiv$ creation version of the above operators

The exciton-photon coupling constants T, are given by Elliot [3.32] as:

$$T_{cv}^{p}(\mathbf{K}) = -\frac{e}{m}\left(\frac{2\pi\hbar}{\omega_{l(s)} n_{l(s)}^{2}}\right)^{\frac{1}{2}} e_{l(s)} \langle c|\mathbf{p}|v\rangle \Psi_{p}(0) \delta_{K,\kappa} \quad \mathbf{(3\text{-}25)}$$

where $\langle c|\mathbf{p}|v\rangle \equiv$ matrix element of the momentum operator

$\Psi_{p}(\mathbf{r}) \equiv$ wavefunction of the internal exciton state

The exciton-phonon coupling constant S, can take two forms according to the type of interaction occurring. The interaction may be either a deformation potential or a

Fröhlich one. For the case of the deformation potential the interaction is described by Martin [3.33] as:

$$S_{qp}^{K'K}(\mathbf{Q})=\frac{\sqrt{3}\bar{u}_0}{2a_0}\left[D_e^v(\mathbf{r})I_{qp}^h(\mathbf{Q})-D_h^v(\mathbf{r})I_{qp}^e(-\mathbf{Q})\right]\delta_{K',K+Q} \qquad \textbf{(3-26)}$$

where $D \equiv$ deformation potential as defined by Pikus and Bir [3.34]

$a_0 \equiv$ lattice constant

$e \equiv$ refers to electron

$h \equiv$ refers to hole

The matrix element I, is shown by Canterero et al. [3.29] to be:

$$I_{qp}^{e(h)}(\mathbf{Q})=\int d^3r\Psi_q^*(\mathbf{r})\exp\left(-i\frac{m_{e(h)}}{m_e+m_h}\mathbf{Q}\cdot\mathbf{r}\right)\Psi_p(\mathbf{r}) \qquad \textbf{(3-27)}$$

This leads to the derivation of the contribution to the polarisability by the deformation potential [3.29]:

$$a_{DP}=\frac{a_0^2}{2m}\frac{R_H^2a_H^3\sqrt{3}}{\hbar\omega_l(\hbar\omega_l\hbar\omega_s)^{\frac{1}{2}}}\left\{\begin{array}{l}\langle c\,|\mathbf{p}\cdot\mathbf{e}_s|v_q\rangle\langle v_q|D_h^v|v_p\rangle\langle v_p|\mathbf{p}\cdot\mathbf{e}_l|c\,\rangle\dfrac{\Psi_q^*(0)I_{qp}\Psi_p(0)}{(\hbar\omega_l-E_p+i\Gamma_p)(\hbar\omega_s-E_q+i\Gamma_q)}\\+\langle c\,|\mathbf{p}\cdot\mathbf{e}_s|v_p\rangle\langle v_p|D_h^v|v_q\rangle\langle v_q|\mathbf{p}\cdot\mathbf{e}_l|c\,\rangle\dfrac{\Psi_p^*(0)I_{pq}\Psi_q(0)}{(\hbar\omega_l+E_q+i\Gamma_q)(\hbar\omega_s+E_p+i\Gamma_p)}\end{array}\right\}$$

**(3-28)**

where $R_H \equiv$ Rydberg of the hydrogen atom

$a_H \equiv$ Bohr radius of the hydrogen atom.

If we now consider the Fröhlich interaction the above arguments hold but the exciton-phonon coupling constant is different. According to Fröhlich [3.35] it is given by:

$$S_{qp}^{KK'}(Q)=\frac{1}{\sqrt{V}}\frac{C_F^*}{|Q|}\left[I_{qp}(-Q_h)-I_{qp}(Q_e)\right]\delta_{K',K-Q} \qquad \textbf{(3-29)}$$

Here we define [3.36]:

$$C_F=-i\left(\frac{1}{\varepsilon_\infty}-\frac{1}{\varepsilon_0}\right)^{\frac{1}{2}}\left(2\pi\hbar\omega_0 e^2\right)^{\frac{1}{2}} \qquad \textbf{(3-30)}$$

where $\varepsilon_0 \equiv$ static dielectric constant

$\varepsilon_\infty \equiv$ optical dielectric constant

This leads to the derivation of the contribution to the polarisability by the Fröhlich interaction:

$$a_F=\left(\frac{e}{m}\right)^2\frac{V_c C_F^*\langle c|e_l\cdot p|v\rangle\langle v|e_s\cdot p|c\rangle}{\bar{u}_0\omega_l(\omega_l\omega_s)^{\frac{1}{2}}Q}\sum_{pq}\Psi_q^*(0)\frac{\left[I_{qp}(-Q_h)-I_{qp}(Q_e)\right]}{(\hbar\omega_s-E_q+i\Gamma_q)(\hbar\omega_l-E_p+i\Gamma_p)}\Psi_p(0)$$

**(3-31)**

### 3.5.2.2 Resonant Raman Scattering

The phenomenon of resonance [3.37] that is utilised in parts of this project can be explained easily if one pays close attention to the equations which define the polarisibilities for the case of the deformation potential and the Fröhlich interactions.

If we simplify matters by ignoring the effects of broadening then close examination of *Equation 3-28* and *Equation 3-31* show that the polarisability, in both cases, tends towards a maximum when either:

$$\hbar\omega_l \rightarrow E_p \qquad \text{or} \qquad \hbar\omega_s \rightarrow E_q \qquad \textbf{(3-32)}$$

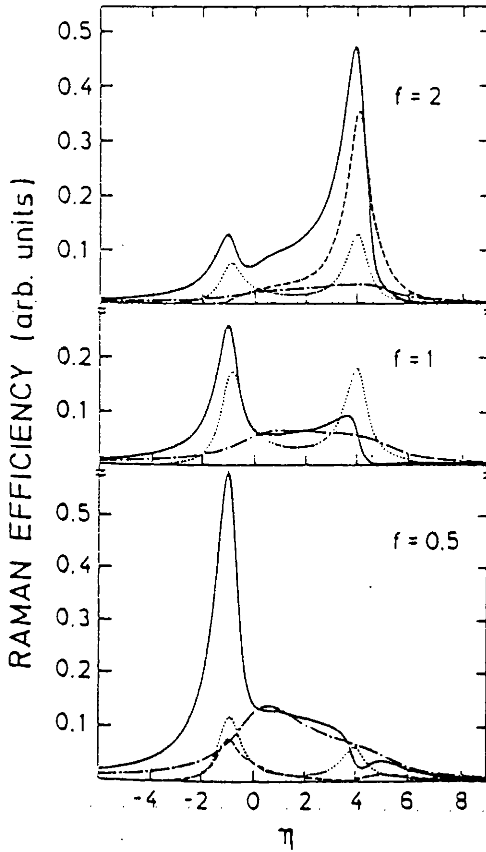


*Figure 3.14* Raman polarisability $|a_{DP}|^2$ (solid lines) as a function of the parameter η where $\eta = \frac{(\hbar\omega_l - E_g)}{R}$ and R≡exciton Rydberg energy, for three different values of f, 0.5, 1 and 2. Also the different contributions from the matrix elements, discrete-discrete (short dashed line), discrete-continuous plus continuous-discrete (long dashed line), and continuous-continuous (dot-dashed line). Here f is defined to be the ratio of Bohr radii of final and initial states i.e. $f_{qp} = \frac{a_q}{a_p}$ [3.29].

This then leads to an increase in the terms that make up the Raman tensor. This in turn leads to a dramatic increase in the scattering efficiency due to the squaring of the term involving the Raman tensor, as is shown in *Equation 3-16*. Cantarero et al. [3.29, 3.36] plotted the Raman scattering efficiency as a function of photon energy, these are reproduced in *Figure 3.14* and *Figure 3.15*.

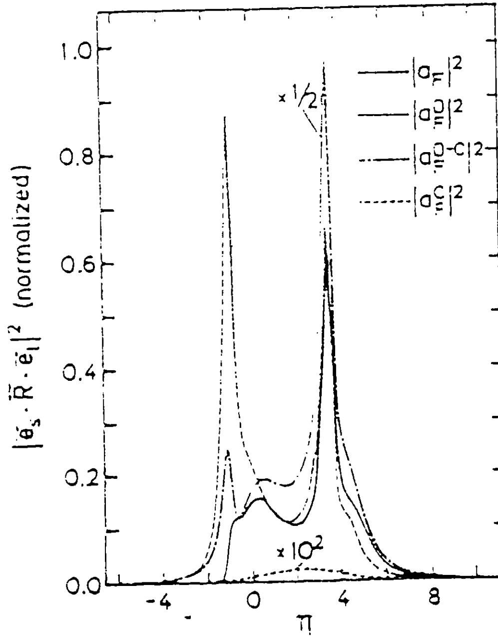

*Figure 3.15* Raman polarisability $|a_F|^2$ as a function of the parameter $\eta$, for $\frac{\hbar\omega_0}{R} = 4.55$. Also the different contributions discrete-discrete, discrete-continuous plus continuous-discrete, and continuous-continuous matrix elements denoted by superscripts *D*, *D-C*, and *C* respectively [3.36].

This means qualitatively that the intensity of the scattered signal can be increased simply by choosing the excitation frequency to be near that of an excitonic state. Such states can be found near the band-gap of the material.

### 3.5.2.3 Polarisation

The Raman scattering efficiency of the system to polarised light is easily calculated

using the Raman tensors of *Equation 3-17* and *Equation 3-18*. It is only necessary to know the crystal plane being investigated, which determines the Raman tensor, the polarisation of the light entering and that leaving the crystal. If these are all known it is a simple case of completing the multiplication.

Consider light incident on the (001) face of a zinc-blende crystal. Let the incident light be polarised parallel to the $x$-axis and the analyser be set in the same orientation i.e.

$$\boldsymbol{\varepsilon}_l = \boldsymbol{\varepsilon}_s = \begin{pmatrix} 1 & 0 & 0 \end{pmatrix} \tag{3-33}$$

We are able to use *Equation 3-16* to define the Raman scattering efficiency as:

$$\frac{dS}{d\Omega} \propto \left| \boldsymbol{\varepsilon}_s \cdot \vec{\mathbf{R}}_i \cdot \boldsymbol{\varepsilon}_l \right|^2 \tag{3-34}$$

Substituting into *Equation 3-17* and *Equation 3-18* we have to evaluate the following equations:

$$\begin{aligned} \frac{dS}{d\Omega} &\propto \left| \begin{pmatrix} 1 & 0 & 0 \end{pmatrix} \begin{pmatrix} a_F & 0 & 0 \\ 0 & a_F & 0 \\ 0 & 0 & a_F \end{pmatrix} \begin{pmatrix} 1 \\ 0 \\ 0 \end{pmatrix} \right|^2 \\ &\propto \left| a_F \right|^2 \end{aligned} \tag{3-35}$$

and:

$$\begin{aligned} \frac{dS}{d\Omega} &\propto \left| \begin{pmatrix} 1 & 0 & 0 \end{pmatrix} \begin{pmatrix} 0 & a_{DP} & 0 \\ a_{DP} & 0 & 0 \\ 0 & 0 & 0 \end{pmatrix} \begin{pmatrix} 1 \\ 0 \\ 0 \end{pmatrix} \right|^2 \\ &\propto \left| 0 \right|^2 \end{aligned} \tag{3-36}$$

Therefore the final Raman scattering efficiency is:

$$\frac{dS}{d\Omega} \propto |a_F|^2 \tag{3-37}$$

We see there is no contribution to the Raman scattering efficiency from the deformation potential, this is obviously not always the case and is dependent on the polarisations and crystal face used. If it should occur that both of the contributions cancel we are in a symmetry forbidden regime.

#### 3.5.2.4 Raman Scattering from Tellurium

Amorphous Te crystallises at 283 K [3.38] and so it is unstable at room temperature. The only stable form of crystalline Te is a trigonal structure with space group $D_3^4$. The lattice consists of helical chains located at the corners and centres of a hexagonal array. There are three atoms per turn of each helix and these define the unit cell. The helical axis defines the *c*-axis of the crystal. Each atom is separated from its nearest neighbour in the chain by 2.86 Å, which is a considerably shorter distance than its nearest neighbours in adjacent chains, a distance of 3.46 Å, and so the binding between atoms in one of the chains is much stronger than the binding between the chains [3.39]. It is because of this inequality in the bond strengths that the normal modes of the $D_3$ point group for a three atom molecule can be modelled by long wavelength lattice modes [3.39]. Group theory can then be used to predict two doubly degenerate E type modes which are infra-red and Raman active and one $A_1$ type mode which is Raman active. If the degeneracy of the E type modes is lifted there is then a total of five Raman active modes. There is also one $A_2$ type mode which is infra-red active.

The frequencies of these modes are summarised in *Table 3.2* below together with values obtained for the mode frequencies using other techniques for comparison [3.39].

The other techniques quoted are neutron scattering and infra-red, which was obtained indirectly from a reflectivity experiment.

| | **Frequency ($cm^{-1}$)** | | |
|---|---|---|---|
| **Symmetry** | **Raman** | **Neutron** | **Infra-red** |
| $E^l$ (transverse) | 91.3 | 93.0 | 92.0 |
| $E^l$ (longitudinal) | 102.2 | | 106.0 |
| $A_1$ | 119.7 | 119.0 | |
| $E^u$ (transverse) | 139.5 | 138.0 | 144.0 |
| $E^u$ (longitudinal) | 139.5 | | |

*Table 3.2* The Raman active phonon modes observed for tellurium and their frequencies as measured using various experimental techniques. Here the superscripts *l* and *u* refer to lower and upper respectively.

### 3.5.2.5 Effect of Crystalline Damage on the Raman Spectrum

Raman scattering has been postulated as a tool to investigate and quantify the amount of crystalline damage induced in semiconductors by fabrication techniques such as dry etching and ion implantation. The main advantage of the technique is that it is non-destructive which makes it possible to measure the amount of damage in each and every production wafer should it be required, rather than using a destructive test on one, representative wafer. The latter practice allows the introduction of errors if the chosen sample is not representative or if the process is not reproducible, it also results in the physical and financial loss of the representative wafer.

There have been several reports of the damage induced in GaAs by ion implantation being assessed by Raman scattering [3.17, 3.40]. In these reports the LO and

TO phonons are visible in the unimplanted samples. The phonon peaks are sharp and occur at the frequencies predicted by the phonon dispersion curves for GaAs at k=0. Samples exposed to different fluxes of 45 keV Beryllium ions were examined by Raman scattering after each exposure. The resulting series of spectra showed the progression of the material from the crystalline state to an almost amorphous state as the flux of ions was increased. The peak intensity of the phonon peaks was reduced and the peaks exhibited asymmetric broadening to lower energies. Lower energy modes also appeared in the spectrum as the dispersion relations degenerated, indicative of a lack of crystallinity.

Wagner and Hoffman [3.41] reported the ratio of the 2LO phonon peak intensity to that of the LO phonon as a possible means of assessing and quantifying the damage induced by argon ions in GaAs. The 2LO phonon intensity was found to be relatively more susceptible to damage than that of the LO phonon, i.e. its intensity decreased faster than the intensity of the LO phonon. This was due to the $E_1$ gap resonance for scattering by the 2LO phonon being ~0.2 eV full width at half-maximum which is sharper than that for scattering by the LO phonon. The scattering efficiency of the 2LO phonon also suffered a resonance enhancement of ~50 which was significantly greater than the corresponding factor of ≤10 for the case of the LO phonon scattering efficiency, as measured by Trommer and Cardona [3.42]. The same result would also arise if there were defects or impurities in the sample as these would shift and broaden the $E_1$ gap resonance, this effect has also been seen by Menéndez et al. [3.43] in CdHgTe.

It has also been shown in the work of Watt et al. [3.44] that the manufacturing of nanostructures on the surface of semiconductors, which may be viewed as a form of damage albeit controlled and intentional, exposes crystallographic directions that were not exposed prior to the fabrication step. This means that light scattering selection rules for that surface in effect breakdown and previously forbidden scattering processes can occur. An example of this was the presence of the symmetry forbidden TO phonon after cylinders

were fabricated at the (100) surface of GaAs. Away from the patterned area there was only scattering from the LO phonon, as predicted by the selection rules.

### 3.5.3 Effect of Reduced Dimensions on Phonons

There are many interesting effects which are predicted to manifest themselves in structures which have sub-micron dimensions. Several reviews on the subject have been written [3.45, 3.46, 3.47, 3.48]. There now follows a brief discussion concerning such effects.

#### 3.5.3.1 Zone Folding

If there is a periodic structure within the crystal with a period, d, greater than the crystal lattice, such as a superlattice, this has the effect of folding the Brillouin zone onto a zone limited by $\mathbf{k}_{max} = \frac{2\pi}{d}$, which is less than the usual $\mathbf{k}_{max} = \frac{2\pi}{a}$, where a represents the interatomic spacing. This occurs because of the inverse nature of the reciprocal lattice [3.49], the larger period producing a smaller range of wavevectors.

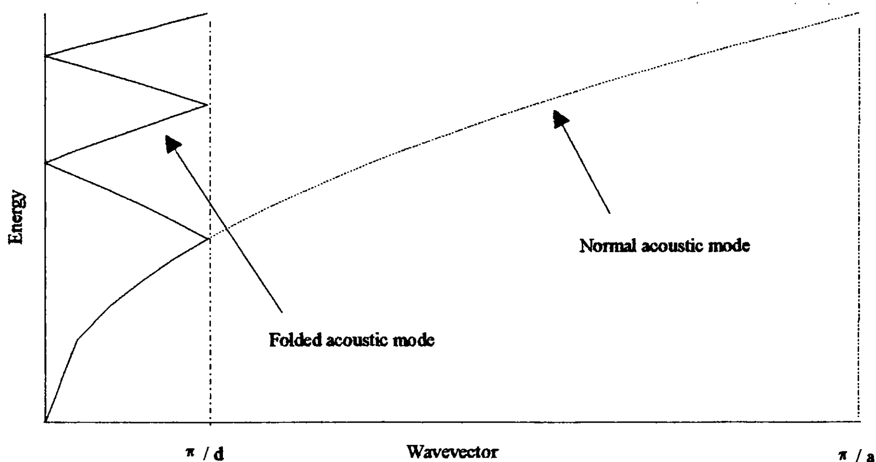


*Figure 3.16* Schematic diagram showing a normal acoustic mode in a lattice of periodicity *a* and the folding effect caused by another, larger, periodicity *d*.

The reduction of the available wavevectors folds the phonon dispersion curve back upon itself towards **k**=0, when it reaches **k**=0 the curve is again folded back and the process is repeated. This is shown diagrammatically in *Figure 3.16.*

### 3.5.3.2 Confined Phonons

The existence of different materials grown next to each other, as is the case in heterostructures and superlattices, can lead to extremely interesting effects occurring. For a phonon to propagate from one material to the next it must satisfy certain boundary conditions given by the dielectric continuum *DC* model [3.48, 3.50]. The requirements laid down by the DC model are:

$$\nabla \times \mathbf{E} = 0 \tag{3-38}$$

and

$$\nabla \cdot \mathbf{D} = 0 \tag{3-39}$$

where $\mathbf{E} \equiv$ electric field

$\mathbf{D} \equiv$ electric displacement

Also the potential function ,$\Phi$, must satisfy Bloch's theorem.

Now consider the above stipulations applied to a material system consisting of two different materials which are differentiated by the subscripts 1 and 2. Let us define the period of the superlattice to be d, this is the sum of the periods of layers 1, $d_1$, and layer 2, $d_2$. It is possible to define a unit cell, and hence a Brillouin zone, peculiar to the superlattice, containing $N_0$ primitive unit cells, i.e. in this case $N_0$=2. The growth direction is taken to be in the z-direction and this enables superlattice wavevectors to be defined: $k_z$ in the z-direction; and due to the isotropy and translational symmetry in the transverse direction, a transverse wavevector $k_T$, perpendicular to $k_z$. Let us also define the

wavevector $k_1$ such that $\omega=\omega(k_1)$, with $\omega(k_1)$ being the dispersion relation in bulk material 1. A similar wavevector $k_2$ is defined for material 2.

From the Lyddane-Sachs-Teller relation for the dielectric function [3.47]:

$$\varepsilon(\omega)=\varepsilon_{\infty}\frac{\omega^2-\omega_{LO}^2}{\omega^2-\omega_{TO}^2} \tag{3-40}$$

where $\omega_{LO}$ = longitudinal optical phonon frequency

$\omega_{TO}$ = transverse optical phonon frequency.

Bungaro et al. [3.47] and Huang and Zhu [3.50] showed that the phonon wavefunction $\Psi(\mathbf{r})$ for each mode had to satisfy the following Laplace equations within the different regions 1 and 2:

$$\varepsilon_1(\omega)\nabla^2\Psi(\mathbf{r})=0 \tag{3-41}$$

$$\varepsilon_2(\omega)\nabla^2\Psi(\mathbf{r})=0 \tag{3-42}$$

To satisfy Bloch's theorem the potential is defined [3.48]:

$$\Phi=e^{ik_T x}f(z) \tag{3-43}$$

with

$$f(z+d)=e^{ik_z d}f(z) \tag{3-44}$$

Consider the modes vibrating at a frequency equal to that of the bulk LO mode in material 1. For such modes, in material 1, the dielectric function, and so the displacement, equal zero thus satisfying *Equation 3-41*. However in material 2 the dielectric function is

non-zero and *Equation 3-39* requires $\nabla \cdot \mathbf{E} = 0$, hence we obtain for material 2:

$$\frac{d^2 f(z)}{dz^2} = k_T^2 f(z) \tag{3-45}$$

If $z = 0$ is chosen to be the centre of material 1 we may solve this equation by setting for material 1:

$$f(z) = A_1 \sin(k_1 z) + B_1 \cos(k_1 z) \tag{3-46}$$

and for material 2:

$$f(z) = A_2 \sinh(k_T z) + B_2 \cosh(k_T z) \tag{3-47}$$

Applying the boundary conditions gives $A_2 = B_2 = 0$. If $A_1$ is set to zero then we must have:

$$\cos(k_1 z) = 0 \tag{3-48}$$

This implies:

$$k_1 z = \frac{\pi}{2}, \frac{3\pi}{2}, \text{etc.} \tag{3-49}$$

The distance to the interface is $z = \frac{d_1}{2}$ hence:

$$k_1 = \frac{m\pi}{d_1} \qquad m = 1, 3, 5, \text{etc.} \tag{3-50}$$

If $B_1$ is set to zero a similar argument gives:

$$k_1 = \frac{n\pi}{d_1} \qquad n = 2, 4, 6 \text{ etc.} \tag{3-51}$$

If the phonon frequency, $\omega$, is such that it forces the dielectric function of material 1 to equal zero, then the phonon wavefunction, $\Psi$, is different from zero only within material 1. This leads to *confined phonons* in material 1 [3.47, 3.48]. Similar results can be obtained for material 2.

Let us now consider the repercussions of $\omega$ being such that neither of the dielectric functions are zero, this allows $\Psi$ to be non-zero in both material 1 and material 2. For this case the phonons are known as *interface modes* [3.47, 3.48]. It should be noted that the amplitude of the interface modes decreases rapidly as the distance normal to the interface increases.

Bungaro et al. [3.47] have shown that similar arguments to the above can be extended to calculate the effect of confining the phonon in another dimension, i.e. restricting its movement to one dimension, as is the case in *quantum wires*. Allowing $L_y$ to represent the size (width) of the wire in the *y*-direction and $L_z$ to represent the wire size (thickness) in the *z*-direction, as shown schematically in *Figure 3.17*, the above authors calculated:

$$k_\alpha^y = \frac{\alpha\pi}{L_y} \quad \textbf{(3-52)}$$

$$k_\beta^z = \frac{\beta\pi}{L_z} \quad \textbf{(3-53)}$$

where $\alpha$ and $\beta$ represent integer quantum numbers corresponding to the confined phonon modes along the *y*- and *z*-directions respectively.

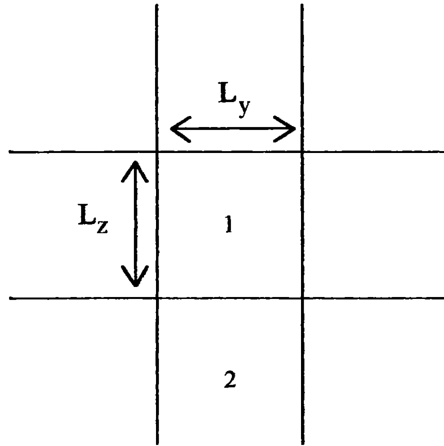


*Figure 3.17* Schematic diagram of a cross-section in the *yz*-plane of a rectangular *quantum wire* as considered by the macroscopic model discussed in the text. The central shaded region, material 1, is surrounded by material 2.

A microscopic model has been suggested in an attempt to explain fully all of the observed phenomena but this goes beyond the scope of this thesis, see Menéndez [3.48] and Rücker et al. [3.51]. The DC model does lead to some incorrect conclusions, none of which are relevant here, but one should be aware of its limitations. It proves impossible to differentiate between the confinement directions for interface phonons in the DC model and both the *y*- and *z*-directions result in the same interface phonon dispersions. This is not the case unless a square wire cross-section is considered, as was the case for Bungaro et al. [3.47]. The two models lead to opposite symmetries for the confined modes. However, the microscopic model has been confirmed experimentally [3.52]. This has important consequences when investigating resonant phenomena in quantum wells. Huang and Zhu [3.50] have suggested the DC model *m*th mode corresponds to the *(m+1)* mode of the microscopic model thereby both models give the same result. To couple an electronic subband with itself the phonon potential has to have even symmetry which is the case for m = 2, 4, 6 etc. for the microscopic case. Hence it is these modes that should be enhanced under resonant conditions and this is indeed the case according to the results of Sood et al. [3.52]. *Equation 3-50* and *Equation 3-51* vary depending on which model is used. The

denominator changed from $d_1$ (= $N_1d$) for the macroscopic case to $(N_1+1)d$ for the microscopic case due to As atoms at both interfaces participating in the vibrations of a given layer.

For the special case of cylinders Watt et al. [3.44] took the theoretical calculation of Ruppin and Englman [3.53] to obtain the frequency of the surface phonons:

$$\frac{\omega_{nh}^2}{\omega_{TO}^2} = \varepsilon_0 - \frac{\varepsilon_m \rho_{nh}}{\varepsilon_\infty} - \varepsilon_m \rho_{nh} \tag{3-54}$$

where:

$$\rho_{nh} = \frac{K_n'(hR) I_n(hR)}{K_n(hR) I_n'(hR)} \tag{3-55}$$

with $\omega_{nh} \equiv$ surface phonon frequency of order n for a propagation constant h

$\omega_{TO} \equiv$ bulk TO phonon frequency

$\varepsilon_m \equiv$ dielectric constant of surrounding medium

$R \equiv$ radius of cylinder

$I_n$, $K_n \equiv$ modified Bessel functions of order n

$I_n'$, $K_n' \equiv$ first derivatives of the above.

# Chapter 4

# Results

## 4.1 Introduction

In this chapter the experiments are detailed and the results obtained from them are given. The chapter is split so that the first section deals with ZnSe. This section is further divided to deal with photoluminescence experiments concerning the as-grown samples and the samples after being subjected to a uniform flat etch, i.e. there were no patterns written on the sample surface prior to the etching. Raman scattering experiments were then carried out on the same samples.

The next section of the chapter deals with ZnTe. This section follows a format similar to that described above for ZnSe.

The chapter continues with an account of the fabrication of nanostructures in the form of wires into the surface of ZnTe. This includes details of the development of the lithographic process. The nanostructures were successfully etched and then were examined using Raman scattering. There is a brief discussion of points to be borne in mind when comparing spectra. Various experiments were designed to investigate unambiguously the etched samples with the aim of assessing the damage caused to the sample by the etching of the nanostructures. The samples were also examined by photoluminescence spectroscopy before and after etching as part of the investigation.

The chapter finishes with details of the fabrication steps used to fabricate cylinders in the surface of ZnTe and the subsequent assessment of these nanostructures by Raman scattering.

## 4.2 Zinc Selenide

Two samples of ZnSe were received from Thomson-CSF in France. The structures *ZS129* and *ZS134*, consisted of 0.53 μm and 0.58 μm of ZnSe, respectively. They were grown using MOCVD at 400°C on the (100) face of an undoped GaAs substrate. There was a lattice mismatch between the materials of 0.26%. Initially, sample *ZS129* was cleaved into four pieces. One piece was kept as a control while the others were etched in differing ratios of methane hydrogen ($CH_4/H_2$).

### 4.2.1 Low Temperature Photoluminescence of Zinc Selenide

The configuration of the laser and spectrometer used for the photoluminescence experiment was that of near backscattering (NBS) where the light impinged upon the sample at an angle of incidence of ~5°. Using true backscattering means that the light from the laser impinges on the sample at right angles to the surface. However, since the light is passing from a material of lower refractive index (air) to one of higher refractive index (ZnSe) then according to Snell's Law the light is refracted and bends towards the normal. Provided the angle of incidence is small enough the angle of refraction is zero and the situation becomes analogous to true backscattering.

Since the band gap of ZnSe occurs at 2.82 eV (4397 Å) at 4 K, the laser line chosen to excite the crystal was the 3638 Å line which required UV optics to be used in the laser. The laser beam was steered by mirrors through neutral density filters. A

combination of these filters was used to obtain the required power at the cryostat window. The light was directed through the filter monochromator to remove any unwanted plasma lines from the laser and then via more mirrors to a focusing lens which focused the light to a spot, typically $\leq 0.5$ mm$^2$, at the sample surface. The CCD camera was used to locate the spot on the sample in the cryostat.

The luminescence was collected by a collimating lens placed in front of the cryostat window. This collecting lens had a large diameter (80 mm) so that it collected as much emitted light as possible. It should be noted that direction does not have a crucial bearing on photoluminescence experiments since the direction of the emitted light is random. The collimated light was then passed through a focusing lens, of a similar diameter to the collecting lens, which directed the light through the entrance slit of the spectrometer.

The slits were adjusted to give the required resolution. The position of the collecting and focusing lenses each had to be finely adjusted in three planes to optimise the number of photons incident on the detector. Neutral density filters could be included or removed to control the signal intensity so that the detector was not damaged. The incident power was measured using a power meter.

Using an exciting power of 100 mW from the 3638 Å line, with a resolution of 0.7 Å and the sample at 5 K, a spectrum was obtained from the control sample and is shown in *Figure 4.1*.

The origins of the peaks at 5 K have been identified using the assignments of Gutowski et al. [2.1] and are given in *Table 4.1*.

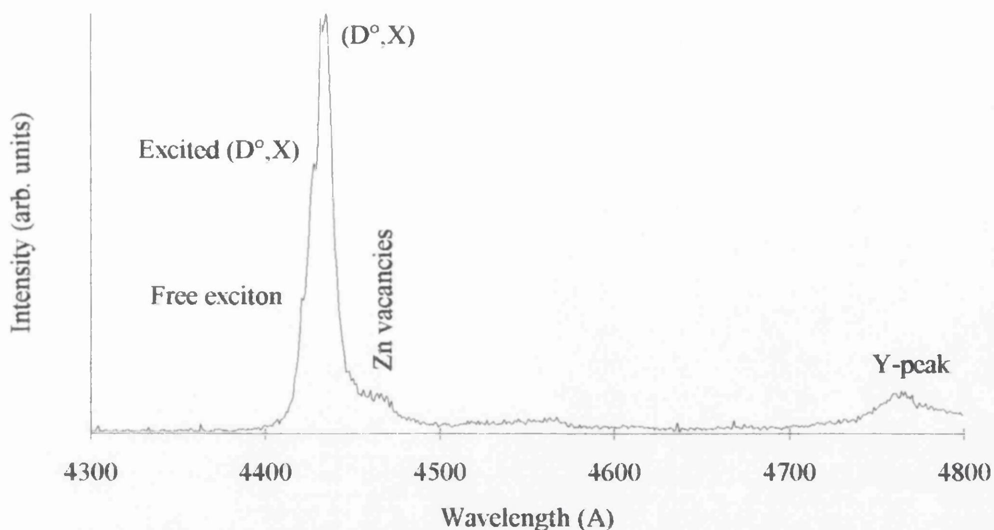


*Figure 4.1* Near band edge photoluminescence spectra from control sample of ZnSe. Temperature = 5 K. 3638 Å excitation. 100 mW at cryostat. 0.7 Å resolution.

| Energy (eV) | Position (Å) | Assignment |
|---|---|---|
| 2.803 | 4424 | Light and heavy hole free exciton |
| 2.798 | 4432 | Excited state of ($D^0$,X) at 4438 Å |
| 2.794 | 4438 | Exciton bound to a neutral donor, ($D^0$,X), labelled I |
| 2.780 | 4460 | Zinc vacancies, $V_{Zn}$ |
| 2.749 | 4510 | First phonon replica of $V_{Zn}$ (separation 31 meV) |
| 2.719 | 4560 | Second phonon replica of $V_{Zn}$ (separation 62 meV) |
| 2.689 | 4610 | Third phonon replica of $V_{Zn}$ (separation 93 meV) |
| 2.605 | 4760 | *Y*-peak, due to dislocations |

*Table 4.1* Position and assignments of peaks occurring in 5 K photoluminescence spectrum of ZnSe.

There is also broad emission occurring at approximately 5300 Å which is due to donor acceptor pairs, see *Figure 4.3a*.

### 4.2.2 Low Temperature Photoluminescence of Reactive Ion Etched Zinc Selenide

Three pieces of ZnSe from sample *ZS129*, were reactive ion etched in $CH_4/H_2$ for one minute while the remaining piece was left as a control. Different ratios of $CH_4$:$H_2$ were used to assess the effect of varying the ratio while all other parameters were kept constant, see *Table 4.2*. The ratios used were 1:2, 1:3 and 1:4 of $CH_4$:$H_2$.

| | |
|---|---|
| Pressure | 20 mTorr |
| RF power | 150 W |
| $V_{DC}$ | ~800 V |

*Table 4.2* Details of etch parameters used to reactive ion etch the ZnSe sample *ZT129*.

The photoluminescence experiment was carried out under similar conditions to those used to obtain the control spectrum. The resulting spectra are shown in *Figure 4.2*.

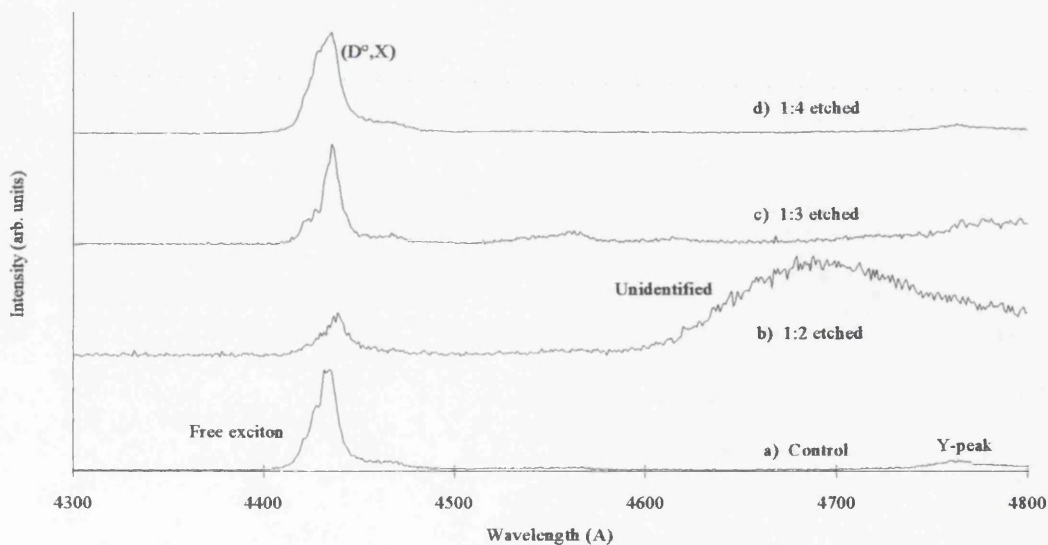


*Figure 4.2* Near band edge photoluminescence spectra from control and etched samples of ZnSe. Temperature = 5 K. 3638 Å excitation. 100 mW at cryostat. 0.7 Å resolution. Spectra have been normalised.

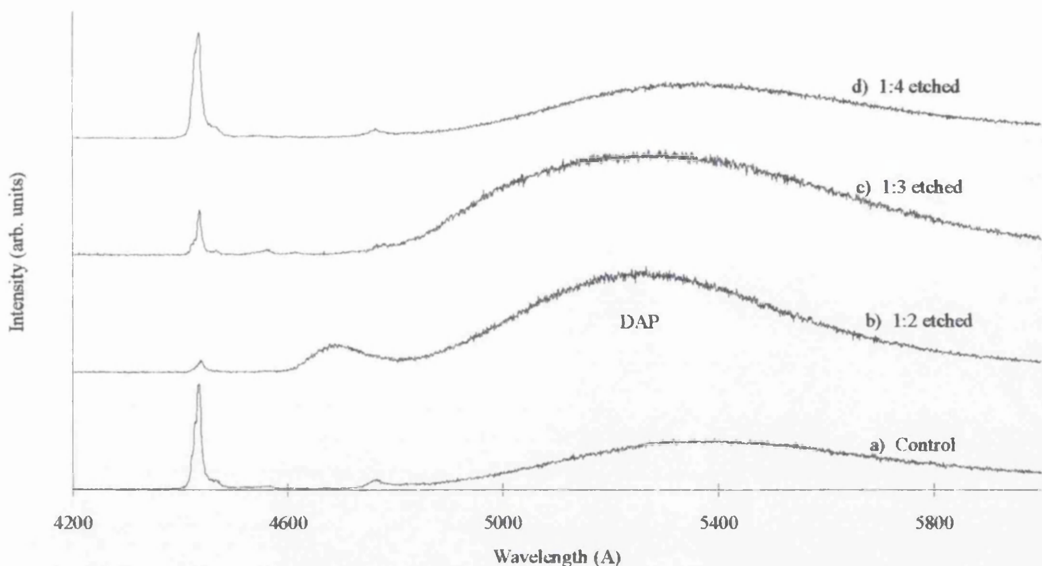


*Figure 4.3* Photoluminescence spectra from control and etched samples of ZnSe. Temperature = 5 K. 3638 Å excitation. 100 mW at cryostat. 0.7 Å resolution. Spectra have been normalised.

Here we see etching with a $CH_4$:$H_2$ ratio of 1:2 leads to a significant increase in the DAP luminescence with respect to the near band edge emission. This emission decreases as the relative amount of hydrogen in the mixture was increased and when the ratio reaches 1:4, the spectrum is very similar to that of the control sample. There also appears a new peak in the spectrum of the 1:2 mixture at 4700 Å, which could not be identified. Since spectra were more like that of the control sample as more hydrogen was added, we did not pursue our investigations into its identity.

The samples were then annealed in pure argon at 200°C for 5 minutes using a Polaron furnace. The samples were examined again using the same experimental conditions as before and the resulting spectra are shown in *Figure 4.4* and *Figure 4.5*.

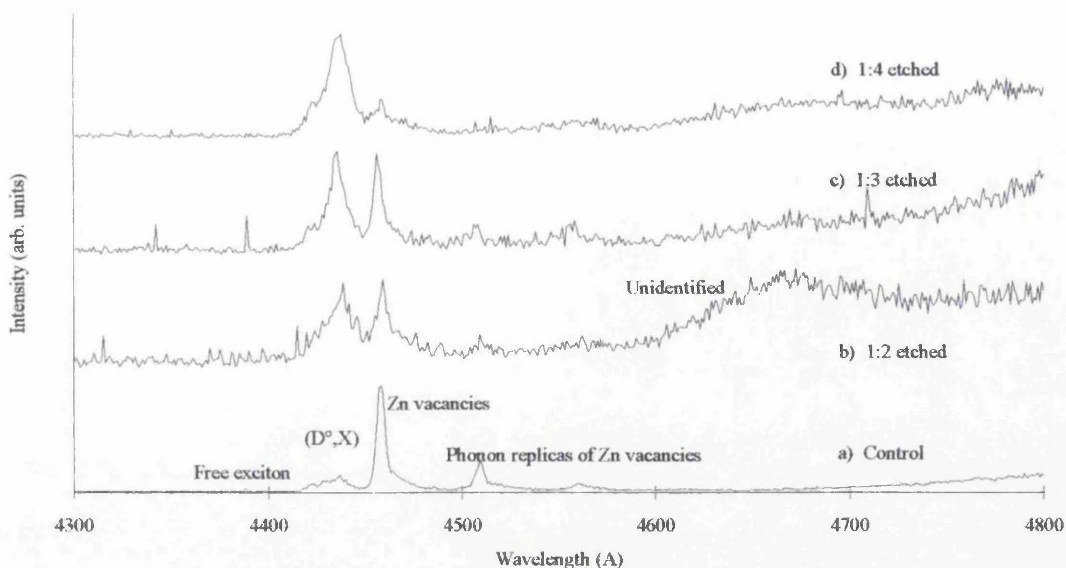


*Figure 4.4* Near band edge photoluminescence spectra from control and etched samples of ZnSe after annealing in Ar for 5 minutes at 200°C. Temperature = 5 K. 3638 Å excitation. 100 mW at cryostat. 0.7 Å resolution. Spectra have been normalised.

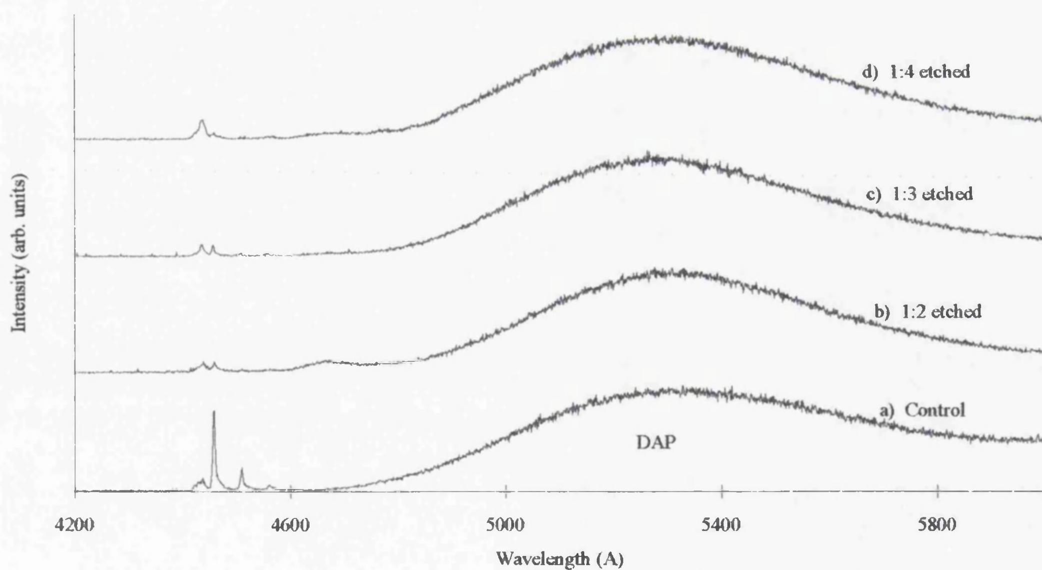


*Figure 4.5* Photoluminescence spectra from control and etched samples of ZnSe after annealing in Ar for 5 minutes at 200°C. Temperature = 5 K. 3638 Å excitation. 100 mW at cryostat. 0.7 Å resolution. Spectra have been normalised.

Here we see there has been a dramatic increase in the DAP emission relative to the near band edge emission and there is more structure visible in the near band edge emission. The spectrum of the sample etched with the 1:4 ratio of $CH_4$:$H_2$ is still the most similar to that of the control sample.

The $CH_4$:$H_2$ ratio was reduced further to 1:8 and 1:10 when etching sample *ZS 134* which had been cleaved into three pieces. Two of the samples were etched for one minute, *Figure 4.6* and *Figure 4.7*, and then all of the samples were annealed at 200°C in Ar for 5 minutes, *Figure 4.8*. We again see the increase in DAP emission after annealing and the increase in bound exciton emission due to Zn vacancies. We also notice a new feature at 4602 Å which is due to a donor acceptor pair involving Ga. The peaks at 4656 Å and 4715 Å are separated by approximately 31 meV and hence are ascribed to its phonon replicas. The emission at 4619 Å is due to a donor acceptor pair involving Cu although there is still some doubt over its identity.

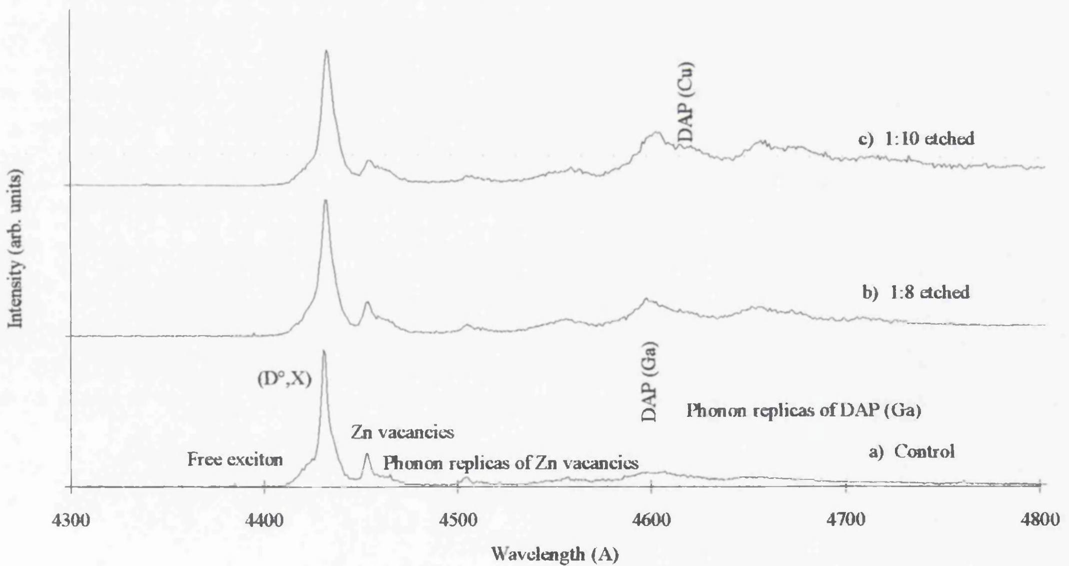


*Figure 4.6* Near band edge photoluminescence spectra from control and etched samples of ZnSe. Temperature = 5 K. 3638 Å excitation. 50 mW at cryostat. 0.7 Å resolution. Spectra have been normalised.

A comparison of these spectra showed that the 1:8 etch gives results more similar to the control than the 1:10 etched sample, both after etching and after annealing. The near band edge emission was found to increase by a factor of twenty after etching and annealing.

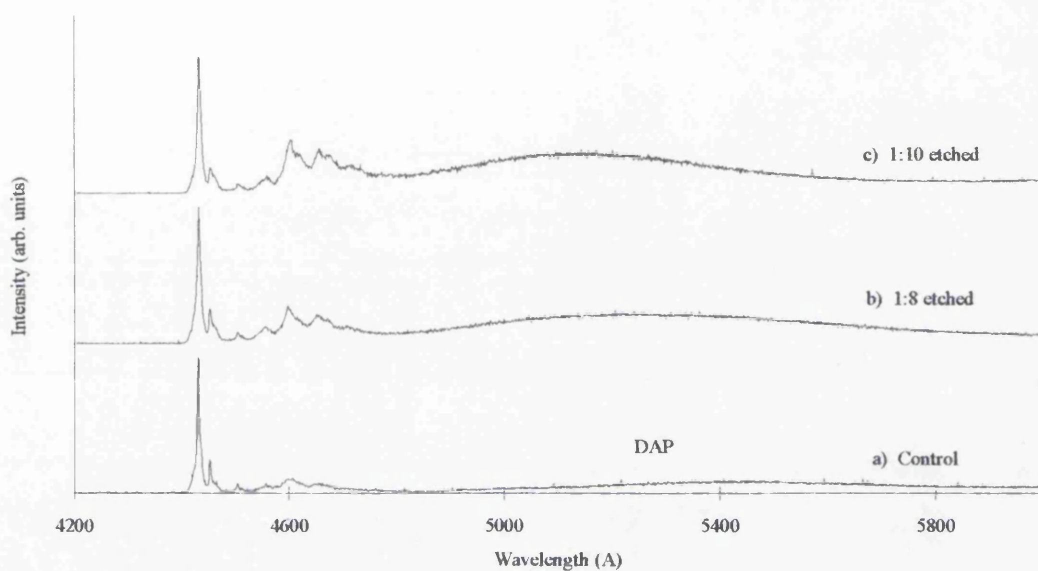


*Figure 4.7* Photoluminescence spectra from control and etched samples of ZnSe. Temperature = 5 K. 3638 Å excitation. 50 mW at cryostat. 0.7 Å resolution. Spectra have been normalised.

From this work we conclude that the ideal ratio of $CH_4$ to $H_2$, as judged spectroscopically, lay between 1:4 and 1:8. Tests carried out to assess the etch anisotropy revealed the 1:8 ratio as the one giving the highest degree of anisotropy, the anisotropy factor was measured to be 0.9. This was assessed using electron microscopy to look directly at etched structures.

This work also suggests that Zn atoms are less strongly bound in the lattice than Se atoms, this is derived as a means of explaining the increase in emission due to Zn vacancies after the annealing process. There was no increase in the emission related to Zn vacancies

after etching when it might be thought a weak inter-atomic link would be vulnerable. This is explained by the fact that the etch process being studied was a flat etch which, it is thought, easily removes the Zn leaving the Se vulnerable to removal by the etch process with the help of its ion bombardment component.

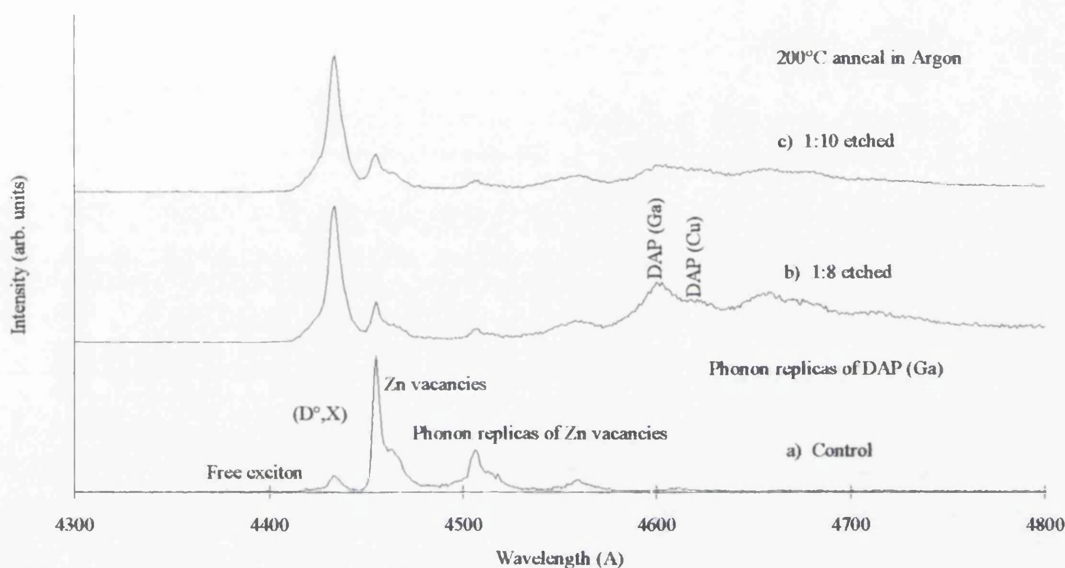


*Figure 4.8* Near band edge photoluminescence spectra from control and etched samples of ZnSe after annealing in Ar at 200°C for 5 minutes. Temperature = 5 K. 3638 Å excitation. 50 mW at cryostat. 0.7 Å resolution. Spectra have been normalised.

### 4.2.3 Room Temperature Raman Spectroscopy of Zinc Selenide

These experiments were carried out at room temperature primarily as a matter of convenience. However, as will be seen later at room temperature we were able to achieve a resonant condition with the band gap of ZnSe and the 4545 Å and 4579 Å lines from the Ar-ion laser. For these experiments the near backscattering (NBS) geometry was used. The selection rules for this geometry dictate that the transverse optical (TO) phonon cannot be created, only the longitudinal optic (LO) phonon when the 100 face of a

zincblende crystal is excited. Since this was to be a preliminary investigation the spectra were not polarised.

Wagner and Hoffman [3.41] showed that the band-gap resonance for scattering from 2LO phonons was much narrower than the band-gap resonance for LO phonon scattering. He also reported there to be a far greater enhancement of the scattering efficiency from the 2LO phonon than from the LO phonon at resonance. Therefore any decrease in the relative intensity of the 2LO phonon intensity to the 1LO phonon intensity could be interpreted as a shift or broadening of the gap resonance caused by damage to the crystal lattice.

Holtz et al. [3.17] carried out work concerning the destruction of crystallographic ordering by ion bombardment. This showed that the 1LO phonon broadened asymmetrically to lower energies and that scattering at lower energies occurred so that the crystalline state gradually deteriorated continuously towards the amorphous state. A summary of his work is given in *Section 3.5.2.5*.

The work by Holtz et al. [3.17] can be related to similar work done by Watt et al. [3.44] who showed that scattering from the TO phonon was possible even in the NBS geometry if the (100) surface was not perfect. An imperfection allows light to couple into other crystallographic directions for which the selection rules do not forbid the TO phonon. Hence the appearance of the TO phonon at 210 $cm^{-1}$ would be another sign of crystalline damage.

*Figure 4.9* shows spectra obtained from the unetched, control sample of ZnSe, from sample *ZS129*. The lower spectrum was obtained using the 4545 Å line while the upper spectrum was obtained using the 4579 Å line. In both cases we see the LO phonon at 250 $cm^{-1}$ from the laser line and the 2LO phonon at 500 $cm^{-1}$ from the laser line, as

expected [2.3]. Using 4545 Å excitation there was more scattering from the 2LO phonon than when the 4579 Å excitation was used. This was because the 4545 Å excitation minus the 2LO phonon energy was closer to the room temperature energy gap of ZnSe and hence the resonance effect was greater. We also see a feature occurring at 4600 Å, the position of which remained invariant under different excitation energies. This implied the peak did not originate from Raman scattering but from a photoluminescent process.

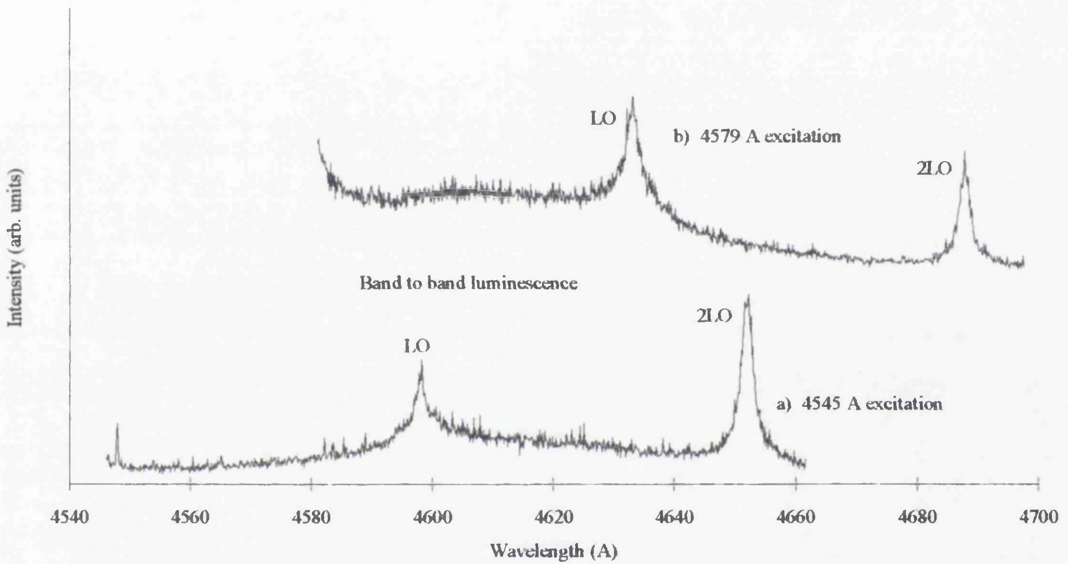


*Figure 4.9* Spectra obtained at room temperature from ZnSe with different excitation wavelengths. 70 mW at sample. Resolution = 0.7 Å. Spectra have been normalised.

A photoluminescence experiment was carried out, starting at 5 K, which enabled the identification of all peaks to be made. The temperature was then increased by intervals of 50 K and the resulting spectra recorded. This enabled the luminescence peaks to be tracked as a function of temperature and the peak observed in the Raman scattering experiment at 4600 Å was positively identified as arising from band to band luminescence.

Excitation with the 4579 Å line was chosen due to the resonance conditions at

room temperature being such that the scattering from the 1LO and 2LO phonons were of approximately the same intensity. Hence any change in the intensity of the 2LO phonon should be immediately obvious.

The four samples used were from *ZS129*, a control and ones uniformly etched for one minute in 1:2, 1:3 and 1:4 ratios of $CH_4$:$H_2$. We see in *Figure 4.10* that the spectra obtained from these samples exhibit none of the expected signs of damage. The relative intensities of the 1LO and the 2LO phonons remained constant and there was no emergence of the TO phonon. The only difference was an increase in the band to band photoluminescence background discussed earlier.

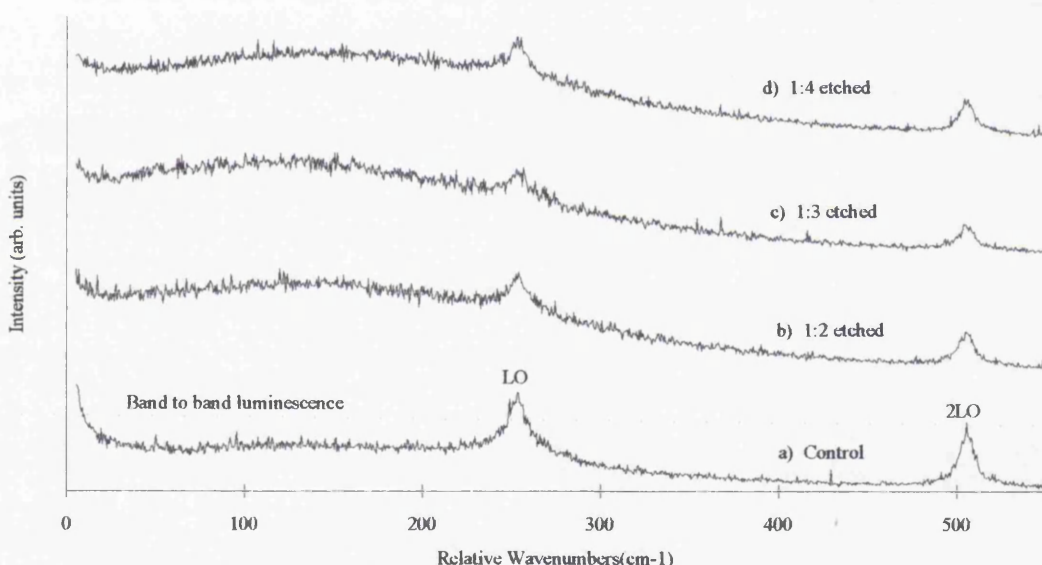


*Figure 4.10* Room temperature Raman scattering spectra obtained from the control and etched samples of ZnSe. 4579 Å excitation. 100 mW at sample. Resolution = 3 $cm^{-1}$. Spectra have been normalised.

The samples were then examined after a period of 5 weeks. During this time the band to band photoluminescence background intensity had decreased. In an effort to reduce it further the 1:3 etched sample was annealed for one minute at 70°C in a mixture

of argon and 5% hydrogen. This resulted in an increase in the background PL, see *Figure 4.11*.

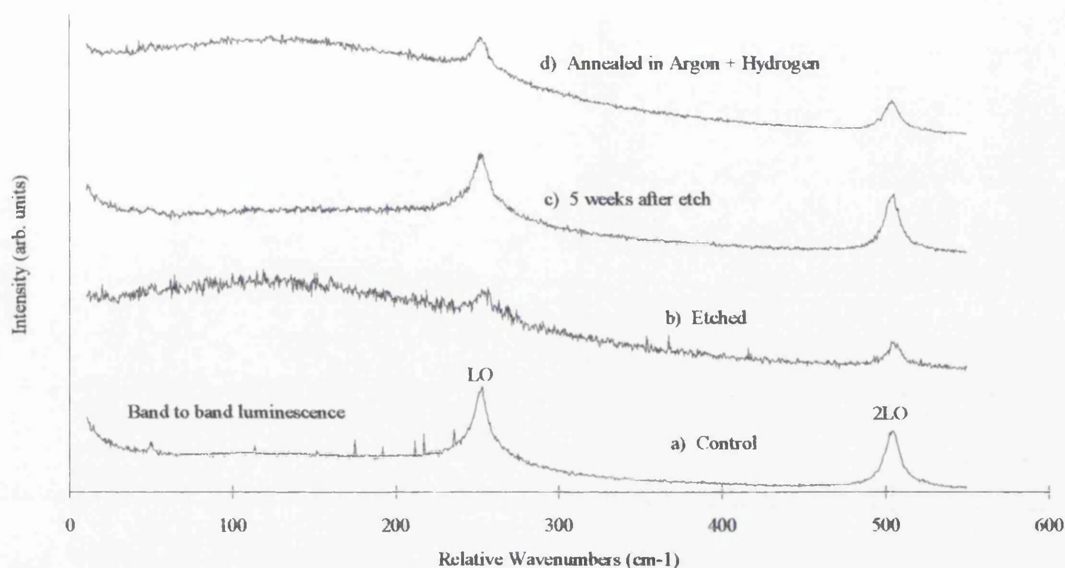


*Figure 4.11* Room temperature Raman scattering spectra obtained from the control and 1:3 etched sample of ZnSe. 4579 Å excitation. 100 mW at sample. Resolution = 3 $cm^{-1}$. Spectra have been normalised.

The 1:2 etched sample was annealed under the same conditions but this time in pure argon as there was concern over a passivation effect due to the hydrogen. The background rose slightly and so the annealing temperature was increased to 150°C where it increased slightly further. The sample was then annealed in argon with 5% hydrogen under the same conditions as the first sample and the background level did not increase, see *Figure 4.12*. This led to the conclusion that annealing had a limited effect on increasing the luminescence background intensity. The annealing possibly helped to desorb hydrogen which was passivating luminescence centres, this is discussed further in Chapter 5. The annealing probably activated other mechanisms by which the luminescence intensity increased, such as by improving the crystallographic order.

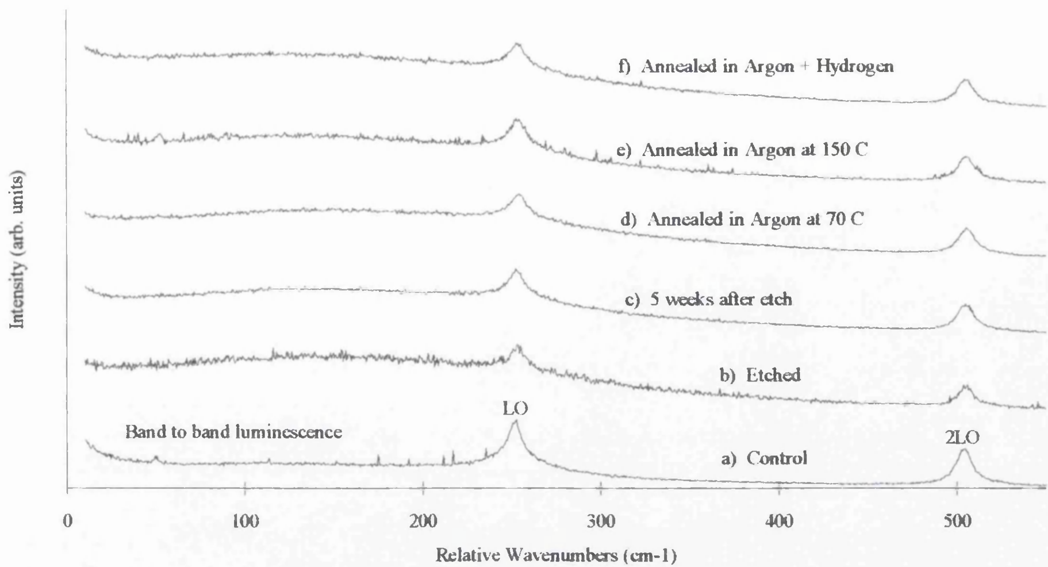


*Figure 4.12* Room temperature Raman scattering spectra obtained from the control and 1:2 etched samples of ZnSe. 4579 Å excitation. 100 mW at sample. Resolution = 3 $cm^{-1}$. Spectra have been normalised.

## 4.3 Zinc Telluride

The low temperature PL spectra of the samples were obtained using a 90° scattering geometry. The 488 nm line of the Ar-ion laser was used to excite the sample which was held at 5 K.

### 4.3.1 Low Temperature Photoluminescence of Zinc Telluride

We see in *Figure 4.13* the 5 K photoluminescence spectrum from the as-grown ZnTe, sample *ZT34*. The excitonic structure in the near band edge region was clearly defined. The peaks at 5209 Å and 5225 Å originate from the strain-split free exciton. From the peak separation a biaxial strain of 0.09% was calculated. This strain resulted from an incomplete relaxation of the large mismatch strain of 7.48%, and the thermal strain

of 0.15% due to the difference in thermal expansion coefficients of the ZnTe epilayer and the GaAs substrate. The dominant peak, occurring at 5236 Å was identified as an exciton bound to an Arsenic acceptor following the assignment of Wagner et al. [4.1]. The shoulder to the low energy side of the large peak is another acceptor bound exciton which cannot be identified. The 6LO and 7LO Raman scattered lines were also present at 5201 Å and 5258 Å respectively, these were a useful magnitude of intensity indicator and also provided an easy wavelength calibration. The peak at 5269 Å could not be identified. These assignments are tabulated below in *Table 4.3*.

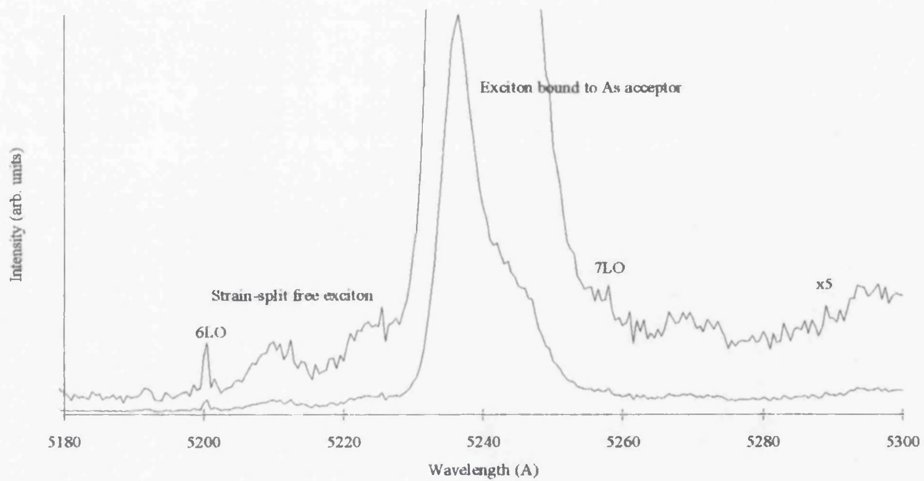


*Figure 4.13* Low temperature (5 K) photoluminescence spectrum of as-grown ZnTe. 4880 Å excitation. 70 mW at cryostat. Resolution = 0.7 Å.

| **Energy (eV)** | **Position (Å)** | **Assignment** |
|---|---|---|
| 2.384 | 5201 | 6LO phonon |
| 2.380 | 5209 | Strain-split free exciton |
| 2.373 | 5225 | Strain-split free exciton |
| 2.368 | 5236 | Exciton bound to an arsenic acceptor |
| 2.358 | 5258 | 7LO phonon |

*Table 4.3* Position and assignments of peaks occurring in 5 K photoluminescence spectrum of ZnTe.

### 4.3.2 Low Temperature Photoluminescence of Reactive Ion Etched Zinc Telluride

The sample *ZT34* was then cleaved into four pieces, three of which were reactive ion etched in $CH_4/H_2$ for five minutes while the fourth piece was retained as a control. Three ratios of methane to hydrogen were used 1:6, 1:8 and 1:10. The photoluminescence spectra obtained after etching are shown in *Figure 4.14* together with the spectrum obtained from the control sample as a comparison. Assuming the intensity of the Raman lines to be constant, the overall intensity of the near band edge luminescence has decreased in all cases by two orders of magnitude with respect to the control sample. The most dramatic reduction in intensity occurs for the exciton bound to the arsenic acceptor and correlates well with the proportion of hydrogen in the etch gas, i.e. the greatest reduction in intensity occurs for the 1:10 ratio of $CH_4/H_2$ etch gas. This implies that hydrogen incorporation is the cause of the decrease in the intensity of the acceptor bound exciton. Similar reductions in PL intensity have been reported in other p-type semiconductors after exposure to hydrogen, see for example it's effect on CdTe [4.2, 4.4] and Si [4.4].

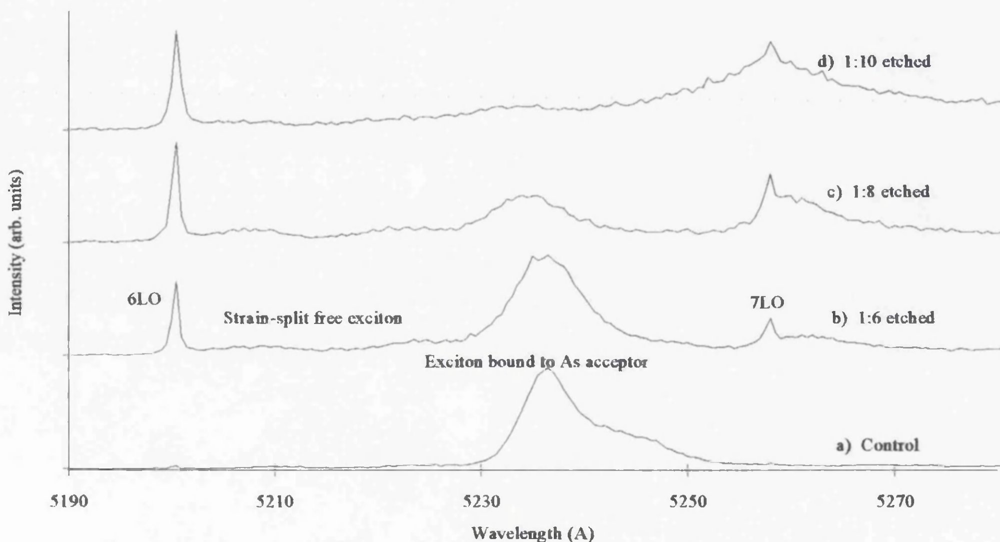


*Figure 4.14* Low temperature (5 K) near band edge photoluminescence spectra of a control and three etched samples of ZnTe. 4880 Å excitation. 10 mW at cryostat. 0.5 Å resolution. Spectra have been normalised.

The effect of reactive ion etching on the deep level emission is shown in *Figure 4.15*. In the spectrum obtained from the control sample donor acceptor pair (DAP) emission can be seen at 5379 Å. The FWHM of this peak was 12 meV and has two phonon replicas at lower energies. There is also a small peak visible at 5669 Å which Moisan [4.5] ascribes to states bound to extended defects at the ZnTe/GaAs interface. After etching there is a decrease in intensity of the DAP emission in line with that of the exciton bound to the As acceptor, this therefore indicates the DAP emission involves an unknown donor recombining with an As acceptor. This conclusion agrees with the ionisation energy of As, 78.3 meV [4.1], assuming a donor ionisation energy of 18 meV [2.3]. The deep level spectra of the etched samples show two new broad features to lower energies than the DAP. At 5560 Å there was a peak associated with a Zn vacancy complex [4.6, 4.7]. The peak reported here is somewhat broader than that reported by the authors above who reported a FWHM of 15 meV. Analysis of this spectrum gives a FWHM of 61 meV. This suggests a similar complex but with a much larger range of energies due to crystallographic disorder induced by reactive ion etching and enhanced by the strain fields at the ZnTe/GaAs interface. At 5767 Å there was a peak again associated with states bound to extended defects at the ZnTe/GaAs interface [4.5]. This peak has also been observed but not identified by Wilson et al. [4.6] in both MBE and MOVPE grown ZnTe/GaAs.

The samples were then annealed in flowing nitrogen at 250°C for 15 minutes in an attempt to remove the hydrogen thought to be incorporated into the samples during etching. For the purposes of comparison, the control sample was also annealed. After annealing low temperature PL was carried out on the samples and the resulting spectra are shown, *Figure 4.16* shows the near band edge emission while *Figure 4.17* shows the deep level emission.

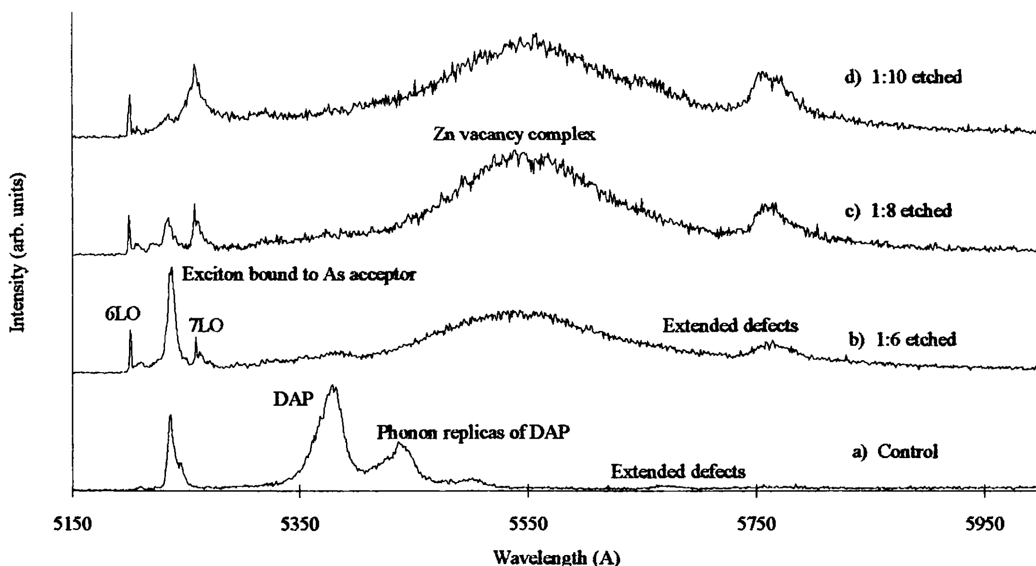


*Figure 4.15* Low temperature (5 K) photoluminescence spectra of a control and three etched samples of ZnTe. 4880 Å excitation. 10 mW at cryostat. 0.5 Å resolution. Spectra have been normalised.

The near band edge spectrum of the control sample revealed no great changes, there was no significant broadening of the dominant bound exciton emission. However, the intensity of the DAP emission was very much reduced. Contrary to this, the etched samples showed marked differences in their spectra after annealing. All of the spectra now bear more resemblance to that of the control sample with the dominant As bound exciton displaced to higher energies by 2 meV in all cases. Complementary work involving the annealing of etched samples in flowing Ar gave similar results. The FWHM of the peak has broadened by less than 0.5 meV, suggesting there has been minimal degradation in the optical quality of the material. The overall intensity of the near band edge emission has increased by more than one order of magnitude.

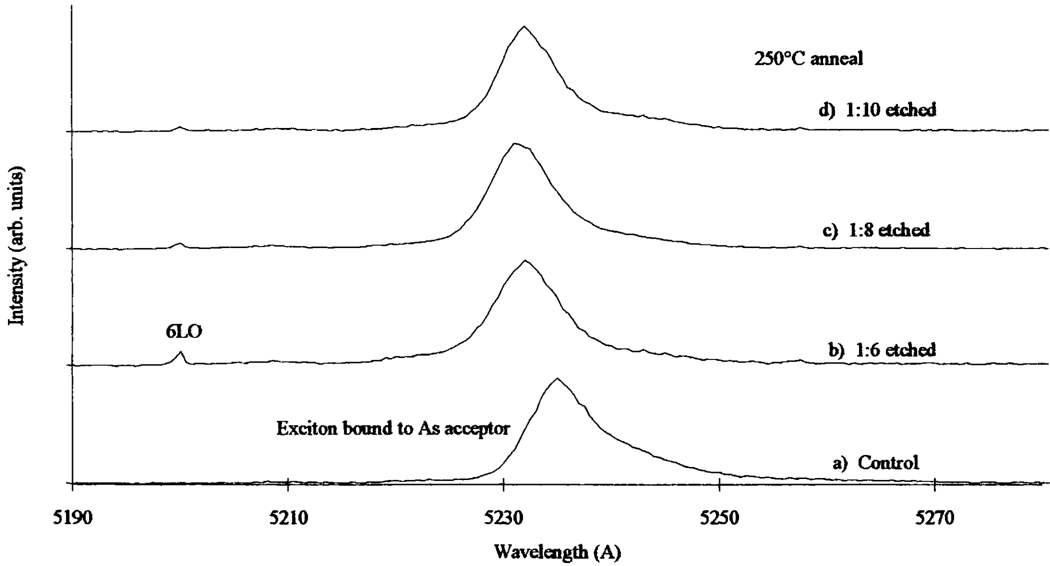


*Figure 4.16* Low temperature (5 K) near band edge photoluminescence spectra of a control and three etched samples of ZnTe after annealing in nitrogen at 250°C for 15 minutes. 4880 Å excitation. 10 mW at cryostat. 0.5 Å resolution. Spectra have been normalised.

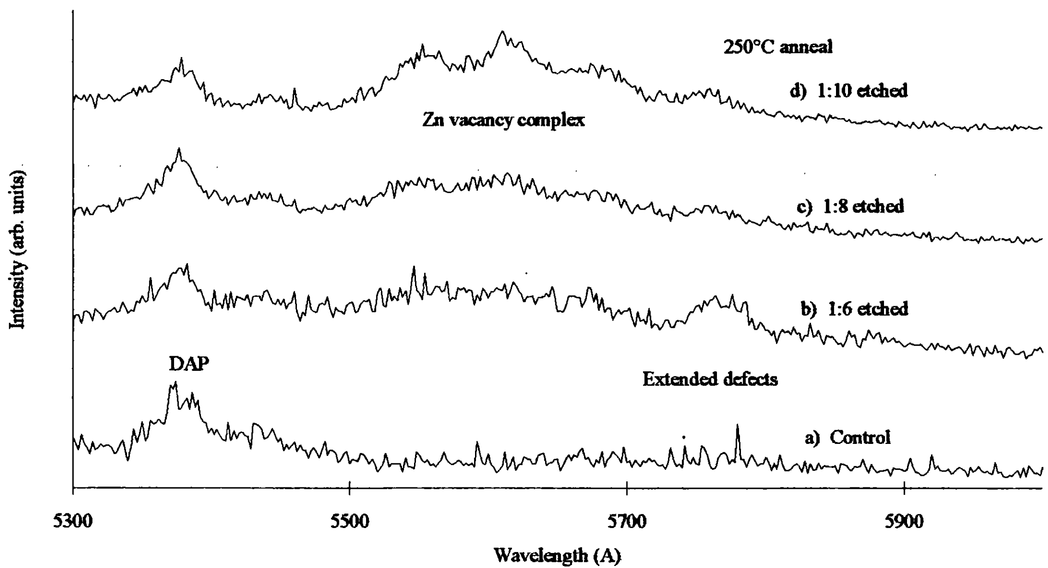


*Figure 4.17* Low temperature (5 K) photoluminescence spectra of a control and three etched samples of ZnTe after annealing in nitrogen at 250°C for 15 minutes. 4880 Å excitation. 10 mW at cryostat. 0.5 Å resolution. Spectra have been normalised.

The deep level emission of the etched samples, after annealing, shows some recovery of the DAP emission intensity, along with its associated phonon replica. The peak at 5767 Å remains but its intensity has been reduced. The broad emission at 5560 Å due to the Zn vacancy complex now has more structure, revealing a definite peak at 5560 Å and two phonon replicas. This now resembles the spectra reported by Wilson et al. [4.6] and Meese and Park [4.7] with a FWHM of 20 meV which is comparable with the value they obtained, confirming the earlier assignment. We can deduce that annealing reduces the etch-induced dislocation damage.

### 4.3.3 Raman Spectroscopy of Zinc Telluride

An as-grown sample of ZnTe, sample *ZT46*, was cleaned using IPA, blown dry with nitrogen and then mounted onto a brass plate using some Bostik. For room temperature measurements the mounting plate was then screwed to an adjustable stage which in turn was positioned on the optical bench. For these experiments the near back scattering arrangement was used. Under these conditions for a zincblende crystal, the TO phonon at 173.8 $cm^{-1}$ [2.3] was forbidden [3.30], only the LO phonon at 209 $cm^{-1}$ [2.3] was allowed.

The laser was focused to a spot at the surface of the sample, the inclusion of a power meter head allowed the power to be measured. The collimating and focusing optics were optimised to give a maximum number of counts. There were no polarisation components included in the initial investigations.

The sample was examined at room temperature using the 5286 Å line of the Ar ion laser. A peak was obtained at 206 $cm^{-1}$ but was extremely weak even with 100 mW of laser power at the sample surface. The excitation wavelength was changed to the 5145 Å line but there was no peak discernible above the noise level. This was due to the

phenomena of resonance discussed in Chapter 3. If the excitation energy is close to the bandgap of the crystal, the Raman scattering process is more efficient, see *Section 3.5.2.2*.

The sample was mounted in the cryostat and taken down in temperature to 5 K. The CCD camera was used to focus the laser spot onto the sample. The collecting optics were then optimised as before to give the maximum number of counts.

Using the 5145 Å line of the laser the following spectrum, shown in *Figure 4.18*, was obtained. The LO phonon was clearly visible at 210 $cm^{-1}$ and was flanked by combinational modes at 207 $cm^{-1}$, 215 $cm^{-1}$ and 218 $cm^{-1}$. These peaks were due to scattering from LO-TA, LO+TA and LO+LA respectively, where TA represents the transverse acoustic and LA represents the longitudinal acoustic phonons. These phonons can collide and scatter light at energies equal to the sum of their individual energies or one of the phonons can be created with the required energy originating from the LO phonon thereby reducing the energy of the scattered light.

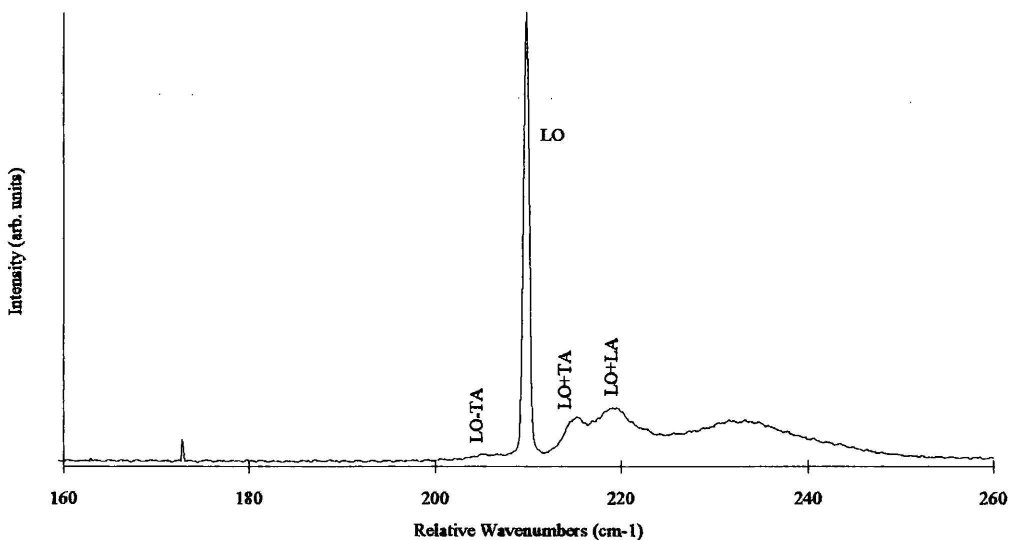


*Figure 4.18* Raman spectra obtained from a control sample of ZnTe at 5 K. NBS. 5145 Å excitation. 1.5 mW at cryostat. 2 $cm^{-1}$ resolution. Unpolarised.

The lattice temperature was increased from 5 K to 10 K, 25 K, 50 K, 75 K, 100 K, 150 K and finally to 200 K. At 200 K the Raman signal could no longer be resolved from the background noise. The intensity of the LO phonon was measured at each temperature using the same input power and the same experimental configuration, allowing time for the temperature to stabilise at each step to within ±0.1°C. The resulting peak intensity was plotted as a function of the sample temperature and the results are shown graphically in *Figure 4.19*. The effect of taking the energy gap of the sample away from the resonance condition with the LO phonon, by increasing the temperature, can be seen clearly as the peak intensity of the LO phonon was reduced dramatically.

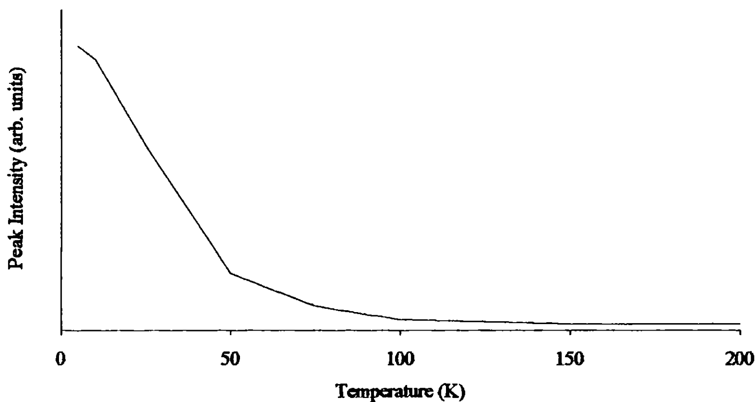


*Figure 4.19* Effect of sample temperature on the peak intensity of the LO phonon of ZnTe. NBS. 5145 Å excitation. 2 mW at cryostat. 2 $cm^{-1}$ resolution. Unpolarised.

Since the 5286 Å line lies to a lower energy than the energy gap of ZnTe at 5 K, the effect of increasing the sample temperature should bring the energy gap nearer to resonance with the LO phonon. The experiment was repeated using the 5286 Å line and the results are shown below in *Figure 4.20*. The peak intensity increased as the temperature was increased, reaching a maximum at 170 K as the band gap came into resonance with the excitation. There is also a shoulder, peaking at 130 K. This was due to the band gap coming into resonance with the excitation with the assistance of the energy

of a LO phonon. As the temperature increased further the peak intensity decayed as for the 5145 Å excitation until it was lost in the background noise at 280 K.

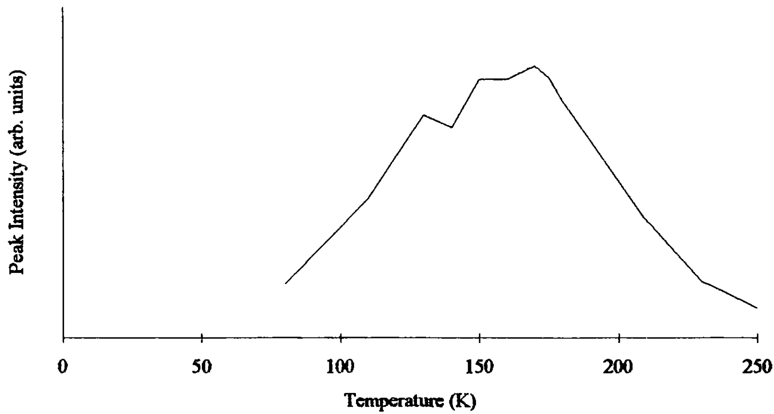


*Figure 4.20* Effect of sample temperature on the peak intensity of the LO phonon of ZnTe. NBS. 5286 Å excitation. 5 mW at cryostat. 2 $cm^{-1}$ resolution. Unpolarised.

### 4.3.4 Raman Spectroscopy of Reactive Ion Etched Zinc Telluride

The sample of ZnTe *ZT46* was cleaved into four pieces and then three pieces were reactive ion etched in methane hydrogen for five minutes, the ratio of the gases was varied for each piece. The samples were not patterned but simply subjected to the etch plasma, this is therefore referred to as a ***flat etch***. The ratios used were 1:6, 1:8 and 1:10 of methane to hydrogen. The samples, including the control sample were then cooled down to 5 K and examined in the near back scattering arrangement using the 5145 Å line as the source of excitation. The light was focused to a spot on the surface of the semiconductor and the scattered light signal was optimised as detailed previously. The scans which resulted are shown below in *Figure 4.21*.

The spectra from the etched samples exhibited no major changes from that of the control sample. The LO phonon did not broaden to lower energies as might have been

expected from the work of Holtz et al. [3.17] and Rama Rao and Sundaram [3.40], nor did the forbidden TO phonon appear as happened in the same experiments. There was a slight decrease in the intensity, with respect to the 1LO phonon, and definition of the combinational modes, indicating some degradation of the crystal lattice. This effect was extremely weak and was put down to the penetration depth of the light, ~100 nm, reaching the interface region near the substrate where the material quality deteriorated due to the lattice mismatch of 8% between the ZnTe and the GaAs.

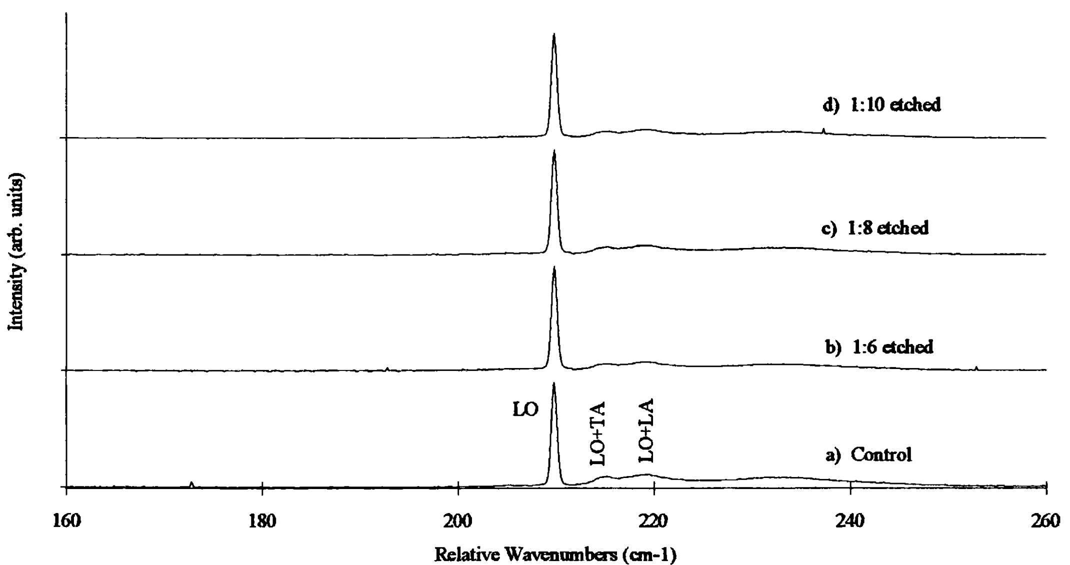


*Figure 4.21* Raman spectra obtained from a control sample and three reactive ion etched samples of ZnTe at 5 K. NBS. 5145 Å excitation. 1.5 mW at cryostat. 2 $cm^{-1}$ resolution. Unpolarised. Spectra have been normalised.

To test this hypothesis a thicker sample of ZnTe, sample *ZT193*, was grown at Regensburg. This consisted of an epilayer of 2.2 μm of ZnTe grown on a standard GaAs substrate. This was etched for five minutes using a 1:8 ratio of methane to hydrogen and examined by Raman spectroscopy at 5 K using the 5145 Å line of the laser and near back scattering so that the results could be compared with those of the above experiment. The

spectra obtained before and after etching are shown below in *Figure 4.22* and show there was no change in the definition of the combinational modes or their intensities relative to the 1LO phonon after etching. We must therefore conclude the Raman scattering experiment did not reveal any signs of significant crystalline damage due to reactive ion etching and the changes seen in the Raman spectra are related to the quality of the interface.

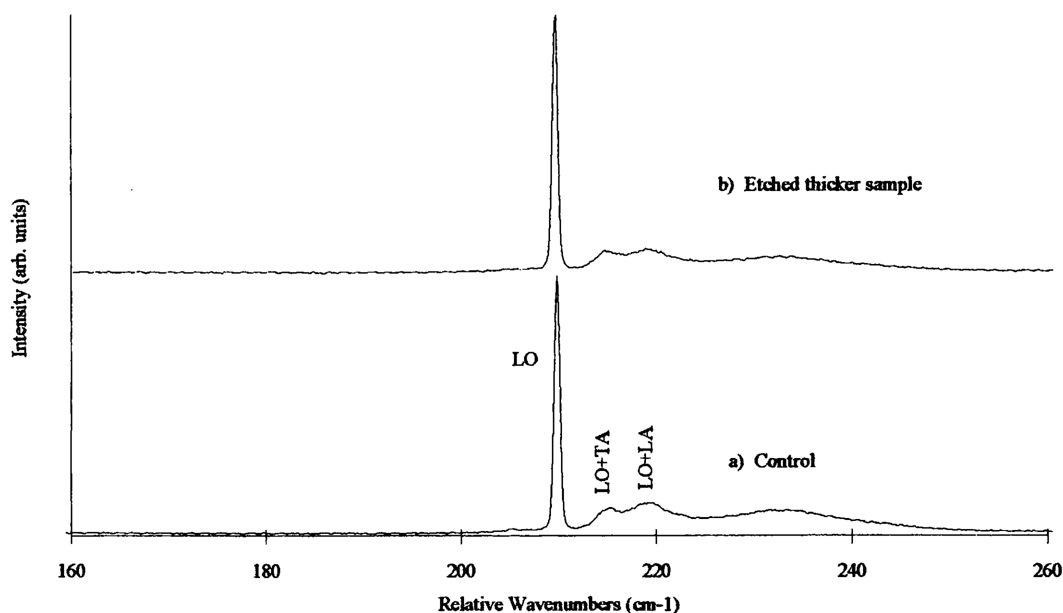


*Figure 4.22* Raman spectra obtained from an unetched control sample of ZnTe and a thicker sample which was etched with the 1:8 ratio of $CH_4/H_2$. NBS. 5145Å excitation. 2 mW at cryostat. 2 $cm^{-1}$ resolution. Unpolarised.

## 4.4 Wires Fabricated in Zinc Telluride

### 4.4.1 Fabrication of Wires

The sample of ZnTe, *ZT55*, used in this section was grown by MOCVD at

Regensburg. It consisted of a 1.8 μm epilayer of ZnTe grown on a (100) GaAs substrate. The single sample was cleaved into two pieces.

To enhance the chances of success with the fabrication the samples had to be as clean as possible. The sample preparation was carried out entirely in a class 100 clean room. The first sample was initially degreased in Trichloroethylene for 5 minutes in an ultrasonic bath, this was rinsed in acetone for 5 minutes in the ultrasonic bath and this in turn was rinsed in IPA for 5 minutes in the ultrasonic bath. The IPA was then evaporated using a nitrogen gun.

To obtain as high a resolution as possible it was decided to use a double layer of polymethylmethacrylate, (PMMA), a positive electron-beam resist, see *Section 3.3.2*. The first layer was 4% BDH PMMA, this solution was chosen initially because it was easier to lift-off than 2.5% BDH.

The pattern was generated using the "CATS" CAD software. It consisted of an array of wires 800 μm long, 60 nm wide and the pitch of the *grating* was 500 nm. The entire width of the pattern was 800 μm giving an area of 0.64 $mm^2$ for the pattern. The pattern was written by a Leica EBPG5 beamwriter, working at 50 keV with a 20 nm spot size. The required exposure was estimated from that used for patterning GaAs at around 800 $\mu Ccm^{-2}$. The atomic masses of Zn and Ga are similar (30 and 31 respectively) indicating the scattering of the electron beam, and therefore the exposure, would be similar, however, the atomic masses of As and Te are quite different (33 and 52 respectively). Hence it was decided to utilise a facility in the beamwriter software to carry out exposure tests varying the exposure over nine patterns, centred roughly on the exposure known from previous work in the department to work for GaAs, ~700 $\mu Ccm^{-2}$. An exposure of 500 $\mu Ccm^{-2}$ was chosen for the first pattern, the exposure was then increased by a factor of 1.1 for each subsequent pattern thereby resulting in an exposure

for the final pattern of 1071 $\mu Ccm^{-2}$.

The exposed pattern was developed in a 3:1 solution of IPA:MIBK at 23°C for 30 seconds, the solution was then rinsed in IPA. The 3:1 solution of MIBK was used as it gave the best resolution. The mask for the dry etch process was a 25 nm thick layer of titanium which was evaporated onto the sample. Acetone at 45°C was used to lift-off the titanium on the photoresist, leaving behind the titanium which had been evaporated directly onto the ZnTe. The acetone was rinsed off using IPA.

The thickness of the titanium mask was important because if it was too thin the dry etching process would etch through the mask leaving the ZnTe unprotected. If it was too thick the titanium on the ZnTe would join with the titanium on the e-beam resist, thereby forming a continuous layer which would not allow the acetone to dissolve the resist during the lift-off procedure thereby preventing lift-off taking place.

After the layer of Ti was subjected to the lift-off procedure it was possible to examine the pattern using an electron microscope. The microscope used for this work was an Hitachi S800. There was no sign of the pattern when the base layer of PMMA was 2.5% BDH. The problem was diagnosed to be the lift-off process since the variation in exposure should have produced patterning. Bearing this in mind the sample was immersed in warm acetone, at approximately 30°C, for 30 minutes to remove all of the Ti. The patterning process was repeated again but this time with 4% BDH for the base layer and 2.5% ELV for the uppermost layer.

This time the pattern was discernible under the electron microscope and the sample was reactive ion etched for six minutes in what was now the standard 1:8 mixture of $CH_4$ to $H_2$. The etch resulted in an anisotropy factor of 0.95. The relevant details of the etch are given in *Table 4.4*.

| $CH_4$ | 5 sccm |
|---|---|
| $H_2$ | 40 sccm |
| Pressure | 20 mTorr |
| RF power | 150 W |
| $V_{DC}$ | ~850 V |

*Table 4.4* Details of etch parameters used to etch wires into the ZnTe sample *ZT55*.

The sample was examined using SEM and the wires were found to be 80 nm wide and 400 nm tall, see *Figure 4.23*. All of the exposures resulted in wires being etched with the exception of the two lowest exposures which were 500 $\mu Ccm^{-2}$ and 550 $\mu Ccm^{-2}$.

*Figure 4.23* SEM micrograph of one of the wire patterns etched in *ZT55*. The wires are 80 nm wide and 400 nm tall.

### 4.4.2 Unpolarised Raman Spectroscopy of Wires

The 80 nm wide wire sample was then examined at 5 K by unpolarised Raman scattering in the region of interest which was 150 $cm^{-1}$ to 1000 $cm^{-1}$, using 5145 Å excitation. A variety of peaks were found, however, when the excitation source was changed to 5017 Å it became obvious that the majority of the peaks originated from photoluminescence see *Section 4.4.3*.

The detected Raman peaks included the 1LO flanked by combinational modes as reported earlier, the 2LO at 421 $cm^{-1}$ and the 3LO at 631 $cm^{-1}$. The presence of a Raman scattered peak at 393 $cm^{-1}$ should also be noted which was due to the 2LO combining with the TO phonon. There was no sign however, of the TO phonon which was still forbidden and therefore there was no sign of crystalline damage.

It was thought the wires were perhaps not tall enough to give the aspect ratio Ruppin and Engleman [3.53] mentioned in their work on cylinders and so the sample was etched for a further 3 minutes.

Upon re-examination at 5 K the Raman spectra obtained appeared to be no different to the flat etched samples. It was noticed however, that at room temperature, under excitation from the 4880 Å line, an increase in intensity in the lower energy region occurred when the sample was examined over the same spectral range. This was more thoroughly investigated and proved to be the high energy tail of one of two large peaks which were identified, see *Section 3.5.2.4*, as the Te A1 and E modes occurring at 121 $cm^{-1}$ and 141 $cm^{-1}$ respectively, the former being the more intense see *Figure 4.24a*. The sample was examined away from the patterned area *Figure 4.24b* and the peaks at approximately 121 $cm^{-1}$ and 141 $cm^{-1}$ were found to have reduced in intensity to a level comparable with the LO phonon. Another sample of ZnTe, *ZT95*, was examined under

similar conditions and the spectra obtained *Figure 4.24c* was very similar to that of the unpatterned areas with the intensities of the peaks at approximately 121 $cm^{-1}$ and 141 $cm^{-1}$ being less than the intensity of the LO phonon.

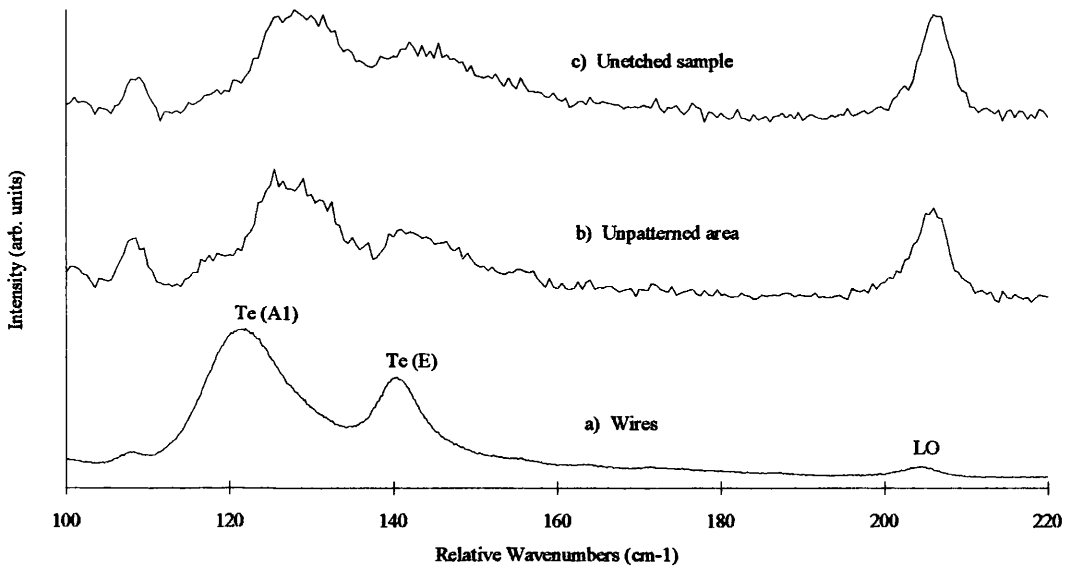


*Figure 4.24* Raman spectra of ZnTe showing differences between etched area patterned with wires; unpatterned etched area; unetched sample. NBS. Samples were at room temperature. 4880 Å excitation. 50 mW at sample. 2 $cm^{-1}$ resolution. Unpolarised. Spectra have been normalised.

It was thought to be of interest to try to reduce the dimensions of the wires still further to investigate the limits of the technique and the effect on the phonons. With this in mind the other piece of the original ZnTe sample *ZT55* was cleaned and coated with a layer of 2.5% BDH which was baked and then a capping layer of 2.5% ELV was spun and baked. The CAD program was changed so that the pattern was only 5 nm wide, this was unlikely to be achieved since the spot was 20 nm in diameter but it was thought it might reduce the dimensions of the pattern. The sample was then patterned by the Leica EBPG5 beamwriter using the exposure test facility with the same exposure values as were used for the previous sample.

Upon developing and evaporating 25 nm of titanium the pattern was visible when inspected using the SEM. The wires in the pattern were measured to be 60 nm wide, see *Figure 4.25*. The sample was etched for six minutes using the standard etch conditions given previously.

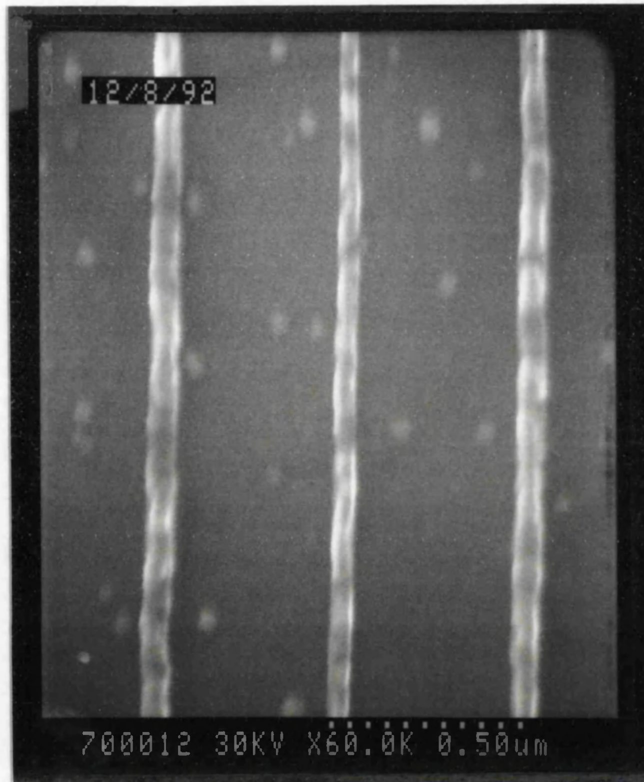


*Figure 4.25* SEM micrograph of the Ti mask after lift-off. The wires in the pattern are 60 nm wide.

The etched wires were then examined using the SEM. Of the nine areas subjected to the exposure test it was found only three of the areas had resulted in wires. These were the patterns which had been exposed with the following e-beam exposures: 605 $\mu Ccm^{-2}$, 666 $\mu Ccm^{-2}$ and 805 $\mu Ccm^{-2}$. Of these the wires in the 605 $\mu Ccm^{-2}$ pattern had fallen over due to their aspect ratio being too great, see *Figure 4.26*. The 805 $\mu Ccm^{-2}$ exposure pattern was only partly printed, it was not known why the 732 $\mu Ccm^{-2}$ pattern was not printed. This left the 666 $\mu Ccm^{-2}$ pattern as the only complete set of wires and all further discussion relates to the wires in this pattern.

The wires were measured using the SEM and found to be 480 nm tall. The wire width was found to decrease towards the top of the wire, starting at 40 nm at the base and tapering to 20 nm at the top implying a positive slope of 1.2° from the vertical, a very high degree of anisotropy, see *Figure 4.27* and *Figure 4.28*.

*Figure 4.26* SEM micrograph showing an angled view of the wire pattern exposed with 605 $\mu Ccm^{-2}$ and etched in *ZT55*. The wires have fallen over due to the anisotropy factor [3.19] becoming too great.

This indicates the electron-beam exposure is absolutely critical for very low dimensional work. For the 80 nm pattern there was a much larger process window and the *ideal* exposure was safely exceeded, however for the smaller wires the exposure had to lie within approximately 10% of the optimum value.

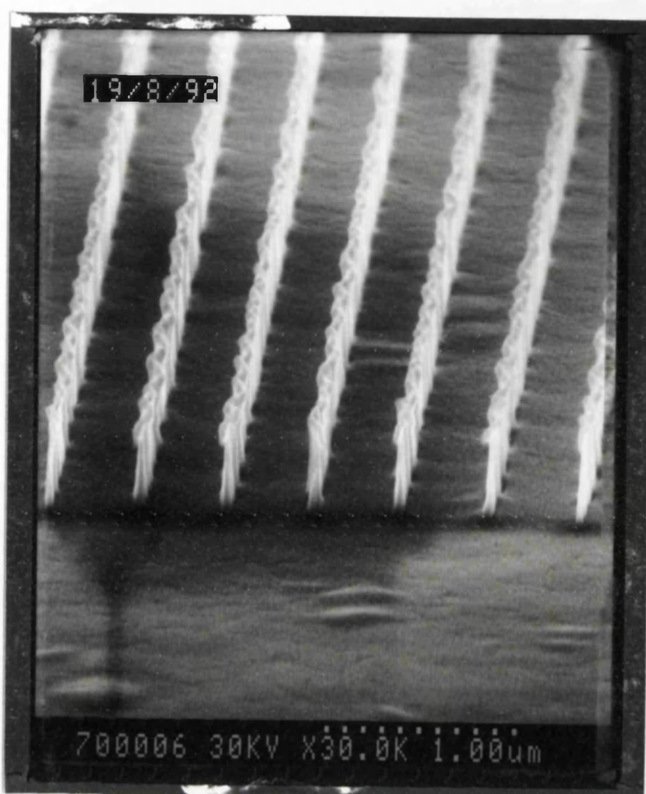


*Figure 4.27* SEM micrograph showing an angled view of the wire pattern exposed with 666 $\mu Ccm^{-2}$ and etched in *ZT55*. The wires were 20 nm wide at the top and 480 nm tall.

### 4.4.3 Effect of Excitation Frequency

The sample was examined by Raman spectroscopy at 5 K using the 5145 Å line of the laser in an NBS configuration. The resulting spectra can be seen in *Figure 4.29a*. The majority of the peaks are relatively broad suggesting they originate from photoluminescence. The two notable exceptions were the two relatively narrow peaks at 210 $cm^{-1}$ and 421 $cm^{-1}$.

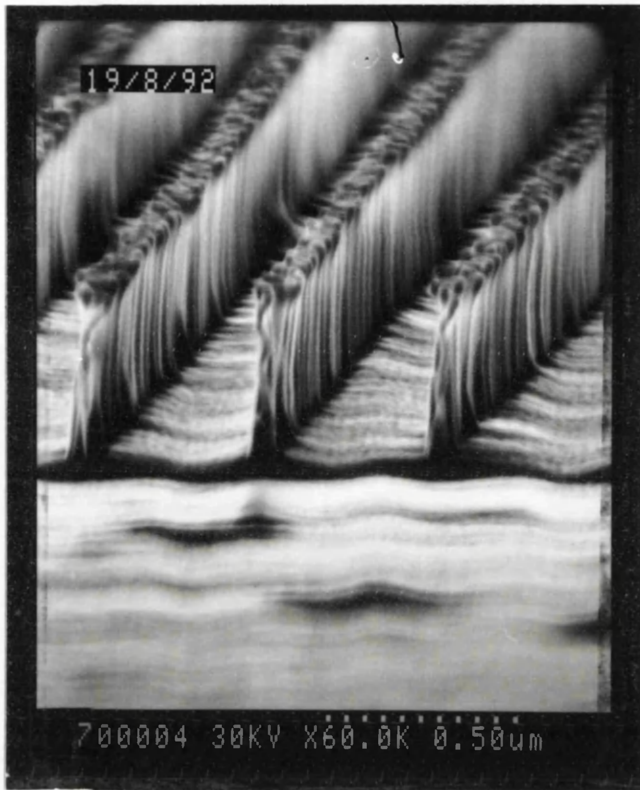


*Figure 4.28* SEM micrograph showing a close-up view of the wire pattern exposed with 666 $\mu Ccm^{-2}$ and etched in *ZT55*. The wires were 20 nm wide at the top and 480 nm tall.

To confirm easily which peaks were luminescence and which were due to Raman scattering, the excitation wavelength was altered to 5017 Å, see *Figure 4.29b*. In theory the Raman scattered peaks remain shifted from the laser line by a constant energy whereas the luminescence emission remains at the same wavelength. In *Figure 4.29b* the excitation wavelength was 5017 Å but the software was fooled into believing it still to be 5145 Å, thus examining the same range of wavenumbers allows a comparison to be made with *Figure 4.29a*. The peaks that do not appear to have shifted in energy are therefore photoluminescence (remember the ordinate of *Figure 4.29* refers to 5145 Å excitation) and it was then possible to confirm by their absence the peaks at 210 $cm^{-1}$, 392 $cm^{-1}$, 421 $cm^{-1}$ and 631 $cm^{-1}$ arose from Raman scattering. These peaks were identified as the 1LO, LO+TO, 2LO and 3LO and phonons respectively.

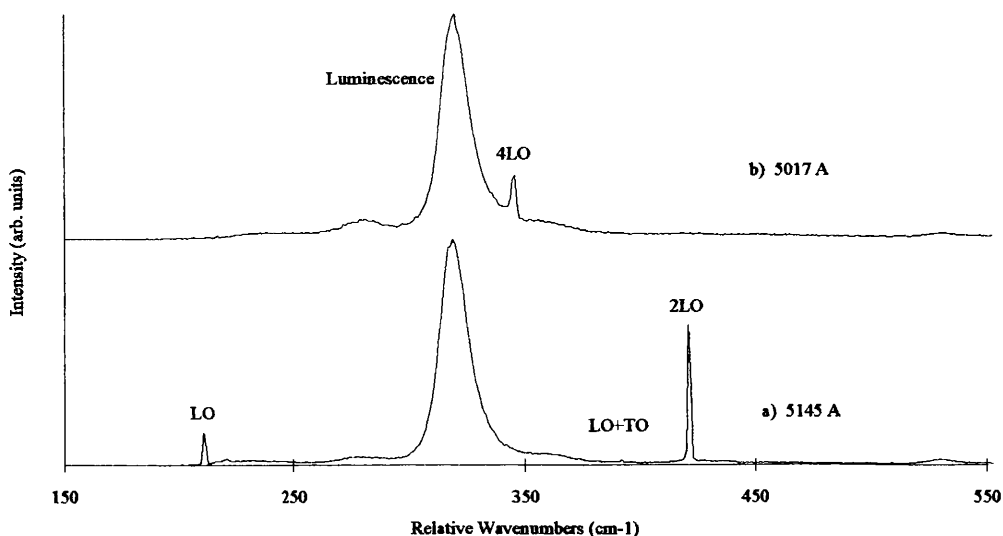


*Figure 4.29* Effect on the Raman spectrum of varying the excitation frequency. NBS. Samples were at 5 K. 30 mW at cryostat. 1 $cm^{-1}$ resolution. Unpolarised. Spectra have been normalised. N.B. the ordinate refers to 5145 Å excitation.

### 4.4.4 Considerations When Comparing Spectra

The previous section highlights the difficulties and dangers of comparing different spectra. Caution had to be exercised when comparing spectra with differing excitation source powers as this led to different sample temperatures which altered the band-gap and hence the resonance conditions. Simple differences in sample temperatures moved the band-gap and so altered the resonance conditions. Changes in the excitation sources affected the resonance conditions and probe depths. Raman spectroscopy by its nature is vulnerable to polarisation changes and care had to be taken to take into account any differences in polarisation before drawing any conclusions from a comparison of spectra. Altering the orientation of the sample was important during experiments involving polarisation since the Raman tensor which dictated the Raman scattering was sensitive to the crystallographic symmetry. These points and their relevance are discussed in more detail below.

#### 4.4.4.1 Effect of Excitation Power

The effect of varying the power on the intensity of the phonon with respect to the 2LO phonon was investigated under 5145 Å excitation with the sample at 5 K. The sample was first excited with 30 mW of optical power, this resulted in *Figure 4.30a*. The power was then increased by a factor of six to give 180 mW at the sample, the resulting spectrum is given in *Figure 4.30b*. Both spectra show clearly the LO and 2LO phonons at 210 $cm^{-1}$ and 421 $cm^{-1}$ respectively. The 2LO is more intense than the LO in both cases, the ratio of the peak intensity of the 2LO to that of the LO was 4.8 in the case of the lower power and 9.6 in the case of the higher power. The broader peaks between phonons arise from photoluminescence.

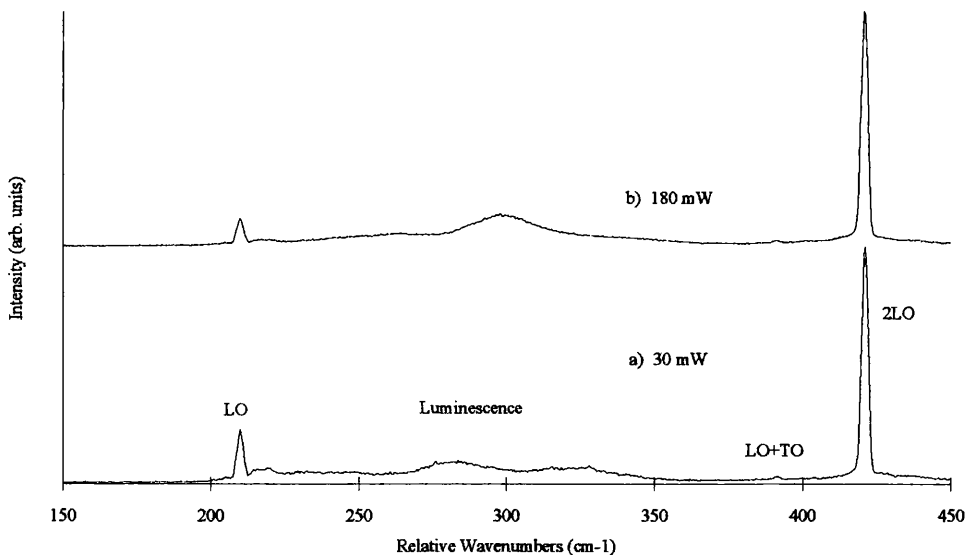


*Figure 4.30* Effect on the Raman spectrum of varying the excitation power. NBS. Samples were at 5 K. 5145 Å excitation. 2 $cm^{-1}$ resolution. Unpolarised. Spectra have been normalised.

Using the higher power it can be seen that the intensity of the LO phonon falls below that of the photoluminescence peak at 298 $cm^{-1}$. It was not known whether the

photoluminescence had increased or the Raman scattering had decreased. The increased power meant more photons were present to excite the electrons in the sample and hence give rise to more photoluminescence emission, which may have been responsible for giving the impression of the relative reduction in the peak intensity of the LO phonon.

It was thought that the relative intensities of the 2LO and LO phonons would be a suitable means of assessing any changes in the spectra since they both arose from a similar scattering process. The extra power also increased the lattice temperature, causing a shift in the luminescence peaks to longer wavelengths which hence altered the resonance conditions to disfavour the scattering off the LO phonon. This would explain the increase in the ratio of the peak intensity of the 2LO phonon to that of the LO phonon from 4.8 to 9.6.

It was not possible to differentiate easily which of these effects was dominant and therefore the experiments that compare peak intensities were carried out with great attention paid to preserving the incident optical power thereby allowing valid comparisons to be made.

#### 4.4.4.2 Effect of Sample Temperature

The sample was examined both at 5 K and at room temperature, approximately 300 K. At 5 K the LO phonon was found to occur at 210 $cm^{-1}$ as predicted by the literature [2.3]. The LO phonon peak was found to occur at 205 $cm^{-1}$ at room temperature and the peak was much broader. The shift was due to the thermal expansion of the lattice at higher temperatures while the broadening was accounted for by the thermal energy of the lattice allowing a wider range of **q** vectors to participate in phonon scattering.

The Te modes proved to be far more interesting. Under excitation with 5145 Å

light the Te modes were clearly visible when the sample was at room temperature, see *Figure 4.31a*. When the sample was cooled to 5 K the Te modes could not be seen as is shown in *Figure 4.31b*. The excitation was then changed to the 5286 Å line and at 5 K the Te modes were once again visible, see *Figure 4.31c*, although the LO phonon is relatively much brighter in this case.

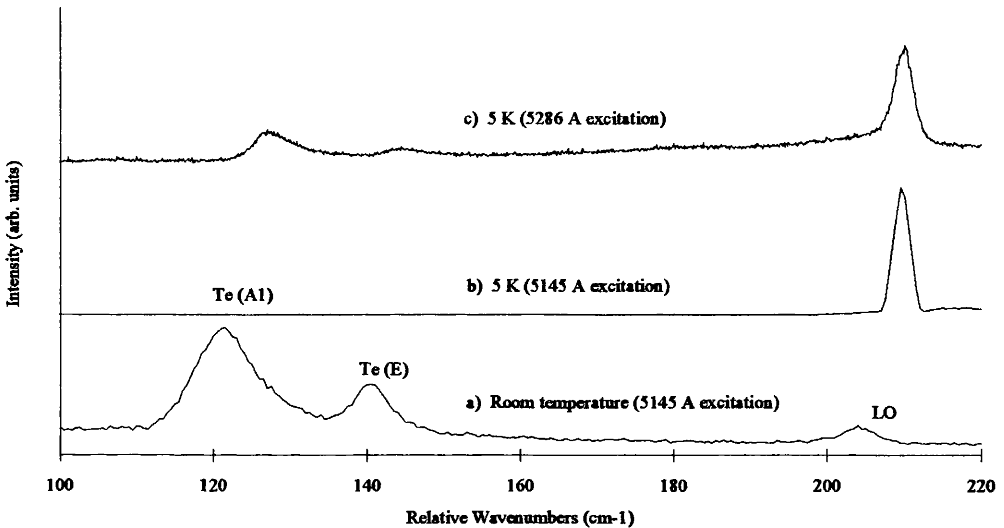


*Figure 4.31* Effect of varying the sample temperature on the Raman spectrum from an array of etched wires. NBS. 30 mW at cryostat. 2 $cm^{-1}$ resolution. Unpolarised. Spectra have been normalised.

This phenomenon cannot be explained at present. It is suspected to be due to a change in resonance conditions with the Te though this is confounded by the reappearance of the Te modes under 5286 Å excitation. It should be borne in mind that Halsall et al. [4.8] observed similar modes which they concluded originated from Te occlusions near the interface. The laser light here cannot be penetrating as far as the interface region however, since the modes are not visible away from the patterned areas, see *Figure 4.24*.

Excitation with the 4880 Å line greatly simplified matters because it lies to a much shorter wavelength than the photoluminescence thereby avoiding major resonance effects.

The penetration depth is less than for 5145 Å light and so it was possible to investigate the material nearer to the surface and so away from the interface region. The 4880 Å line also makes available more optical power than any other line available from the argon ion laser. By using this line consistently the samples may be compared easily.

### 4.4.5 Effect of Polarisation

In order to assess the effects of the wires and their orientation spectroscopically, experiments utilising polarisation were carried out. The polarisation ensured that the spectra could be compared in the knowledge that factors outside the Raman experiment were not influencing the results. The wires were printed so that they ran parallel to one of the cleaved edges. Zincblende crystals are known to cleave in the (110) and (1-10) directions hence the crystallographic direction of the wires was known.

It is the relative polarisations of the incident and scattered light that are important in Raman scattering experiments. We see that in the near back scattering orientations discussed the scattering intensity is at a maximum when the spectra are polarised and at a minimum when the spectra are depolarised, as predicted by the equations below. This can be seen in *Figure 4.32*. It should be noted that it was the spectral response of the spectrometer's gratings which dictated the orientation of all other elements in the experiment. The light, in order to optimise the response of the spectrometer gratings, after passing through the analyser must be parallel to the grooves of the grating, see *Figure 3.3*. This in turn dictated the sample orientation and the orientation of the polariser to allow a desired combination of relative orientations to be obtained. If this had not been done the spectra would not have been comparable unless the spectra were divided by the grating response for that particular orientation.

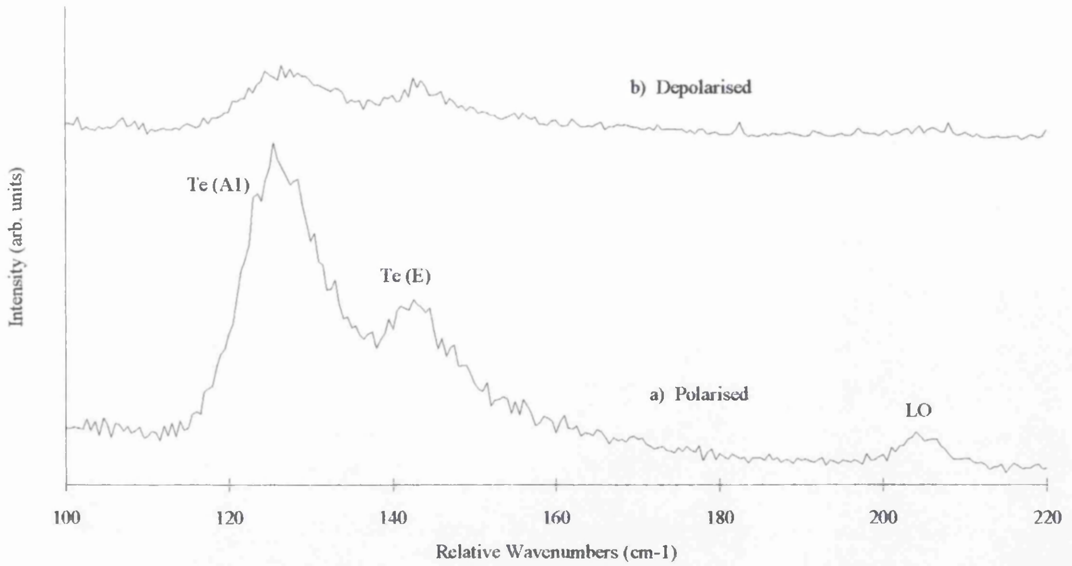


*Figure 4.32* Effect of varying the polarisation on the Raman spectrum from an array of etched wires. NBS. Samples were at room temperature. 4880 Å excitation. 40 mW at sample. 1.5 $cm^{-1}$ resolution.

If we consider only parallel polarisation the Fröhlich interaction gives:

$$\begin{pmatrix} 1 & 1 & 0 \end{pmatrix} \begin{pmatrix} a_F & 0 & 0 \\ 0 & a_F & 0 \\ 0 & 0 & a_F \end{pmatrix} \begin{pmatrix} 1 \\ 1 \\ 0 \end{pmatrix} = 2a_F \qquad \textbf{(4-1)}$$

and the deformation potential gives:

$$\begin{pmatrix} 1 & 1 & 0 \end{pmatrix} \begin{pmatrix} 0 & a_{DP} & 0 \\ a_{DP} & 0 & 0 \\ 0 & 0 & 0 \end{pmatrix} \begin{pmatrix} 1 \\ 1 \\ 0 \end{pmatrix} = 2a_{DP} \qquad \textbf{(4-2)}$$

Thus both interactions are allowed.

For perpendicular polarisation the Fröhlich interaction gives:

$$\begin{pmatrix} -1 & 1 & 0 \end{pmatrix} \begin{pmatrix} a_F & 0 & 0 \\ 0 & a_F & 0 \\ 0 & 0 & a_F \end{pmatrix} \begin{pmatrix} 1 \\ 1 \\ 0 \end{pmatrix} = 0 \qquad \textbf{(4-3)}$$

and the deformation potential gives:

$$\begin{pmatrix} -1 & 1 & 0 \end{pmatrix} \begin{pmatrix} 0 & a_{DP} & 0 \\ a_{DP} & 0 & 0 \\ 0 & 0 & 0 \end{pmatrix} \begin{pmatrix} 1 \\ 1 \\ 0 \end{pmatrix} = 0 \qquad \textbf{(4-4)}$$

thus neither interaction is allowed.

### 4.4.6 Scattering from a Patterned Area Versus an Off-Pattern Area

We see from *Equations 4-1, 4-2, 4-3, 4-4* above that changing the orientation of the sample by 90° does not influence the resulting phonon scattered light in this case. This phenomenon occurs due to crystallographic symmetry. This is shown in *Figure 4.33* in which both spectra were obtained away from the patterned wires to avoid any ambiguity arising from the structures; the spectra are identical despite the sample having being rotated through 90° between the scans. It should also be noticed from the equations that both the Fröhlich and deformation potential interactions behave in the same manner under this particular change in orientation.

### 4.4.7 Effect of Wire Orientation

If we now examine the patterned area we clearly see the 1LO phonon at 205 $cm^{-1}$ together with the appearance of the Te A1 and E modes at 125 $cm^{-1}$ and 142 $cm^{-1}$. When the wires were parallel to the *x*-direction the ratio of the Te A1 mode:Te E mode:LO phonon was 5:2.5:1, this is shown in *Figure 4.34b*.

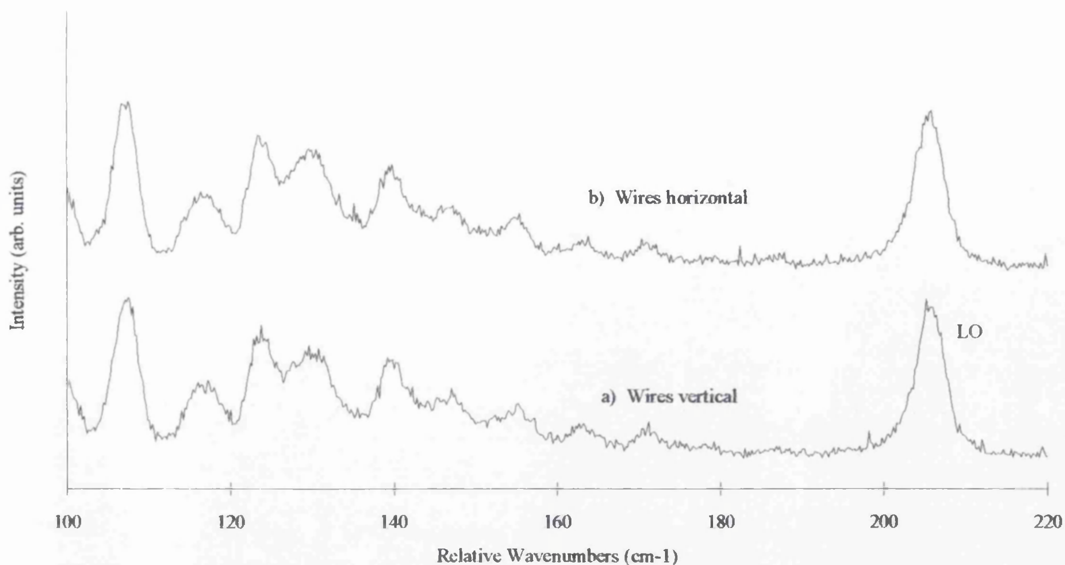


*Figure 4.33* Effect of varying the sample orientation on the Raman spectrum from a flat etched area. NBS. Samples were at room temperature. 4880 Å excitation. 40 mW at sample. 1.5 $cm^{-1}$ resolution. Polarised.

The wires were then rotated through 90° so they were parallel to the *y*-direction, keeping all other factors constant. The spectrum was however quite different to that with the wires parallel to the *x*-direction, which is shown in *Figure 4.34a*. We see the Te A1 and E modes are stronger than the LO phonon, the intensity of which we may assume to be the same as in *Figure 4.34b*, as was proved by the off-pattern spectra in *Figure 4.33* and the above equations. The ratio of the Te A1 mode:Te E mode:LO phonon is now 15:7.5:1. It should be noted that the ratio of the Te A1 mode:Te E mode remains fixed at 2:1 for both orientations indicative of a common relationship in their origins.

The difference in the ratios between the Te peaks and the LO phonon can be explained as being due to the sidewalls of the wires coupling more efficiently to the electromagnetic field of the laser light when they were parallel to the *y*-direction. However, when the wires ran parallel to the *x*-direction the light was unable to impinge on

the sidewalls to the same extent. This indicates there to be a degree of preferential lateral etching which favours removal of Zn from the side wall leaving Te behind. This process did not manifest itself away from the pattern because in the relatively large open areas the ionic bombardment component of the etch helped to remove the Te leaving a balanced stoichiometry. The absence of a balanced stoichiometry in the sidewalls also accounts for the absence of any surface modes as it would prove impossible for them to propagate if the surface was not continuously smooth.

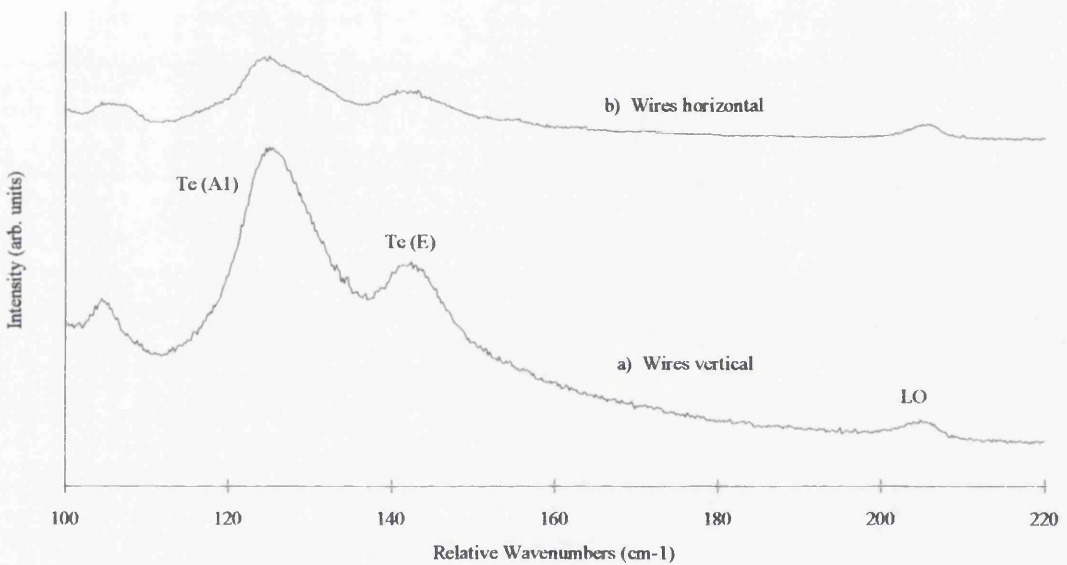


*Figure 4.34* Effect of varying the orientation of the wires on the Raman spectrum from an array of etched wires. NBS. Samples were at room temperature. 4880 Å excitation. 40 mW at sample. 1.5 $cm^{-1}$ resolution. Polarised.

### 4.4.8 Comparison of the LO and 2LO Phonon Peak Intensities

It has been suggested by Wagner et al. [3.41] that a possible quantifiable method of assessing the damage in crystalline semiconductors would be to compare the peak intensity of the 2LO phonon with that of the LO phonon. The 2LO phonon is more sensitive to

damage than the LO phonon due to its band-gap resonance being narrower and also its resonant scattering efficiency being much greater than that of the LO phonon. Crystalline damage will shift and broaden the band-gap thereby changing the resonance conditions, this has a relatively greater effect on the 2LO phonon intensity than the LO phonon intensity. It is therefore possible to make a comparison between two different areas and a larger number obtained for the ratio of the 2LO phonon intensity to the LO phonon intensity is indicative of less crystalline damage.

Spectra were recorded at 5 K using the 5145 Å line both on- and off-pattern, the spectra are shown in *Figure 4.35*. The ratio of the peak intensity of the 2LO to the peak intensity of the LO was easily calculated to be 2.80 in the case of the wires and 3.75 in the case of off-pattern. This indicates there to be more damage to the lattice at the site of the wires compared to the flat areas away from the wires. These results however raise questions because of the PL background. The spectra were recorded with the only intended difference being the site which was illuminated. The difference in the background PL intensity could be due to the etch, a slight difference in alignment, the sample temperature or a grating effect. The first two suggestions are unlikely due to the fact the signals are of similar intensities, also there is a change in the relative intensities of the PL emissions, and the PL emission does not shift in wavelength. Any grating coupling effect would be minimal at such a steep angle of incidence. The PL of the etched samples is considered in greater detail elsewhere, see *Section 4.4.9*. The difference in PL background however, infers there to be a difference in resonance conditions. Another possibility was that the reduced dimensions of the wires confines the exciton and the resulting blue shift in the emission was responsible for altering the resonance conditions to favour scattering off the LO phonon [4.9]. The fact that the dimensions of the wires are large compared to the Bohr radius of the exciton, approximately 4 nm [3.20], means the excitons are unlikely to be confined.

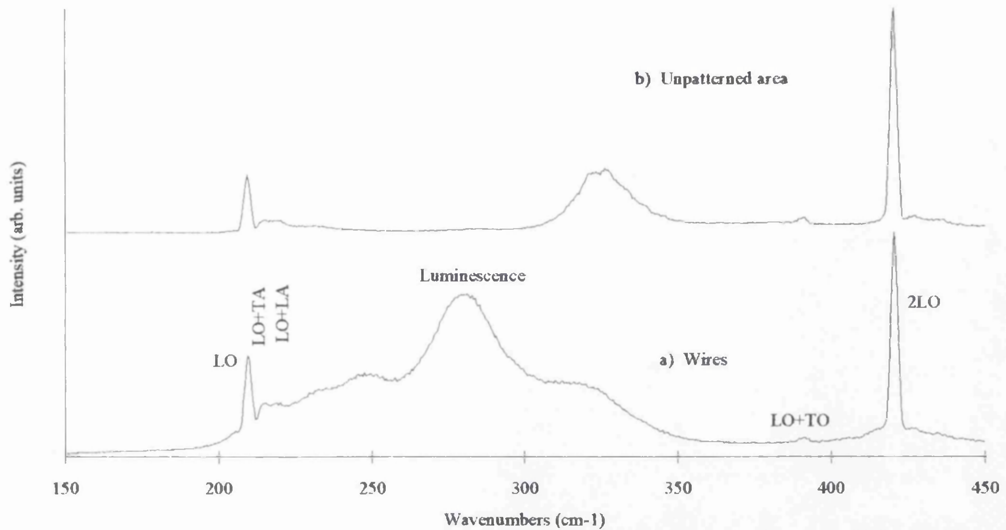


*Figure 4.35* Raman spectra recorded at 5 K showing a reduction in the ratio of the peak intensity of the 2LO phonon to that of the LO phonon when moving from an unpatterned etched area to a patterned etched area. NBS. 5145 Å excitation. 100 mW at cryostat. 2 $cm^{-1}$ resolution. The spectra are polarised and have been normalised.

### 4.4.9 Photoluminescence of Wires

The sample was examined at 5 K using the 4880 Å line of the $Ar^+$-ion laser. The laser was focused to a spot on the wire arrays, this was confirmed using the CCD camera which enabled precise monitoring of the laser beam position on the sample. The spectrum obtained is given in *Figure 4.36a*. The sample was then moved so that the spot was focused onto an area subjected to the etch but not patterned, the resulting spectrum is given in *Figure 4.36b*.

The peaks were easily identified from the literature [4.1] and are given in *Table 4.5*.

The splitting of the free exciton remains constant at 5 meV. The splitting is caused by the strain in the lattice originating from the interface with the GaAs substrate which has

a different lattice constant to that of ZnTe. Since the splitting remains constant for on- and off-pattern it is deduced the strain must be the same in both cases.

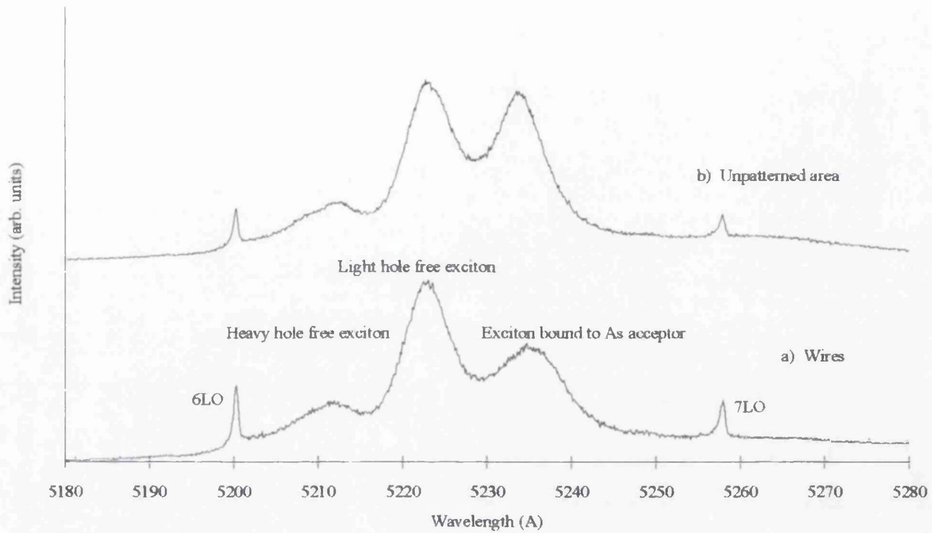


*Figure 4.36* Low temperature (5K) near band edge photoluminescence spectra obtained from wires and an unpatterned area of the same sample of ZnTe. NBS. 4880 Å excitation. 60 mW at sample. 0.25 Å resolution. Spectra have been normalised.

| **Energy (eV)** | **Position (Å)** | **Assignment** |
|---|---|---|
| 2.384 | 5200 | 6LO phonon |
| 2.379 | 5212 | Heavy hole free exciton |
| 2.374 | 5223 | Light hole free exciton |
| 2.369 | 5234 | Exciton bound to an arsenic acceptor |
| 2.358 | 5258 | 7LO phonon |

*Table 4.5* Positions and assignments of peaks occurring in the low temperature photoluminescence spectrum of reactive ion etched ZnTe.

The intensity of the emission from the wires is slightly less than that from the flat etched surface, using the phonon lines as intensity references. This was possibly a sign of

damage but it proves impossible to guarantee the phonon's intensity does not vary.

It should be noted that there were no wavelength shifts for any of the peaks concerned. However, there was a change in relative photoluminescence intensities between the free excitons and the exciton bound to the As acceptor. The ratio of the split free exciton lines remained constant both on and off-pattern which suggested the intensity of the bound exciton had increased going from the wires to the flat etched area. This increase in the emission from the exciton bound to an As acceptor was likely to arise from the removal of material by etching the off-pattern area allowing light to penetrate nearer to the interface where the As concentration had increased because of diffusion of As from the GaAs substrate during the growth process.

## 4.5 Cylinders Fabricated in Zinc Telluride

### 4.5.1 Fabrication of Cylinders

This work carries a great deal of importance because it will allow the fabrication of structures reduced in yet another dimension compared to the wire work. With the impending advent of quality heterostructures in II-VI semiconductors the fabrication of zero dimensional confinement becomes plausible. The lack of reasonably good quality heterostructures during this project meant any sort of investigation into zero dimensional confinement was impossible. Taking this limitation into account an assessment of the quality of the etch, regarding reducing damage to the lattice, was carried out. Cylinders were etched into the ZnTe using a technique similar to that used for the wires.

The sample was fabricated by Dr. K. Tsutsui using a similar technique to that given for the fabrication of the wires. The resist used was a bilayer of PMMA consisting of 4%

BDH spun directly onto the ZnTe, *sample ZT95*, with a layer of 2.5% ELV spun on top. The Leica EBPG5 beamwriter was used to manufacture the pattern. The electron beam was focused to a spot which was then switched on and off as the sample was scanned, (rather than being allowed to hit the sample continuously during each pass, as was the case for the wires). On development of the resist in MiBK the sample then had a 30 nm thick Ti mask evaporated onto it. The lift-off was achieved using warm acetone.

*Figure 4.37* SEM micrograph showing an angled view of a 50 nm diameter dot.

The etching was carried out in an *Electrotech SRS Plasmafab 340* RIE machine. The standard 1:8 mixture of $CH_4$:$H_2$ was used with 5 sccm of methane. The pressure was 20 mTorr and the RF power was 150 W. After a six minute etch the cylinders were 300 nm tall and 60 nm in diameter. A 50 nm diameter dot, representative of the ones making up the array examined, is shown in *Figure 4.37*.

### 4.5.2 Raman Spectroscopy of Cylinders

Initially the sample was investigated at room temperature using 4880 Å light in the NBS configuration. As can be seen from *Figure 4.38* the spectra was similar to that obtained from the wires. The LO phonon was present at 204 $cm^{-1}$, together with the Te A1 and E modes at 123 $cm^{-1}$ and 140 $cm^{-1}$ respectively.

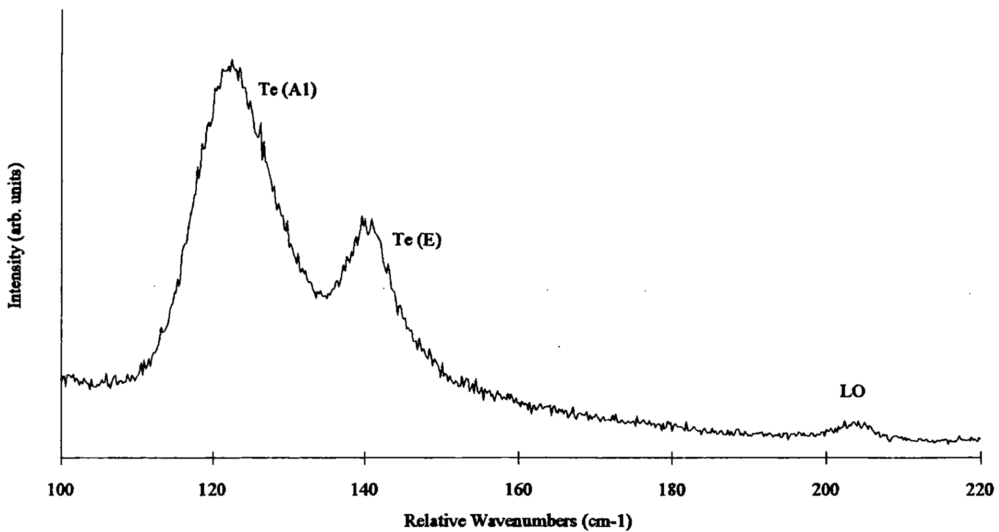


*Figure 4.38* Room temperature Raman scattering from ZnTe dots. NBS. 4880 Å excitation. 70 mW at sample. 3 $cm^{-1}$ resolution. Unpolarised.

The sample was then cooled to 5 K and the experiment repeated using the 5145 Å line to illuminate the sample, the resulting spectrum is shown in *Figure 4.39a*. Again we see the LO phonon, this time at 210 $cm^{-1}$ due to the lower temperature. We also have the

combinational modes at 207 $cm^{-1}$, 215 $cm^{-1}$ and 218 $cm^{-1}$ due to scattering from LO-TA, LO+TA and LO+LA respectively. Another combinational mode was visible at 392 $cm^{-1}$ which was due to a summation of the LO+TO phonons. The resonance conditions emphasised scattering off the 2LO phonon which occurred at 421 $cm^{-1}$. The ratio of the peak intensity of the 2LO phonon to that of the LO phonon was calculated to be 1.72.

The area of illumination was then changed away from the patterned cylinders to an area subjected simply to a flat etch. The spectrum obtained, which is shown in *Figure 4.39b*, did not reveal any new peaks but the ratio of the 2LO to LO phonons had increased to 1.8 indicating there to be more damage at the site of the cylinders.

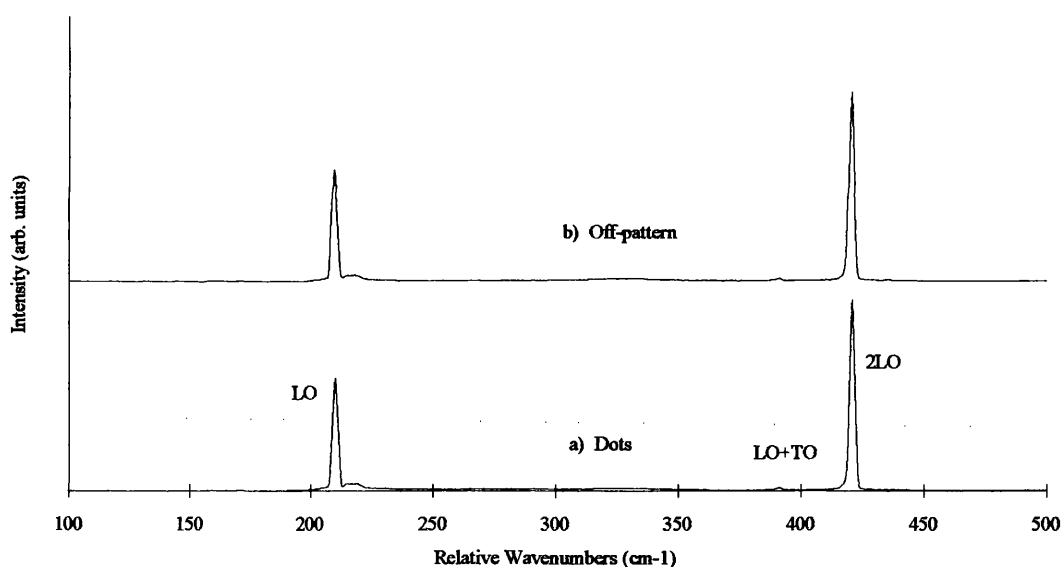


*Figure 4.39* Comparison of Raman scattering from dots and a flat-etched area of ZnTe. NBS. 5 K. 5145 Å excitation. 20 mW at cryostat. 2 $cm^{-1}$ resolution. Unpolarised. Spectra have been normalised.

The laser line was then changed to 5286 Å and the sample re-examined. At the site of the cylinders the Te A1 and E modes appeared but were weak compared to the LO phonon, see *Figure 4.40a*. The ratio of the 2LO to LO phonon was calculated to be 0.1.

Also of interest was the very weak TO phonon at 181 cm$^{-1}$ which had not been observed before. Moving away from the patterned areas allowed the spectrum given in *Figure 4.40b* to be recorded. Here the Te A1 and E modes have almost disappeared, there was no sign of the TO phonon and the ratio of the 2LO to LO phonon was 0.1. The presence of the TO phonon can be explained by the light being able to access new crystallographic directions due to the cylinders having been etched and the sidewalls being exposed. This argument gains more support from the disappearance of the TO phonon when the flat etched area was examined. The disappearance of the Te modes supports the argument concerning selective etching of the Zn with respect to the Te. This argument gains more credibility since all other aspects of the experiment are analogous to the work carried out by Watt et al. [3.44] who witnessed the propagation of surface phonons on similar cylinders fabricated in GaAs. The surface phonons scattered light to frequencies that lay between those of the LO and TO phonon frequencies. No such scattering was observed indicative of a change in the stoichiometry at the surface of the etched cylinders.

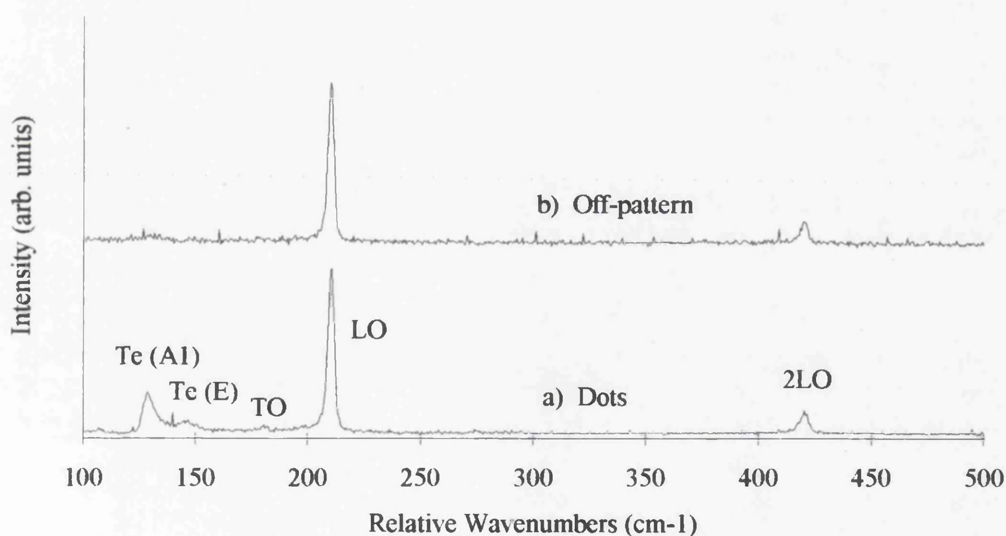


*Figure 4.40* Comparison of Raman scattering from dots and a flat-etched area of ZnTe at 5 K. NBS. 5286 Å excitation. 40 mW at cryostat. 2.5 cm$^{-1}$ resolution. Unpolarised. Spectra have been normalised.

# Chapter 5

# Discussion of Results

## 5.1 Importance of Starting Material

In the preceding chapter the results obtained from the samples received were given. The material was characterised before and after reactive ion etching using the techniques of photoluminescence and Raman spectroscopy.

There is a large amount of physics to be researched once the growth area has improved sufficiently. The topic of confined phonons holds great interest but requires the availability of good quality superlattices with sharp, accurately defined interfaces with regards to doping and composition. A major goal therefore must be to become sufficiently expert in the manufacturing of interfaces. The lack of phonon confinement points towards poor quality interfaces. This is probably due to interdiffusion of the layers smearing out the contrasting dielectric constants of the heterojunction. Evidence of poor interfaces is given in *Figures A1, A2* and *A5,* where there is little or no fine structure visible. This problem needs to be addressed as it may be crucial to the performance of future device.

The strain from the interface could well become a problem in the future and it would be advantageous to dictate the strain required to tailor the performance of a device, such as a laser. It is a subtle but nevertheless important difference when the strain dictates the performance of the device and the requirements of the device have to be compromised.

Again there is little room for manoeuvre on the grower's part since, taking ZnTe as an example, the choice of a nearly lattice matched substrate, such as GaSb, is prohibited by the cost. All samples from Universität Regensburg therefore were grown on GaAs with a lattice mismatch of approximately 7% which inevitably led to strained samples which can be seen in the splitting of the free exciton in *Figure 4.13*. There are, of course no commercially available ZnTe substrates. It should be noted ZnSe has an advantage because its lattice constant of 5.668 Å almost matches that of GaAs at 5.653 Å leading to a slight mismatch of 0.26% at room temperature.

The problems of obtaining good crystallinity near the interface with the substrate, the diffusion of impurities from the substrate and the presence of strain due to lattice mismatch, can be prevented by incorporating a thick buffer layer or superlattice into the structure. This could be a major inconvenience from an etching point of view as it means, if the layers have to be etched through to the substrate for reasons of isolation, the sample will need to be exposed to the plasma for longer thereby increasing the possibility of damage. Also, because of the set anisotropy factor, the lateral dimensions of any structures must be large enough to ensure the profile of the etched feature does not suffer. For example if we take the case of quantum wires, if the etch begins to undercut, the wire cannot be very tall or it will be liable to collapse, see *Figure 4.26*.

The equipment and personnel assembled at Glasgow would allow the production and characterisation of optical devices such as lasers. This calls for reasonably accurate control of doping, something which is not too far in the future judging by the numerous recent reports of luminescence and lasing from II-VI materials. The possibility of fabricating surface emitting lasers at Glasgow is very attractive since there are no other reports of an etching technique to rival the anisotropy factor exhibited by the $CH_4/H_2$ etch developed at Glasgow which opens up the possibility of etching thick layers and layers of different materials i.e. a superlattice or dielectric mirror.

The ability to dope II-VIs to high concentrations, $>10^{18}$ cm$^{-3}$, would allow the investigation of plasmons. The fabrication of a grating on the surface of the sample would allow the light to couple more efficiently to the plasmons [5.1. 5.2, 5.3, 5.4].

## 5.2 Effects of Dry Etching

The etched samples of ZnSe described in the previous chapter show some similarities to the etched ZnTe samples. First let us consider each separately and then make comparisons.

The etched ZnSe, *ZS129*, showed a decrease in the DAP luminescence at 5300 Å, relative to the near band edge luminescence. The decrease was concurrent with the decrease in the ratio of $CH_4$:$H_2$, indeed the photoluminescence spectrum of the sample etched in the 1:4 ratio resembles that of the control sample. The same effect, decreasing DAP emission at 2.305 eV with increasing hydrogen, can be seen in the ZnTe samples. In the ZnTe samples this also coincides with the decrease in the arsenic acceptor at 2.368 eV leading to the conclusion the DAP, in ZnTe, concerns an arsenic acceptor and an unidentified donor.

The similarities between the two materials leads to the conclusion the decrease in the DAP emission is connected with the methane to hydrogen ratio. The decrease in the proportion of hydrogen could have led to a more aggressive etch thereby creating damage. However, this is unlikely given the small atomic mass of hydrogen, in addition there is no evidence of damage in the Raman spectrum of either. The decrease in DAP emission is more likely to be an indication of a passivation mechanism whereby the hydrogen is breaking the link between the DAP by neutralising either the donor or the acceptor. In ZnTe the suppression of the emission from excitons bound to the arsenic acceptor leads to

the hypothesis that hydrogen is passivating the acceptor. The possibility of the hydrogen also passivating the donor cannot be ruled out, however, there is no direct evidence from this work to support any conclusions on this hypothesis.

After annealing at 200°C in pure argon for 5 minutes the DAP luminescence has recovered for ZnTe and especially well for ZnSe and the spectra obtained from both sets of samples resemble their respective controls. The arsenic acceptor in ZnTe has also recovered to resemble the control spectrum. This can be explained by the partial desorption of the passivating hydrogen, by the increase in thermal energy, leading to the reactivation of the acceptor.

One important phenomenon is the increase, after annealing, of the luminescence from the zinc vacancies at 2.780 eV in the unetched ZnSe samples. The other peaks appearing at lower energies are easily identified as the LO phonon replicas of the $V_{Zn}$ emission because of their regular separation which coincides with the LO phonon energy, 31 meV. This phenomenon is not seen in the etched samples. There is at present no explanation for this, although there is a possibility that the zinc is not securely positioned in the lattice and is easily removed, either by annealing or by it being etched preferentially with regard to the group VI element.

The preferential etching argument also holds for the ZnTe case where a broad feature of 61 meV occurs at 2.23 eV after etching, it does not appear after simple annealing. This emission is assigned, after comparison with the spectra obtained by Wilson et al. [4.6], to a zinc-vacancy-impurity complex. After annealing, this complex develops finer structure which suggests the annealing has removed some etch induced damage.

Sotomayor Torres et al. [1.4], using XPS, observed a Te rich surface after etching ZnTe and a Se rich surface after etching ZnSe. This again adds more weight to the idea of

preferential etching of the group II element by $CH_4/H_2$.

The etching of nanostructures in ZnTe led to the appearance of Te A1 and E modes in the Raman spectrum shown in *Figure 4.24a*. These peaks were much more obvious on the arrays of wires than on the flat etched areas. The effect of polarisation orientation was investigated and the modes were found to be brighter under parallel polarisation, see *Figure 4.32a*. This then allowed the orientation of the sample to be ruled out as a possible cause of the modes intensity behaviour, see *Figure 4.33*. The remaining possibility to be investigated was the orientation of the wires themselves, which is detailed in *Figure 4.34*. The Te modes were more evident when the sample was oriented such that the axes of the wires were vertical, i.e. running parallel to the $x$-direction. In the near back scattering orientation used, the laser made an angle of 5° to the $z$-axis in the $yz$-plane. This meant the sidewalls of the wires were illuminated more in this orientation than when the wires were turned through 90° so their axes ran parallel to the $y$-direction. This leads to the conclusion that there must be a far greater proportion of Te present at the sidewalls than at the sites of the flat etched areas. This could arise if the chemical component of the etch, rather than the physical ion bombardment component, was more reactive with the Zn than it was with the Te. The chemical component of the etch is less anisotropic than the ion bombardment component and so it is quite feasible the chemical component should have an important effect on the sidewalls. Again the deduction must be that there is a tendency for the etch to remove the Zn rather than the Te. The Te is probably still quite reactive and its removal will be assisted, for the flat etched areas especially, by the physical bombardment of the ions. Indeed the following simple argument can be put forward. Due to the cubic lattice structure of ZnTe, the removal of a Zn atom from the flat etched surfaces uncovers a Te atom which must be removed before the next Zn atom is revealed. This would explain why the flat etched areas show little sign of Te enrichment in Raman scattering and XPS experiments.

There is also a possibility the Te is deposited on the sidewall and then acts as a protective coating for the sidewalls, enabling the etch to attain a high anisotropy factor by reducing the horizontal etch rate. The triangular shape of the wire cross-section is characteristic of the deposition of a protective coating on the sidewall. This may also be a sign the Ti mask is being eroded and the structure is therefore narrower at the top, though there is no evidence of CD loss from the SEM measurements to support this.

The change in the stoichiometry, whereby there is an increase in the Te:Zn ratio at the sidewalls of the wires, would also explain the failure to observe confined and interface phonons within the structures. The absence of a continuous and regular ZnTe lattice would prohibit the propagation of the phonons, especially at the surface of the structures. Although this is a drawback for this material it should be possible to etch wires into superlattices and observe the effects of confinement in that system. Since there is no evidence of damage within the nanostructures themselves, a confined phonon should be able to propagate along a wire with good confinement in the vertical direction, caused by the heterojunction, and some degree of confinement in the horizontal direction brought about by the etch.

There was no sign in any of the Raman data of an asymmetric broadening of the LO phonon to lower energies as was predicted by Rama Rao and Sundaram [3.40] and we can conclude there was no sign of crystalline damage using this technique. The technique did pick up the presence of TO phonons in the samples etched with dots when the dots were illuminated with 5286 Å light. This can be explained by the light being able to gain access to other crystallographic directions, such as the (100) and (010) directions, via the side of the cylinders. For these directions the TO phonon is no longer forbidden and hence appears in the spectra. It is not known why the TO phonon is not be visible under excitation with 5145 Å light but it is suspected to be due to some resonance phenomenon.

# Chapter 6

# Conclusions and Future Work

## 6.1 Summary of Work Presented in this Thesis

The photoluminescence spectroscopy of the ZnSe samples prior to etching revealed emission from the free exciton at 4424 Å. There was also emission indicating the presence of a neutral bound donor at 4438 Å, zinc vacancies at 4460 Å, extended dislocations at 4760 Å and a donor-acceptor pair at 5301 Å. These transitions have been reported previously and the energies at which they occur in these samples are in good agreement with those reported in the literature.

Following dry etching there was a large increase in the DAP emission relative to the near band edge emission. This increase was found to be inversely proportional to the proportion of hydrogen in the etch gas. At a ratio of 1:4 of $CH_4$:$H_2$ the DAP emission was similar to that from the control sample. There was also a new feature at 4700 Å but this was not identified.

After annealing at 200°C for five minutes in Ar the DAP emission was found to have increased relative to the near band edge emission. In the second batch of samples etched with a higher proportion of hydrogen in the etch gas, there was DAP emission which could be identified from the literature as involving Ga which probably originated from the GaAs substrate. The most interesting feature in the near band edge emission is

the emission due to zinc vacancies which became more intense than that of the higher energy emission possibly indicating the zinc was not securely bound in the lattice. This effect was not observed after the samples had been etched.

The ZnSe sample etched with a $CH_4$:$H_2$ ratio of 1:8 gave a spectrum most similar to that of the unetched control sample and also the most anisotropic etching conditions when assessed using SEM. This ratio was therefore considered to be the most appropriate for etching nanostructures.

The room temperature Raman scattering experiment carried out upon the as-grown and etched ZnSe did not reveal any differences between the control sample and the etched samples. There was no scattering from the TO phonon and there was no asymmetric broadening of the peak related to scattering from the LO phonon. The ratio of the peak related to scattering from the 2LO phonon to that of the one related to scattering from the LO phonon was found to be invariant. It was concluded from this there was no sign of crystalline damage evident from the experiment.

The photoluminescence examination of the as-grown ZnTe revealed emission from the free exciton which was split into two peaks due to strain arising from the lattice mismatch with the substrate. There was also evidence of emission from an exciton bound to an arsenic acceptor which was found to decrease after etching with $CH_4/H_2$, this reduction was found to be more severe as the amount of hydrogen in the etch gas was increased. The emission from this peak was found to recover in intensity after annealing at 250°C for fifteen minutes in nitrogen, although it was shifted higher in energy by 2 meV. Emission from a DAP at 5379 Å follows a similar trend to the exciton bound to the As acceptor after etching. Assuming the donor ionisation to be 18 meV, this would indicate the acceptor involved was As. The behaviour of these two peaks, together with other reports of decreasing photoluminescence emission from *p*-type semiconductors after

exposure to hydrogen led to the conclusion hydrogen was passivating the arsenic acceptor. The annealing serves to drive out the hydrogen and allows the emission intensity to recover.

Annealing was found to reduce the FWHM of the emission assigned to Zn vacancies at 5560 Å from 61 meV to 20 meV. The resemblance of the peak to those reported in the literature confirmed the assignment. The reduction in the FWHM was due to a reduction in the range of energies involved in the Zn-vacancy complex after annealing.

The prediction of the resonance in the Raman scattering efficiency was confirmed by varying the position of the energy gap with respect to the energy of the incident photons by varying the sample temperature. This also served to confirm the brightest signal from the LO phonon with the sample at 5 K, was obtained when using 5145 Å excitation.

There were no signs of crystalline damage evident from the Raman scattering experiment after reactive ion etching ZnTe with $CH_4/H_2$. There was however a decrease in the intensity of the combinational modes but this was not found to occur when a thicker sample was etched with a similar recipe. This led to the conclusion the poor crystalline quality of the sample near the interface inhibited the propagation of the combinational modes.

Wires of 20 nm width were successfully fabricated in ZnTe. Upon examination of the etched samples using Raman scattering, signals corresponding to scattering by the following phonons and combinational modes were observed. The modes identified from the literature were the LO, LO+TO, 2LO and 3LO phonons. The LO phonon peak did not broaden asymmetrically to lower energies and there was no evidence of scattering from the TO phonon. The ratio of the 2LO phonon intensity to that of the LO phonon was found to

be 3.75 away from the patterned area and 2.80 at the patterned area. This decrease was deduced to arise from the change in resonance conditions due to a shift in the energy gap brought about by crystalline damage. This alteration in the resonance conditions was known to effect the 2LO phonon more than the LO phonon due to the 2LO phonon having a much narrower resonance.

Differences in the spectra obtained by changing the excitation frequency and incident power proved inconclusive since it was impossible to separate the effect of altering one parameter from others, which in turn effected the resonance conditions. Altering the excitation frequency altered the respective LO and 2LO resonance conditions, but did allow the origin of peaks to be confirmed since after changing the excitation frequency, the peaks which were energy invariant had to arise from Raman scattering whereas those which were wavelength invariant had to arise from photoluminescence. Altering the incident power of the excitation also altered the sample temperature and hence its bandgap and subsequently the resonance conditions. Increasing the sample temperature directly led to a shift to lower energies of the LO phonon accompanied by a broadening of the peak. The shift was deduced to arise from an expansion of the crystal reducing the frequency of vibration while the broadening was concluded to arise because the thermal energy of the lattice allowed a wider range of **q** vectors to participate in phonon scattering.

The modes visible at 122 cm$^{-1}$ and 141 cm$^{-1}$ were identified using the literature as originating from crystalline Te A1 and E modes, respectively. They were confirmed to be Raman active since they were energy invariant when the excitation energy was changed. The behaviour of the modes under temperature variation could not be understood but it was thought the behaviour was probably due to some resonance phenomenon. The Te modes were found to be most intense when illuminated with depolarised light. Comparison of spectra obtained by illuminating the pattern, and then away from the pattern, with depolarised light, led to the conclusion the Te modes were brightest at the

site of the pattern. The influence of the orientation of the sample was ruled out by rotating it through 90° and observing no change in the spectrum obtained. This then allowed the conclusion that the Te modes were brightest when the wires were parallel to the *y*-direction. From this it is concluded the Te was present on the sidewalls of the wires since their degree of illumination was consistent with the intensity of the Te modes. It should be noted the intensities of the Te modes relative to each other were constant indicating some common origin.

The above effect, together with the conclusion from the XPS work of the etching leaving a Te or Se enriched surface behind, and the presence of Zn-vacancies in the PL of both etched ZnTe and ZnSe leads to the conclusion the $CH_4/H_2$ dry etching process preferentially etches Zn. It should be borne in mind the etch may form a non-volatile Te rich compound which is deposited on the sidewalls and acts as a passivant, protecting the structures from lateral etching.

There was no conclusive indication of damage evident from the photoluminescence experiments conducted on the wire samples. There was a relative increase in the emission from the exciton bound to an arsenic acceptor. This was concluded to arise as a result of arsenic originating from the substrate, the etching reduced the distance to the interface and so the light was able to examine material nearer to the interface and this material contained a higher proportion of arsenic.

The fabrication of cylinders with diameters of 30 nm was successfully accomplished using a similar process to that detailed above for the case of the wires. The Raman spectra obtained from the cylinders were similar to those obtained from the wires. The ratio of the 2LO phonon to the LO phonon was calculated to fall from 1.75 to 1.72 as the spot was moved onto the patterned area therefore indicating there to be greater damage at the site of the pattern than away from it. Scattering from the TO phonon was observed when

5286 Å excitation was used. This arose because the light was able to gain access via the sidewalls to crystallographic directions other than the (100) direction. It was not a sign of damage and when the sample was examined away from the patterned area, but at an area subjected to a flat etch, scattering by the TO phonon could not be observed.

No phonon confinement effects were observed in any of the work, partly as a consequence of the preferential Zn etch discussed above. However, the main parameter of relevance was the interface quality and the periodicity of superlattices and quantum wells. The preferential removal of Zn could lead to an atomically rough surface which may prevent the propagation of phonons. Such a surface may also have a high abundance of dangling bonds which again may ruin the possibility of phonon propagation.

## 6.2 Future Work

It appears from the results of this thesis there is a layer of a Te containing compound laid down on the sidewalls of the wires during reactive ion etching with $CH_4/H_2$. This may well be necessary to prevent lateral etching or it may be due to a preferential etching process. Whichever of these it is due to, some form of post etch clean should be developed to facilitate the removal of this layer so that it does not interfere with the characteristics of any device which may be fabricated in this material i.e. it would reduce the reflectivity of a mirror etched by the process because the difference in refractive indices between ZnTe and Te is less than the difference between ZnTe and air.

As soon as good quality superlattices become available it must be a priority to etch wires and dots in these material systems. It should be possible to investigate the effect of confinement as was discussed in Chapter 3. By making the length of the wires progressively shorter and shorter it should be able to observe effects near the transition

from 1-D to 0-D confinement.

Micro-Raman spectroscopy could be used to investigate the effect of varying the k-vector upon the confinement in wires. This should allow the light to couple more efficiently into the wire and hence amplify any confinement effects.

There are still some as yet unidentified impurities in the photoluminescence spectra of both ZnSe and ZnTe. It would be useful to understand their origins and it is suggested a two hole transition experiment could be configured to identify the impurities.

When samples of highly doped materials, i.e. $>10^{18}$ $cm^{-3}$, are available it should be possible to fabricate a grating on the surface of the sample. The grating could be used to enhance the k-vector of a laser beam and thence allow the dispersion curve of the plasmons to be mapped as a function of wavevector.

Fabrication of light emitting devices should be possible. Starting with a simple LED structure it may be possible to utilise the existence of the exciton at room temperature in wide band-gap II-VIs to produce a relatively bright LED, the performance of which could be further enhanced by incorporating a mirror under the LED to reflect any light which would otherwise be lost in the substrate.

Once a reasonable understanding of this technology is gained it could then be extended to include the etching technology at our disposal. The fabrication then becomes feasible of ring lasers and distributed feedback (DFB) lasers. Surface emitting lasers should also be possible and the combination of an optical source with a Stark effect modulator on the same chip would be an engineering challenge well worth pursuing. By careful design of the growth structure it may be possible to produce these devices in line in the $z$-direction.

# Appendix

The Raman spectra obtained from the ZnSe/ZnS samples, *ZS371*, *ZS377* and *ZS379* are shown in *Figures A1, A2, A3* respectively. They are all very similar, having a low energy peak at ~50 $cm^{-1}$ but there was no scattering between 200 $cm^{-1}$ and 300 $cm^{-1}$ as might have been expected from ZnSe. Since there was no scattering from the ZnSe these samples were not used.

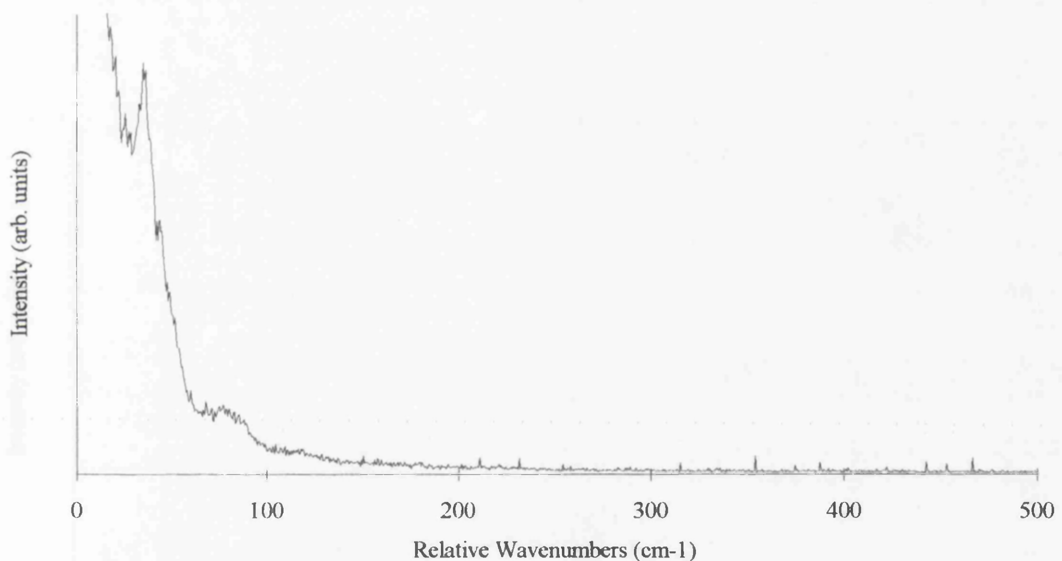


*Figure A1* Raman scattering from ZnSe/ZnS sample, *ZS371*. 5 K. 4880 Å excitation. 1 mW at cryostat. 3 $cm^{-1}$ resolution. Unpolarised.

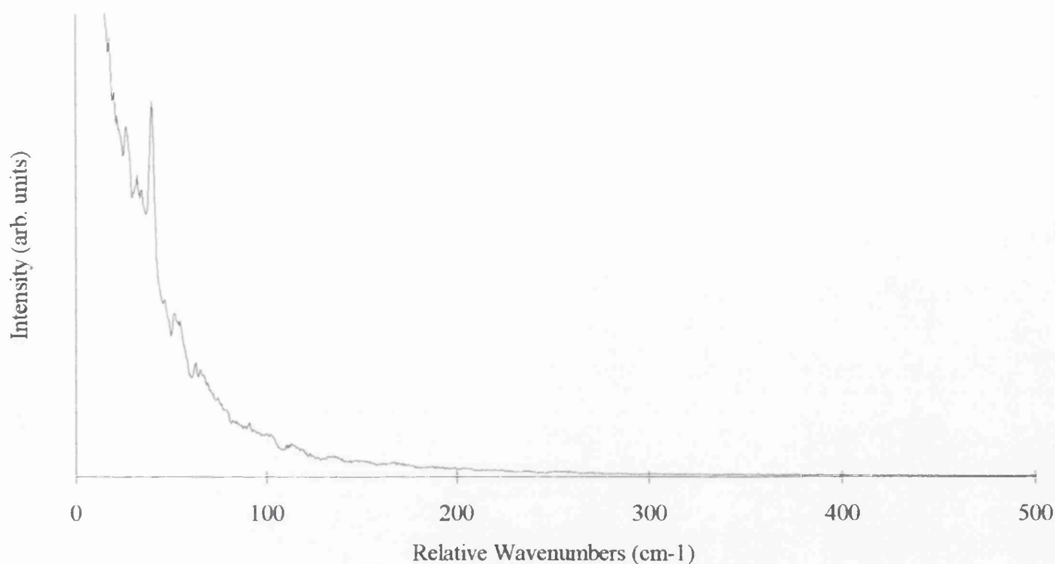


*Figure A2* Raman scattering from ZnSe/ZnS sample, *ZS377*. 5 K. 4880 Å excitation. 1 mW at cryostat. 3 $cm^{-1}$ resolution. Unpolarised.

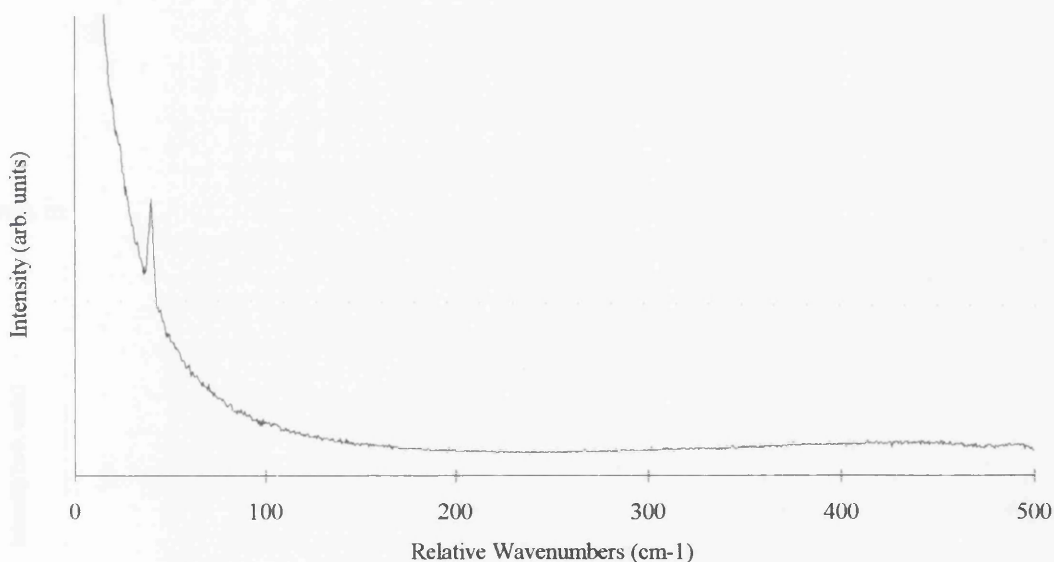


*Figure A3* Raman scattering from ZnSe/ZnS sample, *ZS379*. 5 K. 4880 Å excitation. 1 mW at cryostat. 3 $cm^{-1}$ resolution. Unpolarised.

*Figure A4* presents the Raman scattering spectrum obtained from sample *MB313*. The peak at ~250 $cm^{-1}$ is thought to originate from ZnSe, perhaps from the buffer layer,

but the scattering was very weak and changes in the peak, such as an asymmetric broadening, would have been difficult to observe.

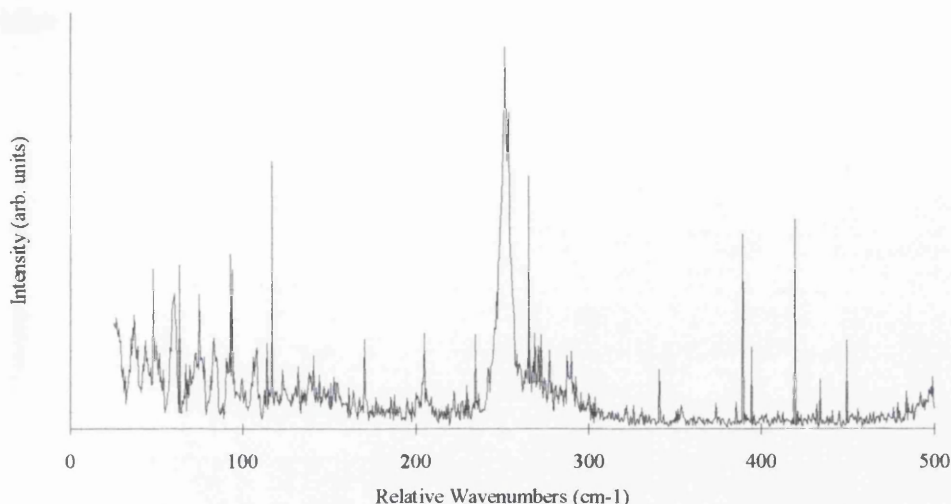


*Figure A4* Raman scattering from the ZnCdSe/ZnSe sample *MB313*. Room temperature. 4880 Å excitation. 100 mW at sample. 3 $cm^{-1}$ resolution. Unpolarised.

The Raman scattering spectrum obtained from the ZnSSe/ZnSe sample, *P26*, is given in *Figure A5*. No scattering was observed from this sample.

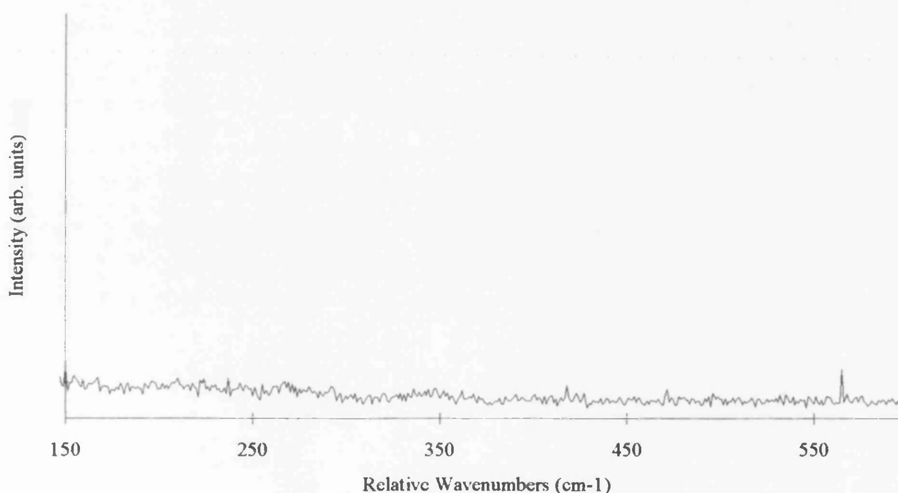


*Figure A5* Raman scattering spectrum given by sample *P26*. Room temperature. 4880 Å excitation. 70 mW at sample. 3 $cm^{-1}$ resolution. Unpolarised.

The low temperature photoluminescence spectrum obtained from the ZnSe/ZnTe sample, *Q97*, is given in *Figure A6*. Following this is the Raman scattering spectrum obtained from the same sample, see *Figure A7*.

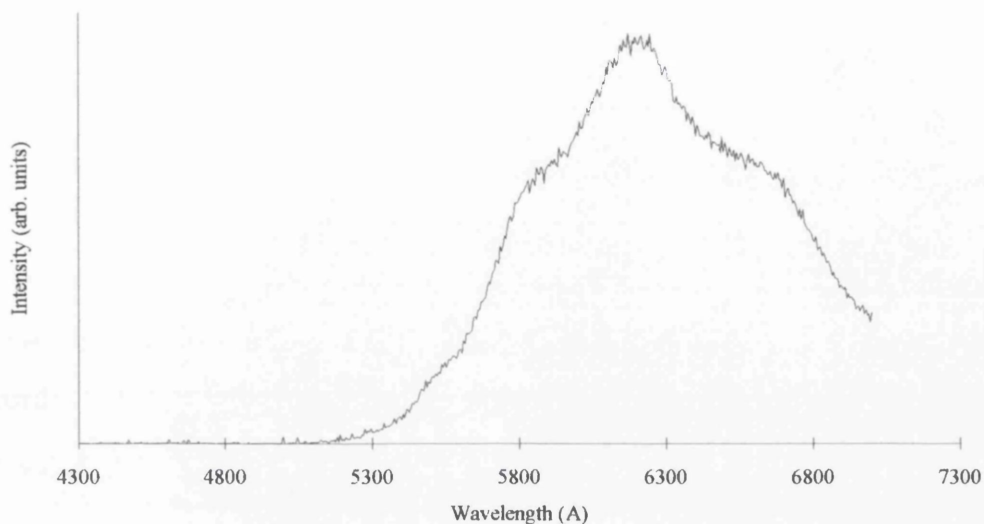


*Figure A6* Low temperature photoluminescence from the ZnSe/ZnTe sample *Q97*. 5 K. 3638 Å excitation. 90 mW at cryostat. 0.7 Å resolution.

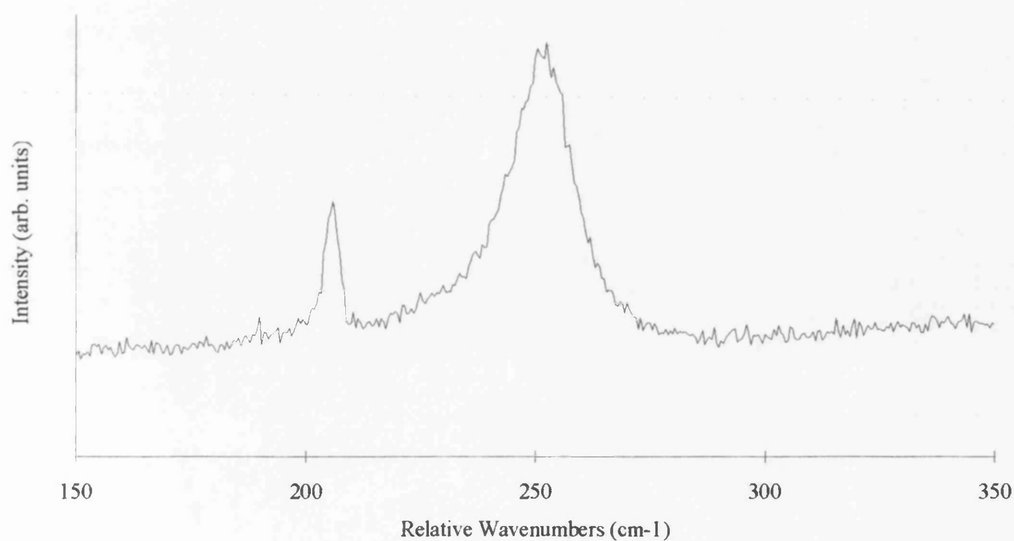


*Figure A7* Raman scattering spectrum from the ZnSe/ZnTe sample *Q97*. Room temperature. 4880 Å excitation. 70 mW at sample. 3 $cm^{-1}$ resolution.

The next four samples, *DJI22A*, *DJI28A*, *DJI30A* and *DJI31A*, consist of superlattices of ZnCdSe/ZnSe grown on GaAs substrates, as detailed in *Section 3.2*. The photoluminescence spectra of the samples were recorded as were the Raman scattering spectra. Sample *DJI22A* was then patterned using a bilayer of PMMA, 2.5% ELV on 2.5% BDH. The resist was then exposed using the e-beam writer with a nine step exposure test starting at 500 $\mu Ccm^{-3}$ and rising by a factor of 1.1 each time. The wires were reactive ion etched for 8 minutes in the sample using a 1:8 ratio of $CH_4$:$H_2$. A SEM micrograph of the 75 nm wide by 400 nm tall etched wires from the pattern exposed with 886 $\mu Ccm^{-3}$ is given in *Figure A8*. The photoluminescence and Raman spectra were then recorded from the wires to investigate any changes brought about by the etching, notably any confinement effects.

*Figure A8* SEM micrograph of wires etched in *DJI22A*.

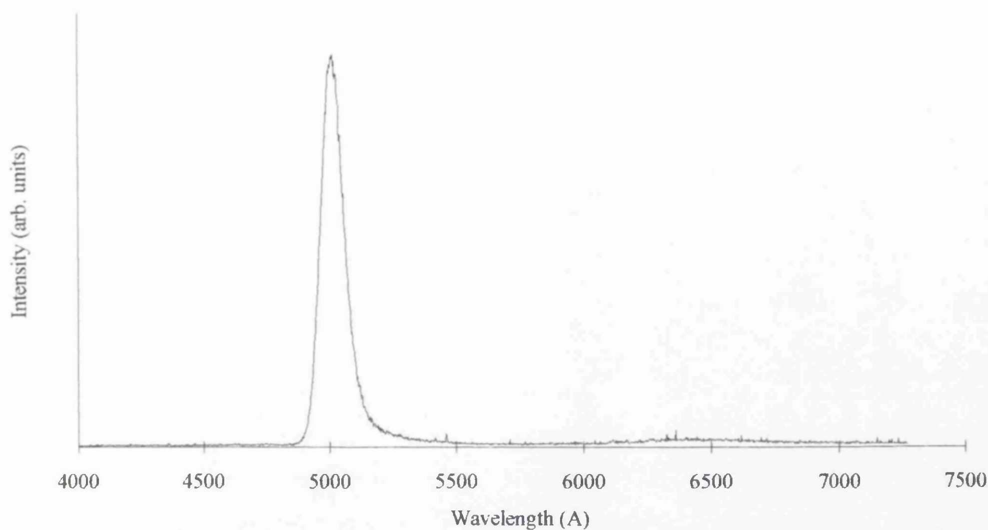


*Figure A9* Low temperature photoluminescence spectrum obtained from the unetched ZnSe/ZnCdSe superlattice sample, *DJI22A*. 5 K. 3638 Å excitation. 5 mW at cryostat. 2.5 Å resolution.

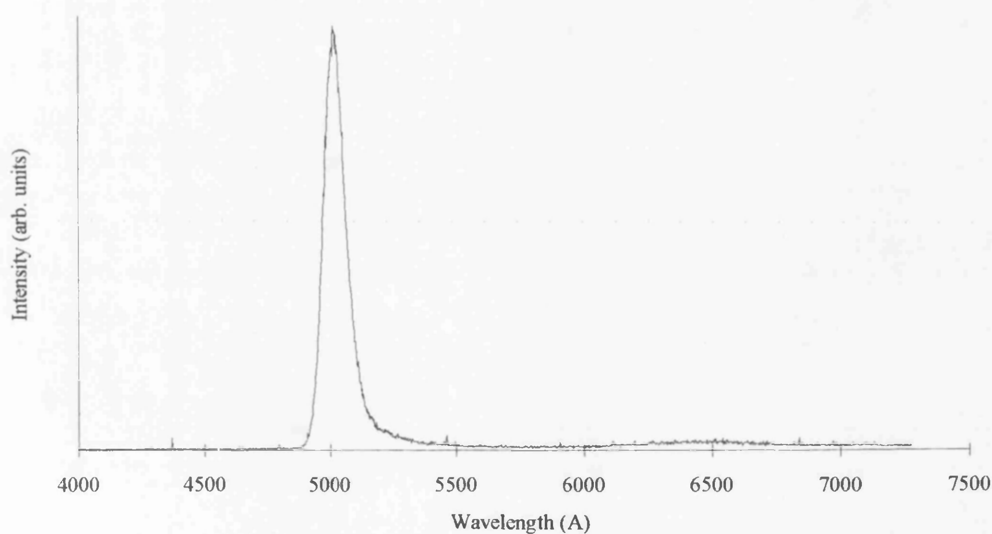


*Figure A10* Low temperature photoluminescence spectrum obtained from the wires etched in the ZnSe/ZnCdSe superlattice sample, *DJI22A*. 5 K. 3638 Å excitation. 5 mW at cryostat. 2.5 Å resolution.

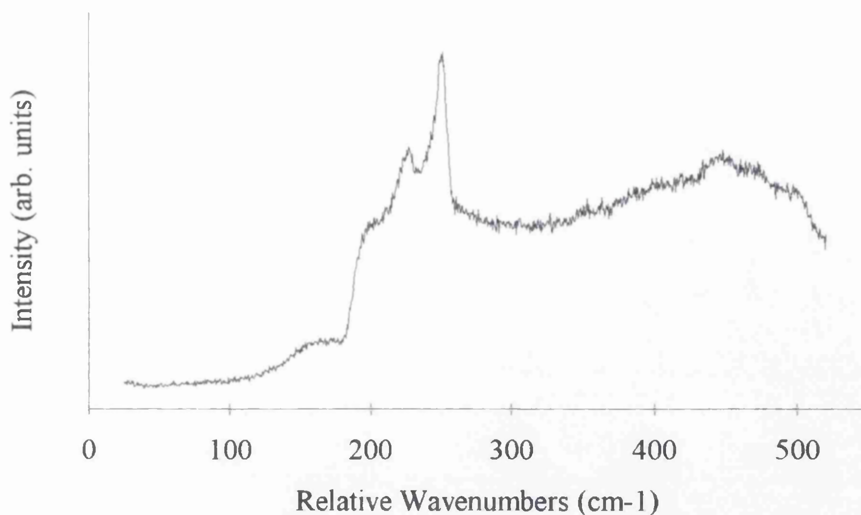


*Figure A11* Raman scattering spectrum obtained from the unetched ZnSe/ZnCdSe superlattice sample, *DJI22A*. 5 K. 4880 Å excitation. 10 mW at cryostat. 3 $cm^{-1}$ resolution.

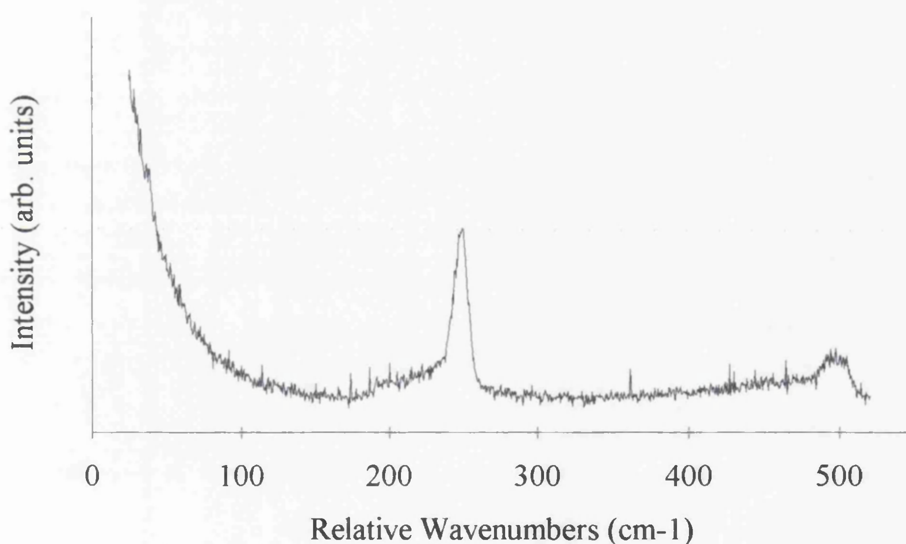


*Figure A12* Raman scattering spectrum obtained from the wires etched in the ZnSe/ZnCdSe superlattice sample, *DJI22A*. 5 K. 4880 Å excitation. 10 mW at cryostat. 3 $cm^{-1}$ resolution. Unpolarised.

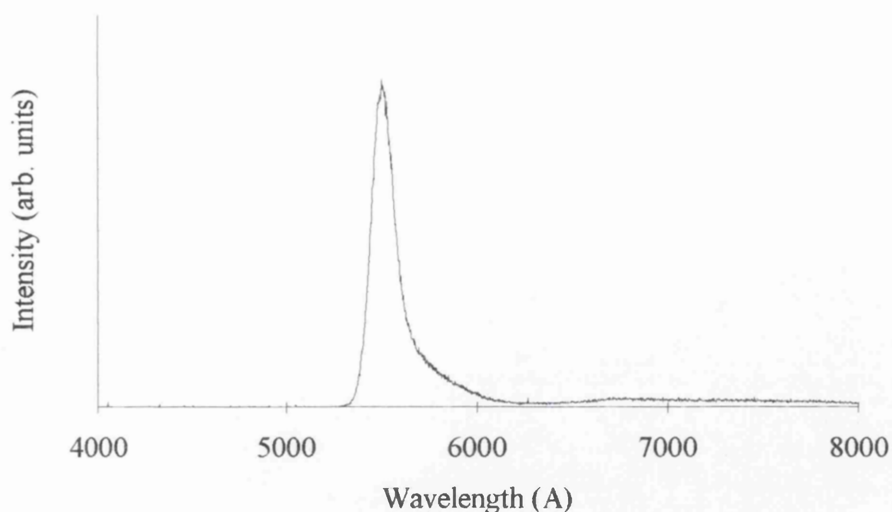


*Figure A13* Low temperature photoluminescence spectrum obtained from the unetched ZnSe/ZnCdSe superlattice sample, *DJI28A*. 5 K. 3638 Å excitation. 5 mW at cryostat. 2.5 Å resolution.

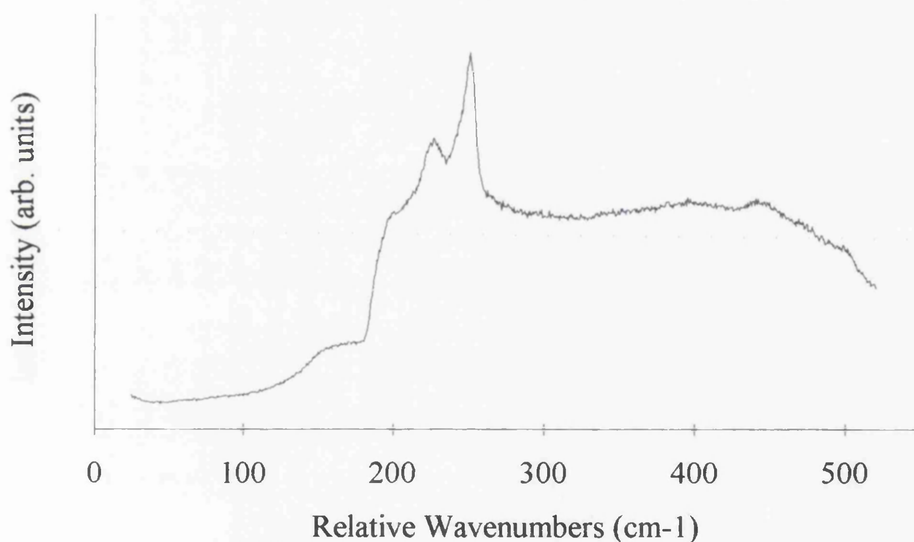


*Figure A14* Raman scattering spectrum obtained from the unetched ZnSe/ZnCdSe superlattice sample, *DJI28A*. 5 K. 4880 Å excitation. 10 mW at cryostat. 3 $cm^{-1}$ resolution. Unpolarised.

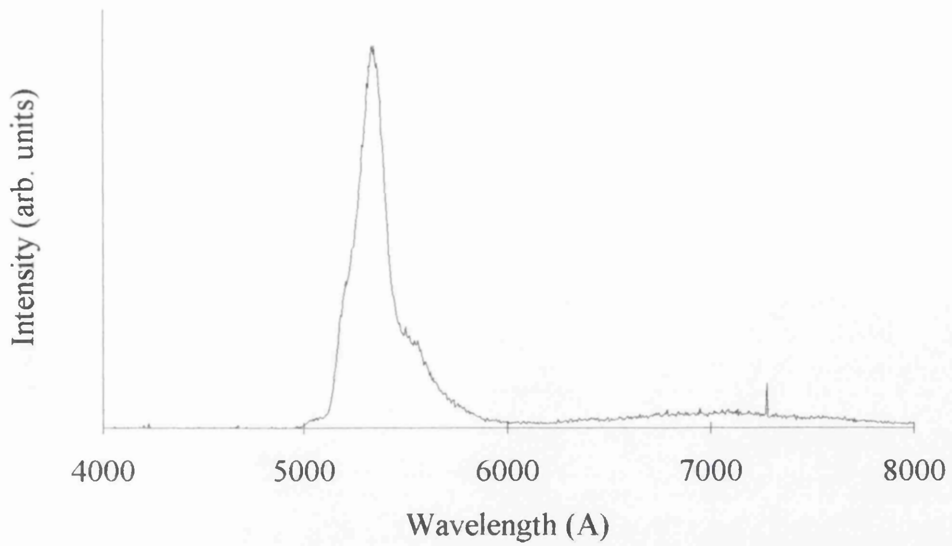


*Figure A15* Low temperature photoluminescence spectrum obtained from the unetched ZnSe/ZnCdSe superlattice sample, *DJI30A*. 5 K. 3638 Å excitation. 5 mW at cryostat. 2.5 Å resolution.

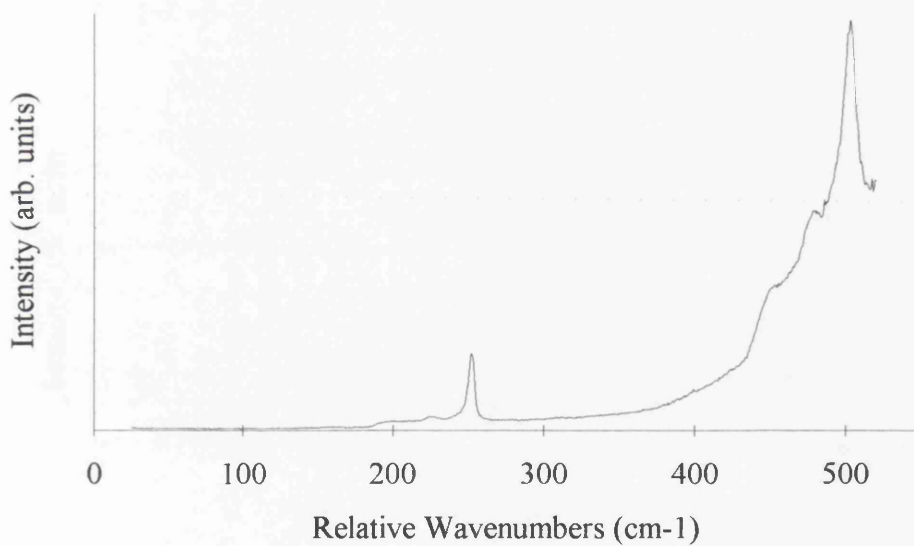


*Figure A16* Raman scattering spectrum obtained from the unetched ZnSe/ZnCdSe superlattice sample, *DJI30A*. 5 K. 4880 Å excitation. 10 mW at cryostat. 3 $cm^{-1}$ resolution. Unpolarised.

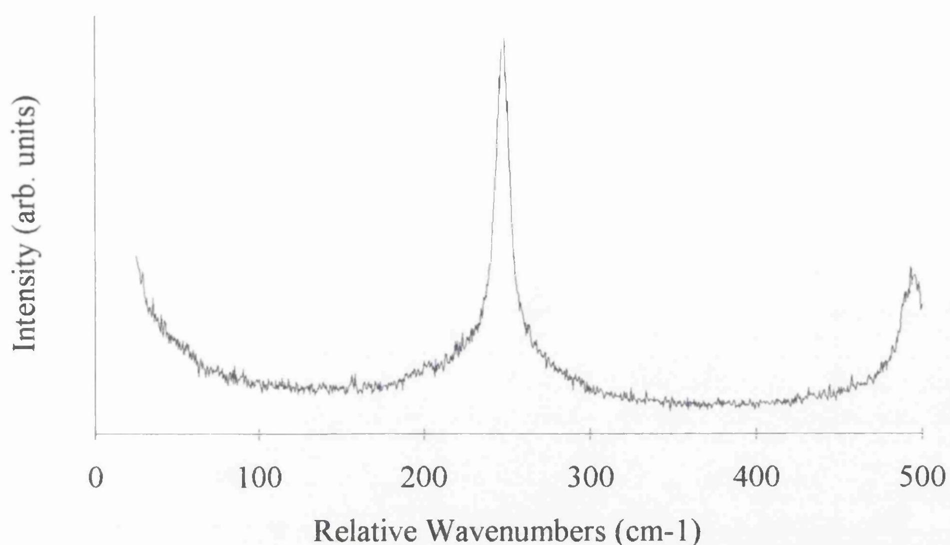


*Figure A17* Raman scattering spectrum obtained from the unetched ZnSe/ZnCdSe superlattice sample, *DJI30A*. Room temperature. 4880 Å excitation. 10 mW at sample. 3 $cm^{-1}$ resolution. Unpolarised.

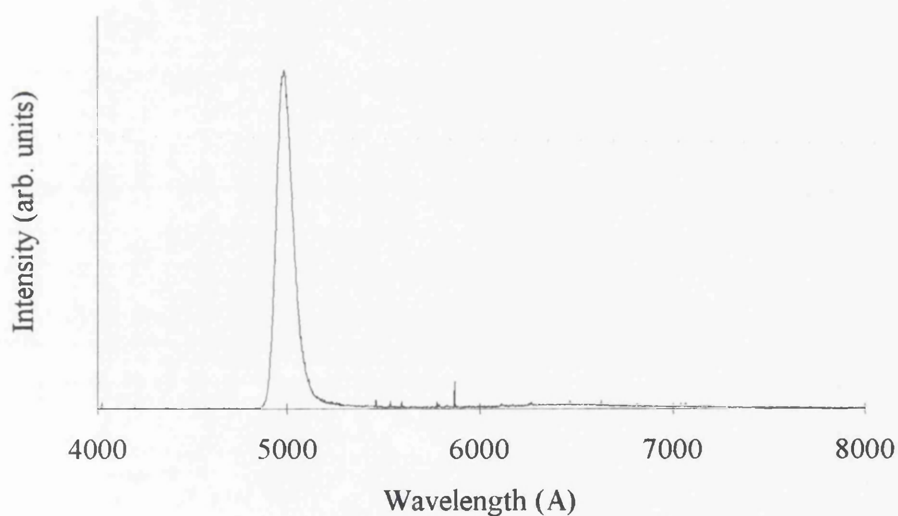


*Figure A18* Low temperature photoluminescence spectrum obtained from the unetched ZnSe/ZnCdSe superlattice sample, *DJI31A*. 5 K. 3638 Å excitation. 5 mW at cryostat. 2.5 Å resolution.

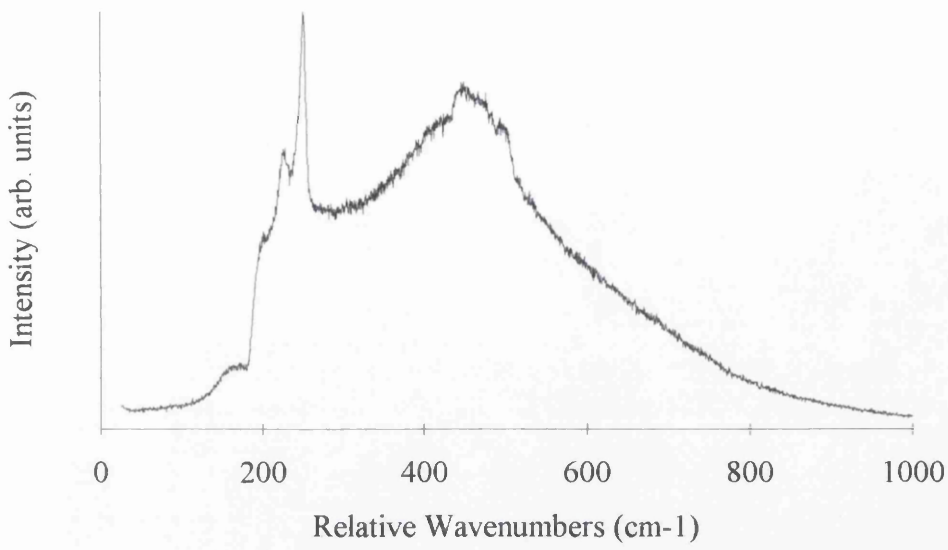


*Figure A19* Raman scattering spectrum obtained from the unetched ZnSe/ZnCdSe superlattice sample, *DJ131A*. 5 K. 4880 Å excitation. 10 mW at cryostat. 3 $cm^{-1}$ resolution. Unpolarised.

## References


1.1 "The Physics and Chemistry of II-VI Compounds"
Ed. Aven, M. and Prener, J.S.
North Holland, Amsterdam (1967).

1.2 "APA Optics Can Beat the Blues"
Electronics Weekly, May 25 (1994).

1.3 "IBM Goes Dotty for Compact Discs"
Electronics Weekly, May 25 (1994).

1.4 Sotomayor Torres, C.M., Smart, A.P., Watt, M., Foad, M.A., Tsutsui, K. and Wilkinson, C.D.W.
J. Electronic Materials **23** 289 (1994).

2.1 Gutowski, J., Presser, N. and Kudlek, G.
Phys. Stat. Sol. (a) **120** 11 (1990).

2.2 Hauksson, I.S., Simpson, J., Wang, S.Y., Prior, K.A. and Cavenett, B.C.
Appl. Phys. Lett. **61** 2208 (1992).

2.3 "Landolt-Börnstein Numerical Data and Functional Relationships in Science and Technology"
Volume **17**(b),
Ed. Madelung, O.,
Springer-Verlag, Berlin (1982).

2.4 Leiderer, H., Supritz, A., Silberbauer, M., Lidner, M., Kuhn, W., Wagner, H.P. and Gebhardt, W.
Semicond. Sci. Tech. **6** A101 (1991).

2.5 Leiderer, H., Jahn, G., Silbauer, M., Kuhn, W., Wagner, H.P., Limmer, W. and Gebhardt, W.
J. Appl. Phys. **70** 398 (1991).

2.6 Cheng, H, DePuydt, J.M., Potts, J.E. and Haase, M.A.
J. Crystal Growth **95** 512 (1989).

2.7 Yasuda, T., Mitsuishi, I. and Kukimoto, H.
Appl. Phys. Lett. **52** 57 (1988).

2.8 Cheng, H, DePuydt, J.M., Potts, J.E. and Smith, T.L.
Appl. Phys. Lett. **52** 147 (1988).

2.9 DePuydt, J.M., Haase, M.A., Cheng, H. and Potts, J.E.
Appl. Phys. Lett. **55** 1103 (1989).

2.10 Migita, M., Taike, A. and Yamamoto, H.
J. Appl. Phys. **68** 880 (1990).

2.11 Ohki, A., Shibata, N., Ando, K. and Katsui, A.
J. Crystal Growth **99** 413 (1990).

2.12 Mitsuhashi, H, Yahata, A, Uemoto, T., Kamata, A., Okajima, M., Hirahara, K. and Beppu, T.
J. Crystal Growth **101** 818 (1990).

2.13 Park, R.M., Troffer, M.B., Rouleau, C.M., DePuydt, J.M. and Haase, M.A.
Appl. Phys. Lett. **57** 2127 (1990).

2.14 Colak, S., Fitzpatrick, B.J. and Bhargava, R.N.
J. Crystal Growth **72** 504 (1985).

2.15 Ding, J., Jeon, H., Nurmikko, A.V., Luo, H., Samarth, N. and Furdyna, J.K.
Appl. Phys. Lett. **57** 2756 (1990).

2.16 Jeon, H., Ding, J., Nurmikko, A.V., Luo, H., Samarth, N., Furdyna, J.K., Bonner, W.A. and Nahory, R.E.
Appl. Phys. Lett. **57** 2413 (1990).

2.17 Guan, Y., Park, Y., Zory, P.S., Yoo, J. and Park, R.M.
"Evidence of Optical Gain at 475 nm (Blue) in ZnSe, Edge Light Emitting Diodes at Room Temperature"
IEEE/LEOS Annual Meeting, San Jose, CA. (1991).

2.18 Hovinen, M., Ding, J., Nurmikko, A.V., Grillo, D.C., Han, J., He, L. and Gunshor, R.L.
Appl. Phys. Lett. **63** 3128 (1993).

2.19 Haase, M.A., Qui, J., DePuydt, J.M. and Cheng, H.
Appl. Phys. Lett. **59** 1272 (1991).

2.20 "Gas Plasma Vapor Etching Process"
Irving, S.M., Lemons, K.E. and Bobos, G.E.
U.S. Patent 3 615 956 (1971).

2.21 "Trends in Plasma Sources: the Search Continues"
Ed. Singer, P.
Semiconductor International, July (1992).

2.22 Walecki, W., Patterson, W.R., Nurmikko, A.V., Luo, H., Samarth, N., Furdyna, J.K., Kobayashi, M., Durbin, S. and Gunshor, R.L.
Appl. Phys. Lett. **57** 2641 (1990).

2.23 Clausen Jr., E.M., Craighead, H.G., Tamargo, M.C., deMiguel, J.L. and Schiavone, L.M.
Appl. Phys. Lett. **53** 690 (1988).

2.24 Schäfer, P., Hoffmann, N., Parthier, L. and Jacobs, K.
J. Vac. Sci. Technol. A **11** 621 (1993).

2.25 Gant, H. and Mönch, W.
Surf. Sci. **105** 217 (1981).

2.26 Patterson, M.H. and Williams, R.H.
J. Phys. D: Appl. Phys. **11** L83 (1978).

2.27 "Handbook of X-Ray Photoelectron Spectroscopy"
Ed. Wagner, C.D., Riggs, W.M., Davies, L.E., Moulder, J.F. and Muilenberg, G.E.
Perkin-Elmer Corporation, New York, (1978).

2.28 "Si Processing for the VLSI Era"
Ed. Wolf, S.
University of California, Irvine, (1989).

2.29 "Microchip Fabrication: a Practical Guide to Semiconductor Processing"
2nd Edition
Ed. Van Zant, P.
McGraw-Hill, New York, (1990).

2.30 Eigler, D.M.
in: "Atomic and Nanometer-Scale Modification of Materials: Fundamentals and Applications"
Ed. Avouris, P.
NATO ASI Series E: Applied Sciences
Vol. **239**
Kluwer Academic Publishers, Dordrecht, (1993).

2.31 Sakaki, H.
Jpn. J. Appl. Phys. **19** L735 (1980).

2.32 Pelekanos, N.T., Ding, J., Nurmikko, A.V., Luo, H., Samarth, N. and Furdyna, J.K.
Phys. Rev. B **45** 6037 (1992).

2.33 Kawakami, Y., Hauksson, I., Stewart, H., Simpson, J., Galbraith, I., Prior, K.A. and Cavenett, B.C.
Phys. Rev. B **48** 11994 (1993).

2.34 Kawakami, Y., Wang, S.Y., Simpson, J., Hauksson, I., Adams, S.J.A., Stewart, H., Cavenett, B.C. and Prior, K.A.
Physica B **185** 496 (1993).

2.35 Miller, D.A.B., Chelma, D.S., Damen, T.C., Gossard, A.C., Wiegmann, W., Wood, T.H. and Burras, C.A.
Phys. Rev. B **32** 1043 (1985).

2.36 Wang, S.Y., Kawakami, Y., Simpson, J., Stewart, H., Prior, K.A. and Cavenett, B.C.
Appl. Phys. Lett. **62** 1715 (1993).

2.37 Wang, S.Y., Horsburgh, G., Thompson, P., Hauksson, I., Mullins, J.T., Prior, K.A. and Cavenett, B.C.
Appl. Phys. Lett. **63** 857 (1993).

3.1 Langen, B., Leiderer, H., Limmer, W., Gebhardt, W., Ruff, M. and Rössler, U.
J. Crystal Growth **101** 718 (1990).

3.2 Tokashiki, K., Sato, K., Aoto, N. and Ikawa, E.
J. Vac. Sci. Technol. B **11** 2284 (1993).

3.3 "Model 2040 and 2045 High Power Ion Laser Instruction Manual"
Spectra Physics Laser Products Division.

3.4 "Laserspec III Instruction Manual"
Spectrolab X-Ray Systems Electro-Optics.

3.5 "Laserspec III"
Technical Literature Spectrolab Electro-Optics.

3.6 "Optics Guide"
Volume 5,
Melles Griot (1990).

3.7 "Ramanor U1000 Monochromator Operating Instructions"
Jobin-Yvon Division d'Instruments S.A..

3.8 "Luminescence Spectroscopy"
Ed. Lumb, M.D.
Academic Press, London (1978).

3.9 "Accessories for Photomultiplier Tubes"
Hamamatsu Photonics K.K., Electron Tubes Division.

3.10 "Instructions Models 3457, 3461, 3462, 3470 Thermoelectric PMT Housings"
Pacific Instruments Inc..

3.11 "Model 33 Power Supply/Temperature Controller Operation and Maintenance Manual"
Pacific Instruments Inc..

3.12 "Photomultiplier Power Supply Type PM 28B and Type PM 28B/VP Operating Manual"
Thorn EMI Electron Tubes Ltd..

3.13 "Inelastic Light Scattering by Low Dimensional Structures"
Watt, M.
PhD Thesis, University of Glasgow (1989).

3.14 "Optical Properties of Novel GaAs-Based Semiconductors"
Ferguson, I.
PhD Thesis, University of St. Andrews (1989).

3.15 "Enhanced Prism Software Instruction Manual"
Version 1.2
Jobin-Yvon Division d'Instruments S.A..

3.16 "Spectralink Technical Manual"
Version 2.1
Jobin-Yvon Division d'Instruments S.A..

3.17 Holtz, M., Zallen, R., Brafman, O and Matteson, S.
Phys. Rev. B **37** 4609 (1988).

3.18 Foad, M.A., Watt, M., Smart, A.P., Sotomayor Torres, C.M., Wilkinson, C.D.W., Kuhn, W., Wagner, H.P., Leiderer, H., Bauer, S. and Gebhardt, W.
Semicond. Sci. Technol **6** A115 (1991).

3.19 "Physics of Semiconducting Devices"
2nd Edition
Sze, S.M.
John Wiley and Sons, New York, (1981).

3.20 "Optical Processes in Semiconductors"
Pankove, J.I.
Dover Publications Inc., New York, (1971).

3.21 Haynes, J.R.
Phys. Rev. Lett. **4** 361 (1960).

3.22 Raman, C.V.
Ind. J. Phys. **2** 387 (1928).

3.23 Smekal, A.
Naturwiss. **11** 873 (1923).

3.24 Loudon, R.
Advan. Phys. **13** 423 (1964).

3.25 Hopfield, J.J. and Thomas, D.G.
Phys. Rev. **132** 563 (1963).

3.26 "Light Scattering in Solids II"
Volume **50**, Topics in Applied Physics,
Ed. Cardona, M. and Güntherodt, G.
Springer, Berlin (1982).

3.27 Born, M. and Bradburn, M.
Proc. Roy. Soc. A **188** 161 (1947).

3.28 Smith, H.M.J.
Phil. Trans. A **241** 105 (1948).

3.29 Cantarero, A., Trallero-Giner, C. and Cardona, M.
Phys. Rev. B **39** 8388 (1989).

3.30 "Light Scattering in Solids I"
Volume **8**, Topics in Applied Physics, 2nd Edition,
Ed. Cardona, M.
Springer, Berlin (1983).

3.31 Ganguly, A.K. and Birman, J.L.
Phys. Rev. **162** 806 (1967).

3.32 Elliot, R.J.
Phys. Rev. **108** 1384 (1957).

3.33 Martin, R.M.
Phys. Rev. B **4** 3676 (1971).

3.34 Pikus, G.E. and Bir, G.L.
Sov. Phys.-Solid State **1** 136 (1959).

3.35 Fröhlich, H.
Adv. Phys. **3** 325 (1954).

3.36 Cantarero, A., Trallero-Giner, C. and Cardona, M.
Phys. Rev. B **40** 4030 (1989).

3.37 Kauschke, W. and Cardona, M.
Phys. Rev. B **33** 5473 (1986).

3.38 Brodsky, M.H., Gambino, R.J., Smith Jr., J.E. and Yacoby, Y.
Phys. Stat. Sol. (b) **52** 609 (1972).

3.39 Torrie, B.H.
Solid State Commun. **8** 1899 (1970).

3.40 Rama Rao, C.S. and Sundaram, S.
J. Appl. Phys. **54** 1808 (1983).

3.41 Wagner, J. and Hoffman, Ch.
Appl. Phys. Lett. **50** 682 (1987).

3.42 Trommer, R. and Cardona, M.
Phys. Rev. B **17** 1865 (1978).

3.43 Menéndez, J., Cardona, M. and Vodopyanov, L.K.
Phys. Rev. B **31** 3705 (1985).

3.44 Watt, M., Sotomayor Torres, C.M., Arnot, H.E.G. and Beaumont, S.P.
Semicond. Sci. Technol. **5** 285 (1990).

3.45 Stroscio, M.A.
in: "Phonons in Semiconductor Nanostructures"
Eds. Leburton, J.-P., Pascaul, J and Sotomayor Torres, C.M.
NATO ASI Series E: Applied Sciences
Vol. **236**
Kluwer Academic Publishers, Dordrecht, (1993).

3.46 Mori, N. and Ando, T.
Phys. Rev. B **40** 6175 (1989).

3.47 Bungaro, C., Lugli, P., Rossi, F., Rota, L. and Molinari, E.
"Phonons in Quantum Wires"
in "Ultrafast Laser Probe Phenomena in Semiconductors and Superconductors",
SPIE Proceedings,
Volume **1677** (1992).

3.48 Menéndez, J.
J. of Luminescence **44** 285 (1989).

3.49 "Introduction to Solid State Physics"
6th Edition
Kittel, C.
John Wiley and Sons, New York, (1986).

3.50 Huang, K. and Zhu, B.
Phys. Rev. B **38** 13377 (1988).

3.51 Rücker, H., Molinari, E. and Lugli, P.
Phys. Rev. B **44** 3463 (1991).

3.52 Sood, A.K., Menéndez, J., Cardona, M. and Ploog, K.
Phys. Rev. Lett. **54** 2111 (1985).

3.53 Ruppin, R. and Englman, R.
Rep. Prog. Phys. **33** 149 (1970).

4.1 Wagner, H.P., Kuhn, W. and Gebhardt, W.
J. Crystal Growth **101** 199 (1990).

4.2 Svob, L. and Marfaing, Y.
Solid State Commun. **58** 343 (1986).

4.3 Svob, L. and Marfaing, Y.
in: "Defects in Semiconductors"
Mater. Sci. Forum 10-12
Ed. von Bardeleben, H.J.
Trans Tech Publications, Switzerland (1986).

4.4 Singh, M. Weber, J. and Konuma, M.
in: "Hydrogen in Semiconductors"
Proc. 6th Trieste IUPAP-ICTP Semiconductor Symposium
Eds. Stutzmann, M. and Chevallier, J.
North-Holland, Amsterdam (1991).

4.5 Moisan, J.Y.
presented at: 2nd Meeting of French II-VI Semiconductor Researchers
Autrans
30 March - 1st April (1992).

4.6 Wilson, B.A., Bonner, C.E., Feldman, R.D., Austin, R.F., Kisker, D.W., Krajewski, J.J. and Bridenbaugh, P.M.
J. Appl. Phys. **64** 3210, (1988).

4.7 Meese, J.M. and Park, Y.S.
in: "Radiation Damage and Defects in Semiconductors"
Inst. Phys. Conf. Ser. 16
Ed. Baruch, P.
Institute of Physics, London (1973).

4.8 Halsall, M.P., Wolverson, D., Davies, J.J., Lunn, B. and Ashenford, D.E.
Appl. Phys. Lett. **60** 2129 (1992).

4.9 Hayashi, S., Sanda, H., Agata, M. and Yamamoto, K.
Phys. Rev. B **40** 5544 (1989).

5.1 Beaglehole, D.
IEEE Transactions on Electron Devices **ED-17** 3 (1970).

5.2 Dakss, M.L., Kuhn, L., Heidrich, P.F. and Scott, B.A.
App. Phys. Lett. **16** 523 (1970).

5.3 Streifer, W., Scifres, D.R. and Burnham, R.D.
IEEE J. Quant. Elect. **QE-12** 422 (1976).

5.4 Zettler, T., Peters, C., Kotthaus, J.P. and Ploog, K.
Phys. Rev. B **39** 3931 (1989).

UNIVERSITY